NASA-CR-194858

1151

REPORT TO THE

NATIONAL AERONAUTICS AND SPACE ADMINISTRATION

SEMIANNUAL STATUS REPORT #6

for

GRANT NAG 5-1490

INVESTIGATION OF PASSIVE ATMOSPHERIC SOUNDING USING MILLIMETER AND SUBMILLIMETER WAVELENGTH CHANNELS

A.J. Gasiewski (Principal Investigator)

D.B. Kunkee (Graduate Student)
D.M. Jackson (Graduate Student)

Covering the period from

July 1, 1993 to December 31, 1993

Submitted by:

Professor Albin J. Gasiewski
School of Electrical Engineering
Georgia Institute of Technology
Atlanta, Georgia, 30332-0250
(404) 894-2934

NASA Technical Officer:

Dr. Robert F. Adler
Laboratory for Atmospheres/Code 612
NASA Goddard Space Flight Center
Greenbelt, MD 20771
(301) 286-9086

TABLE OF CONTENTS

I. INTRODUCTION 1

II. DISCUSSION OF ACTIVITIES 3

III. SUMMARY AND PLANS FOR FUTURE WORK 10

IV. REFERENCES 14

V. TABLES AND FIGURES 16

VI. APPENDICES A-C 24

INTRODUCTION

Progress by the Georgia Institute of Technology's Laboratory for Radioscience and Remote Sensing in developing techniques for passive microwave retrieval of water vapor profiles and cloud and precipitation parameters using millimeter- and sub-millimeter wavelength channels is reviewed. Channels of particular interest are in the tropospheric transmission windows at 90, 166, 220, 340 and 410 GHz and centered around the water vapor lines at 183 and 325 GHz. Collectively, these channels have potential application in high-resolution mapping (e.g., from geosynchronous orbit), remote sensing of cloud and precipitation parameters, and improved retrieval of water vapor profiles.

During the period from July 1, 1993 through December 31, 1993, the first wideband millimeter-wave (MMW) and sub-millimeter wave (SMMW) atmospheric brightness imagery was obtained using the Millimeter Wave Imaging Radiometer (MIR). The data was recorded during flights of the MIR on the NASA ER-2 during CAMEX. A 325-GHz radiometer consisted of a submillimeter-wave DSB receiver with three IF channels at +/-1,3, and 8.5 GHz, and ~14 dB DSB noise figure was successfully integrated into the MIR for these experiments.

The submillimeter-wave imagery unambiguously reveals the presence of the 325 GHz absorption line as manifested by the spectral signatures obtained over clouds and convective precipitation cells, and demonstrates the potential for mapping such features using SMMW channels. Analysis of the MIR SMMW data along with MIR airborne data from cases during TOGA/COARE is in progress, with the primary effort directed toward verifying both clear and cloudy radiative transfer models at MMW and SMMW frequencies. The analyses use coincident data from several ground-based, airborne, and satellite sensors, including the NASA/MSFC AMPR, the MIT MIS, the DMSP SSM/T-2 satellite, collocated radiosondes, ground- and aircraft-based radiometers and cloud lidars, airborne infrared imagers, solar flux probes and airborne cloud particle sampling probes.

A summary of comparisons between computed and measured clear-air brightness temperatures at the millimeter wave channels 89, 150, 183+/-

1,3,7, and 220 GHz has been submitted for publication. The clear-air data show good general agreement between measured brightness temperatures and computed brightness temperatures based on coincident radiosondes, although the discrepancies between these brightness temperatures show that the humidity probes on AIR and VIZ type radiosondes provide readings that are too moist in dry regions of the atmosphere. A study using clear-air 325-GHz airborne data from CAMEX and ground-based data observed at Georgia Tech is underway.

In order to resolve questions concerning the absolute calibration of both the MIR and similar microwave sounders, our study of the scattering and emission from microwave blackbody calibration loads has continued. An extension of the coupled wave method to two-dimensional periodic structures is being developed, and a steady state temperature field solution for the wedge-type structure has been developed. The goals of these numerical studies are to be able to predict the emitted brightness of such loads when used as wideband calibration targets.

The ability to remotely sense oceanic wind direction using passive polarimetric observations is also being studied. A millimeter-wave geometrical optics (GO) model for small-amplitude (1-cm peak-to-peak) water waves has been successfully corroborated by 92-GHz laboratory measurements of polarimetric emission from a wave tank. A discussion of the GO model and the utility of the third Stokes parameter $T_U=Re\langle E_v E_h^* \rangle$ for passive remote sensing of water wave direction along with a summary of the lab measurements has been submitted for publication. Constant bank-angle scans of the ocean using a side-looking 92-GHz radiometer on the NASA DC-8 during TOGA/COARE show wind-related anisotropies in the upwelling brightness that also appear to be of geometrical optics nature in origin. Reduction and archival of the 92-GHHz TOGA/COARE data is nearly complete.

DISCUSSION OF ACTIVITIES

Activities within the period from July 1, 1993 through December 31, 1993 under NASA grant NAG 5-1490 have focused on the integration of the three-channel 325-GHz receiver on the MIR, operation of the MIR aboard the NASA ER-2 during CAMEX (September, 1993), and calibration of the MIR using an optimal nonlinear filtering technique. In addition, MIR data analyses have continued or commenced, including: (1) several TOGA/COARE meteorological cases, (2) a preliminary analysis of the 325-GHz data, and (3) final analysis of clear-air MMW brightness data that were measured prior to TOGA/COARE [Jackson and Gasiewski, 1993, Appendix A].

The MIR is a joint project between the NASA Goddard Space Flight Center and the Laboratory for Radioscience and Remote Sensing at Georgia Tech. Past Georgia Tech contributions to the MIR and its related scientific uses have included basic system design studies, performance analyses, circuit and radiometric load design, in-flight software, operation of the MIR during field deployments, development of post-flight data display and calibration software, and radiative transfer studies of the effects of clouds, water vapor, and precipitation on MIR brightness temperatures. During December 1993, the MIR was transported to Georgia Tech for characterization and ground-based experiments involving the 325-GHz radiometer.

In addition to the MIR-related activities, data from a 92-GHz polarimetric radiometer that was deployed on the NASA DC-8 during TOGA/COARE has been calibrated and analyzed. The polarimetric capabilities of the 92-GHz radiometer were added by Georgia Tech to investigate the relationship between polarized microwave brightness temperatures and both oriented atmospheric ice cloud particles and anisotropic ocean surface features. To improve the accuracy of fully polarimetric radiometers, we have designed and begun to construct a prototype digital correlator with up to 1-GHz bandwidth. The correlator will have direct applications in airborne polarimetric radiometers such as the NASA/MSFC Advanced Microwave Precipitation Radiometer (AMPR).

1. MIR 325-GHz Imagery

In August 1993 a 325-GHz three-channel DSB radiometer was integrated into the MIR. The 325-GHz receiver was built by the ZAX Millimeter Wave Corporation according to radiometric specifications defined by Georgia Tech. The receiver uses a fundamental-mode mixer with DC bias and a frequency-tripled 108-GHz Gunn oscillator. Three IF channels, one each from 500-1500, 2000-4000, and 7000-10000 MHz provide spectral sampling similar to that of the 183-GHz MIR receiver. All channels are of the total power type. With the inclusion of this radiometer the MIR now has nine channels at 89, 150, 183+/-1,3,7, 220, and 325+/-1,3,8.5 GHz.

The measured noise figure of the 325-GHz receiver is ~14 dB. Although this is relatively high compared to the other four MIR receivers, it yields integration noise levels of ~2-3 K for a 6-msec pixel; these have been shown to be acceptable for initial scientific evaluation of the 325.153 GHz water vapor absorption line.

MIR data is being analyzed from several flights during four ER-2 field deployments, summarized in Table 1. In addition to the case studies outlined previously[1], the following new case studies involving the 325-GHz channels have been identified and are being analyzed:

(1) Clear-air imagery observed during CAMEX (Figures 1 and 2, non-cloudy regions) show brightness temperatures that are, on average, approximately the same over all three 325-GHz channels. This is in contrast to radiative transfer predictions based on the Liebe water vapor absorption model. Under the Liebe model [Gasiewski, 1992], the computed brightness temperatures for the three 325-GHz channels are nearly identical to those of the analogous three 183-GHz channels, and span a range of ~25 K. This discrepancy has not yet been explained, but is of critical importance in assessing the potential for water vapor sounding at 325 GHz.

(2) During several CAMEX flights the MIR observed strong convection over both ocean and land. Strip map images of brightness temperature during the flight lines in Figures 1 and 2 show several interesting features of the 325 GHz imagery. First, virtually all of the convection that was

---

[1] Semiannual Status Report #5 for NASA grant NAG 5-1490, June 30, 1993.

detected in the channels at 220 GHz and lower in frequency was detected with comparable brightness variations at 325 GHz. Thus, water vapor screening of convective cell tops does not seem to be significant. This observation contrasts with some previous hypotheses which suggested that water vapor opacity would preclude detection of cells at 325 GHz.

Second, the 325-GHz channels respond to clouds and precipitation in a monotonic fashion. This response is a result of the radiometrically warm background caused by the opaque lower atmosphere. In contrast, the 89 and 150 GHz channels exhibit small increases in brightness in response to thin clouds; the brightness then decreases as cloud opacity and scattering increase. In addition, the scattering and absorption at 325 GHz are larger than at 89 or 150 GHz. For these two reasons the 325 GHz channels are significantly more sensitive to thin clouds and weak precipitation, as can be seen by comparing the apparent edges of rain cells in the 325 and 89/150 GHz channels.

Third, the 325-GHz channels unambiguously show the presence of the 325.153 GHz water vapor absorption line. This is evidenced by the increased cloud sensitivity seen in the 325 +/-8.5 GHz channel relative to the 325+/-1 GHz channel. Increased absorption by water near the line center reduces the reflectivity of the cell top, thereby raising the brightness temperature. The same phenomena is seen in the 183+/-1,3, and 7 GHz channels.

Applicable supporting data from other instruments is being compiled for both the above CAMEX 325-GHz analyses and ongoing TOGA/COARE analyses. These data are from the Massachusetts Institute of Technology's Millimeter-wave Temperature Sounder (MTS), the NASA/MSFC Advanced Microwave Precipitation Radiometer (AMPR), the NASA Airborne Ocean Color Imager (AOCI), the DMSP SSM/T-2 radiometric sounder, the NASA/GSFC Raman water vapor lidar, and collocated radiosondes.

2. MIR Calibration

In order to accommodate the relatively large noise levels of the 325-GHz channels, as well as to improve the calibration of all the other channels, a nonlinear calibration filter was developed. The filter is based on: (1) identification and removal of non-stationary features in the single-scan gain and offset data, (2) subsequent optimal time-invariant

filtering of the residual gain and offset signals, and (3) reconstruction of the overall gain and offset waveforms. The non-stationary features include jumps and spurious noise. An iterative technique based on the CLEAN algorithm is used for their detection. Upon their removal, an optimal time-invariant linear filter (the Wiener filter) is constructed for each radiometric channel. The filters are based on the estimated noise levels and autocorrelation time constants for the particular channel. In this manner, the unique statistical characteristics of each channel are accommodated.

The nonlinear calibration procedure has been shown to decrease the contribution of calibration noise in the brightness temperature imagery, particularly for the 325-GHz channels.[2] The implementation of the optimal calibration algorithm, accommodation of the new 325-GHz channels, and the provision of several new data editing features required major modifications to the post-flight data analysis software. Most of these have now been completed.

3. Calibration Load Analysis

The emission temperature of a calibration target must be known to better than ~0.5 K to be useful in calibrating radiometers. To precisely predict the emission, it is necessary to determine both the physical temperature and electromagnetic field distribution within the target, which is typically an array of absorbing wedges or pyramids. The emission temperature is the overlap integral of the thermal temperature and a normalized function that is proportional to the electromagnetic power loss density. This analysis is particularly important for targets used in airborne radiometers since these targets are subject to large thermal gradients caused by advective cooling. Precise knowledge of the electromagnetic distribution in wedge and pyramid arrays is also important in the design of microwave absorbers for a variety of purposes, for example, anechoic chambers.

To this end, a steady state numerical solution to the heat equation for a wedge-type structure has been developed using a coupled harmonic method.

---

[2] The basic technique is described by Adelberg and Gasiewski [1993, Appendix B].

The preliminary results of the thermal model suggest that temperature gradients near the absorbing (and, hence, emitting) tips of the wedges are significant enough to warrant consideration in calibration load analysis [Gasiewski and Jackson, 1993].

4. Polarimetric Microwave Radiometry

Polarimetric microwave radiometry has been shown to have potential in spaceborne remote sensing of ocean wave direction [Wentz, 1992; Dzura 1992] and, possibly, in detection of oriented thunderstorm anvil ice [Evans and Vivekanandan, 1990]. We have investigated this both experimentally and theoretically using fully polarimetric laboratory measurements at 92 GHz of upwelling emission from a fresh-water wave tank [Gasiewski and Kunkee, 1993b, see Appendix C; Kunkee and Gasiewski, 1993]. The measurements, which were made using the NASA/GSFC 92-GHz polarimetric radiometer,[3] are well corroborated by a geometrical optics model for anisotropic surface emission. Both model and measurements show that significant brightness variations in the first three Stokes parameters can be produced by only moderately striated dielectric surfaces.

Specifically, the laboratory measurements show a predictable dependence of $T_U=\mathrm{Re}\langle E_v E_h^* \rangle$ on the direction of the water wave, with peak-to-peak amplitudes of up to 20 K at steep observation angles. Moreover, the T_U angular variations are in phase quadrature with similarly strong variations exhibited by T_v and T_h, suggesting that passive remote sensing of surface wave direction can be facilitated by polarimetric microwave radiometry. Both the measurements and model calculations consider all four Stokes' parameters, although the last of these ($T_V=\mathrm{Im}\langle E_v E_h^* \rangle$) is very small and not expected to be useful for geophysical remote sensing of the troposphere or surface.

The encouraging results of the wave tank experiment prompted an airborne field experiment during TOGA/COARE to investigate passive polarimetric measurement of ocean wave direction. Indirectly, one can be expected to infer atmospheric wind direction from such measurements. Electronic and hardware modifications necessary to operate the polarimetric

---

[3] The polarimetric capability was added by Georgia Tech under a previous NASA grant (NAG 8-829) [see Gasiewski and Kunkee, 1993a].

radiometer on the NASA DC-8 aircraft were performed. A total of twenty DC-8 flights occurred during TOGA/COARE, including seven low-altitude (1.5-4 km) constant bank-angle maneuvers designed to provide views of the ocean surface at a constant observation angle and over a range of azimuthal angles [Kunkee and Gasiewski, 1994].

Post-mission calibration of nearly all of the 92-GHz polarimetric data has been completed. A plot of the constant bank-angle data for an incidence angle of 65° (Figure 3) shows residual peak-to-peak brightness variations over azimuthal angle of amplitude ~3 K for T_v and T_h. The shape and amplitude of the variations are closely related to those found by Wentz [1992]. Even for observation at nadir (Figure 4), sinusoidal brightness variations of amplitude ~1 K (complementary in T_v and T_h) can be seen. Although the nadir variations are not large enough for retrieval purposes, they are large enough to adversely impact brightness measurements for some atmospheric sounding purposes, for example, wet path delay measurements or water vapor sounding. The TOGA/COARE data, along with the laboratory wave tank measurements corroborate the hypothesis that anisotropic ocean surface signatures can be observed using microwave radiometers.

In addition to striated water surfaces, it has been hypothesized that polarimetric microwave signatures in T_v, T_h, and T_U will be produced by oriented ice particles, for example, in electrified cirrus anvils. Indeed, microwave depolarization signatures in space-to-ground communications links have been associated with lightning discharges [Cox and Arnold, 1979]. Although polarized microwave signatures from hydrometeors have not yet been definitively observed in the TOGA/COARE data, we are analyzing the origin of apparent T_v-T_h differences of up to +/-10 K observed at 92 GHz over oceanic convection. Supporting data from the other side-looking radiometric instruments that flew on the DC-8 is being sought to verify whether or not these differences are instrumental.

5. Digital Correlator for Polarimetric Radiometry

In anticipation of the need for precision airborne and spaceborne polarimetric radiometry, a high-speed digital correlator for proposed use in the NASA/MSFC Advanced Microwave Precipitation Radiometer (AMPR) is

being developed [Gasiewski and Kunkee, 1992].[4] A prototype A/D converter operating at 800 Ms/sec and using standard emitter-coupled logic (ECL) has been demonstrated (Figure 5). Two such A/D converters along with three high speed digital counters are the essential components of the correlator. The reason for using digital correlation is that calibration of the cross-correlation channel can be accurately performed using only the standard hot and cold calibration targets found in convectional radiometers. The performance of our prototype converter suggests that the necessarily wide IF bandwidths required for Earth remote sensing (in this case, up to 400 MHz) can be obtained using the digital technique. Measurements of converter hysteresis and development of the ECL counters (to be used in conjunction with the A/D converters to form the complete correlator) are in progress.

---

[4] A proposal for much more extensive development of digital correlation polarimetry and its evaluation on the NASA/MSFC AMPR has been submitted by this PI to NASA Headquarters under the title "Passive Measurement and Interpretation of Polarized Microwave Brightness Temperatures," September 1992, NASA control # 2916-RD-074.

SUMMARY AND PLANS FOR FUTURE WORK

The investigations conducted over the past six months have served purposes, including: (1) the first demonstration of radiometric imaging for meteorological purposes at 325 GHz, (2) the development and implementation of optimal nonlinear filters for radiometer calibration, (3) identification of several case studies for radiative transfer modelling at both millimeter- and submillimeter frequencies, and in both clear and cloudy atmospheres, and (4) demonstration of brightness temperature anisotropies caused by ocean waves at 92 GHz. Future plans which build on the findings of these investigations are outlined below.

1. MIR Observations and Data Analysis

An ensemble of clear-air 325-GHz observations for the purpose of radiative transfer model validation will be compiled from the CAMEX data. Ground based data measured with the MIR at Georgia Tech will be used to supplement this. These data will be compared with computed brightness temperatures based on collocated radiosondes and the Liebe water vapor absorption model [Liebe, 1985]. Steps to improve the absolute calibration of the MIR (see Section 2 below) will be necessary in these comparisons.

Several convective case studies from CAMEX are also being compiled for statistical analysis. During the convective overflight on October 5, 1993, the ER-2 Doppler radar (EDOP) obtained coincident nadir reflectivity profiles. This is the first joint EDOP and MIR data set. Because of the coincident EDOP radar truth, analysis of the MIR data from this flight is of great interest.

Two of the MIR case studies identified during TOGA/COARE are particularly interesting for radiative transfer experiments, namely, the overflights of cyclone Oliver and the Kavieng ground observation site. To this end, we plan to simulate ocean surface and atmospheric conditions within the eye of cyclone Oliver to determine the consistency of wideband radiative transfer models using the observed brightness data. The radiative transfer model will consider the effects of increasing humidity, precipitation, and ocean roughness near the eyewall to determine the relative contributions of these components to the warm ring. This

experiment will require some data from the NASA/MSFC AMPR and JPL ARMAR, both of which are available and are being requested.[5]

The Kavieng overflights will be used to provide data for simulating the effects of clouds on upwelling MMW brightness temperatures. Ground-based radiometer data will be used to determine total water vapor and cloud content, while ground-based lidar will be used to determine cloud bottom altitudes. Radiosondes will be further used to constrain the vertical distribution of water vapor. Of interest is a comparison of computed and observed upwelling brightness temperature, and in particular, the impact that clouds have on these temperatures.

MIR data is currently stored in raw format on high-density 8-mm tapes. To facilitate meteorological data analysis and to provide a practical means of disseminating MIR data to collaborating investigators, the display software is being modified for disk-based storage. This software, which will be available for use on PC's, will also incorporate a variety of simple interactive features for MIR data analysis. The MIR data is also being archived on 35-mm slides for graphical storage and dissemination.

2. Radiometer Calibration

In order to better characterize the RF response and absolute accuracy of the MIR, we plan to conduct several tests, including: (1) RF passband response measurements using a plasma discharge noise source and IF spectrum analyzer, (2) local oscillator interference and reflection measurements using a stepped reflecting plate, and (3) calibration-load foam reflection and transmission measurements. These simple measurements will provide answers to questions concerning the calibration of the MIR and the use of the 183 and 325-GHz data in radiative transfer intercomparisons. Particular attention is being paid to the 150 GHz channel, which consistently returns brightness temperatures that are 5-10 K colder than expected from an absorber immersed in liquid nitrogen.

We are now beginning to use the nonlinear calibration technique for operational calibration of all MIR data, including flights during CAMEX and TOGA/COARE. We plan to archive the calibrated data so that it will be

---

[5] Collaborating on the TOGA/COARE data analysis is Dr. J. Vivekanandan of the University of Colorado.

available to investigators collaborating on TOGA/COARE studies. A 1-GB hard disk drive has been obtained under this grant to support the calibration and archival effort. Further improvement in the nonlinear calibration algorithm is expected to be found by using a multidimensional Wiener filter. This will be tested, and if successful, will be implemented prior to archival.

Accurate absolute calibration of the MIR (and similar radiometers) requires that the total reflectivity of the hot and cold loads be less than -1%, and known to better than 0.1%. Manufacturer's specifications typically provide only the specular component of the reflectivity, which is thought to be substantially less than the total reflectivity. In order to refine the MIR calibration, we plan to extend the study of the electromagnetic characteristics of wedge-type blackbody loads to the more desirable pyramidal loads.

Our approach is to develop numerical models for one- and two-dimensionally periodic lossy gratings using the coupled wave method. We currently have software based on the coupled wave method to predict the reflectivity of one-dimensionally periodic loads of arbitrary dielectric profile. Extension of the coupled wave model to two-dimensionally periodic surfaces appears feasible, and will be continued. In addition to the electromagnetic analysis, work on the steady state thermal analysis for two-dimensionally periodic calibration loads will be continued. Although, the radiometric calibration load reflectivity analysis is of importance in understanding precision radiometer calibration, it is of secondary importance relative to the MMW and SMMW data analysis.

3. Polarimetric Radiometry

Further investigations of polarimetric radiometry will consist of follow-up analyses of 92-GHz polarimetric data observed during TOGA/COARE, and the development of a statistical ocean surface emission model using geometrical optics theory for corroboration of the measured TOGA/COARE data. The model will include the effects of ocean surface foam. The limitations of the geometrical optics model in explaining the wave tank and ocean surface data will be of interest; the validity of this model at 92-GHz will provide insight into the applicability of geometrical optics-based models for higher microwave frequencies. Information on the polarizing

properties of surfaces will be useful in remote sensing of ocean surface characteristics and in understanding the impact of ocean surface emission on passive atmospheric sounding.

To reduce the complexity of calibrating a polarimetric radiometer, the development of a working digital cross-correlator will be continued. The cross correlator will be a prototype for the one proposed to be used on the NASA/MSFC AMPR. The bandwidth of the cross-correlator will be approximately 500 MHz, making the device useful for wideband radiometric channel studies.

REFERENCES

Adelberg, L.K., A.J. Gasiewski and D.M. Jackson, "Optimal Calibration of Radiometers using Discrete Wiener Filters", presented at the 1993 International Geoscience and Remote Sensing Symposium, Tokyo, Japan, August 18-23, 1993.

Cox, D.C., and H.W. Arnold, "Observations of Rapid Changes in the Orientation and Degree of Alignment of Ice Particles Along an Earth-Space Radio Propagation Path", J. Geophys. Res., vol. 84, pp. 5003-5010, 1979.

Dzura, M.S., V.S. Etkin, A.S. Khrupin, M.N. Pospelov, M.D. Raev, "Radiometers-Polarimeters: Principles of Design and Applications for Sea Surface Microwave Emission Polarimetry", Proceedings of the 1992 IEEE International Geoscience and Remote Sensing Symposium (IGARSS), pp. 1432-1434, June, 1992.

Evans, K.F., and J. Vivekanandan, "Multiparameter Radar and Microwave Radiative Transfer Modeling of Nonspherical Atmospheric Ice Particles", IEEE Trans. Geosci. Remote Sensing, Vol. 28, No. 4, pp. 423-427, July, 1990.

Gasiewski, A.J., "Numerical Sensitivity Analysis of Passive EHF and SMMW Channels to Tropospheric Water Vapor, Clouds, and Precipitation", IEEE Trans. Geosci. Remote Sensing, Vol. 30, No. 5, pp. 859-870, September, 1992.

Gasiewski, A.J., and D.M. Jackson, "Electromagnetic Scattering from Lossy Periodic Surfaces: Application to Microwave Absorbers", submitted for publication in IEEE Transactions on Antennas and Propagation, March, 1993.

Gasiewski, A.J., and D.B. Kunkee, "Airborne Full Polarization Radiometry Using the MSFC Advanced Microwave Precipitation Radiometer (AMPR)", NASA Marshall Space Flight Center Earth Science and Applications Programs 1992 Research Review, Huntsville, AL, July 7-9, 1992.

Gasiewski, A.J., and D.B. Kunkee, "Calibration and Applications of Polarization Correlation Radiometers", IEEE Trans. Microwave Theory Tech., Vol. 41, No. 5, pp. 767-773, May, 1993a.

Gasiewski, A.J., and D.B. Kunkee, "Polarized Thermal Emission from Water Waves", submitted to Radio Science, November, 1993b.

Jackson, D.M., and Gasiewski, A.J., "Millimeter-Wave Radiometric Observations of the Troposphere: A Comparison of Measurements and Calculations Based on Radiosonde and Raman Lidar," submitted to

IEEE Transactions on Geoscience and Remote Sensing, December, 1993.

Kunkee, D.B., and A.J. Gasiewski, "Laboratory Measurements of Water Gravity Wave Characteristics using Full Polarization Microwave Radiometry", Proceedings of the 1993 URSI National Radio Science Meeting, p. 155, presented at the University of Colorado, Boulder, CO, Jan 5-8, 1993.

Kunkee, D.B., and A.J. Gasiewski, "Airborne Passive Polarimetric Observations of Ocean Wave Anisotropy at 92 GHz During TOGA/COARE", Proceedings of the 1994 URSI National Radio Science Meeting, p. 155, presented at the University of Colorado, Boulder, CO, Jan 5-8, 1994.

Kuo, C.C., "Statistical Iterative Scheme for Estimating Relative Humidity Profiles from Microwave Radiometric Measurements", S.M. Thesis, Massachusetts Institute of Technology, Cambridge, MA, 1988.

Liebe, H.J., "An Updated Model for Millimeter-Wave Propagation in Moist Air", Radio Sci., Vol. 20, No. 5, pp. 1069-1089, 1985.

Wentz, F.J., "Measurement of Oceanic Wind Vector Using Satellite Microwave Radiometers", IEEE Trans. Geosci. Remote Sensing, vol. 30, no. 5, pp. 960-972, September 1992.

Table 1.

MIR integration and data flights: 1992-93.

Sortie #	Date	Time (UTC)	Instruments & Remarks
Moffett Field, CA:			
92-087	5/11/92	1900-2200	MIR,MIS(u),AOCI
92-089	5/14/92	2315-0515	MIR,MIS(d),AOCI *
92-090	5/15/92	2320-0500	MIR,MIS(u),AOCI *
Wallops Island, VA:			
92-130	7/23/92	2100-2315	MIS(d)
92-131	7/29/92	0700-1330	MIS(d) +*
92-132	7/30/92	0700-1330	MIS(d) +*
92-134	8/2/92	0700-1030	MIS(d) +
92-135	8/3/92	0700-0615	MIS(u) +
92-140	8/6/92	0700-1330	MIS(u) +*
TOGA/COARE (Townsville, AUS)			
93-053	1/12/93	2130-0430	Radiation (93-01-06)
93-054	1/17/93	2300-0710	Convection (93-01-07)
93-055	1/19/93	0130-0922	Convection (93-01-08)
93-056	1/25/93	2315-0700	Radiation/Kavieng (93-01-09)
93-057	1/30/93		Pilot proficiency
93-058	1/31/93	2200-0600	Radiation (93-01-10)
93-060	2/5/93	1430-2050	Convection, Oliver overflight (93-01-11) *
93-061	2/7/93	1555-2115	Cyclone Oliver, MIS(d)
93-062	2/9/93	1815-0025	Oliver overflight (93-01-13)
93-063	2/10/93	1430-2225	Kavieng, MIS(d) (93-01-14) *
93-064	2/19/93		Pilot proficiency, MIS(u)
93-065	2/20/93	1900-0335	Convection (93-01-16)
93-066	2/22/93	1900-0205	Convection (93-01-17)
93-067	2/24/93	2000-0315	Radiation (93-01-08)
CAMEX (Wallops Island, VA):			
93-164	9/12/93		Convection, Transit Flight
93-165	9/15/93		Flight #1 Eng. Test (aborted)
93-166	9/19/93		Flight #2 Eng. Test
93-167	9/25/93	1751-2002	Eng. Test Flight (times unsync'd)
93-168	9/26/93	1908-2341	Flight #3
93-169	9/29/93	0106-0458	Flight #4 (AIRS)
93-178	9/30/93	2012-0213	FLight #5 (SSM/T-2)
94-001	10/3/93		Flight #6 (convection)
94-00x	10/5/93		Flight #7 (convection,EDOP)

Notes for Table 1

* SSM/T-2 satellite underpass.
+ Ground-based Raman H_2O_v lidar overflight.
(xx-xx-xx) indicate coincident DC-8 flights.

Note: "u" or "d" indicate up-looking or down-looking, respectively.

All CAMEX flights include the 325-GHz channels.

Figure 1 (p. 19): Strip map images of oceanic convection observed by the MIR on the ER-2 at 20-km altitude (CAMEX, 9/26/93, 2035-2053 UTC). Several small convective cells indicated by brightness temperatures lower than 150 K are shown.

Figure 2 (p. 20): Strip map images of oceanic convection observed by the MIR on the ER-2 at 20-km altitude (CAMEX, 9/26/93, 2058-2116 UTC). The anvil region of the raincell near the cursor (2104) is clearly outlined by the 325 GHz channels.

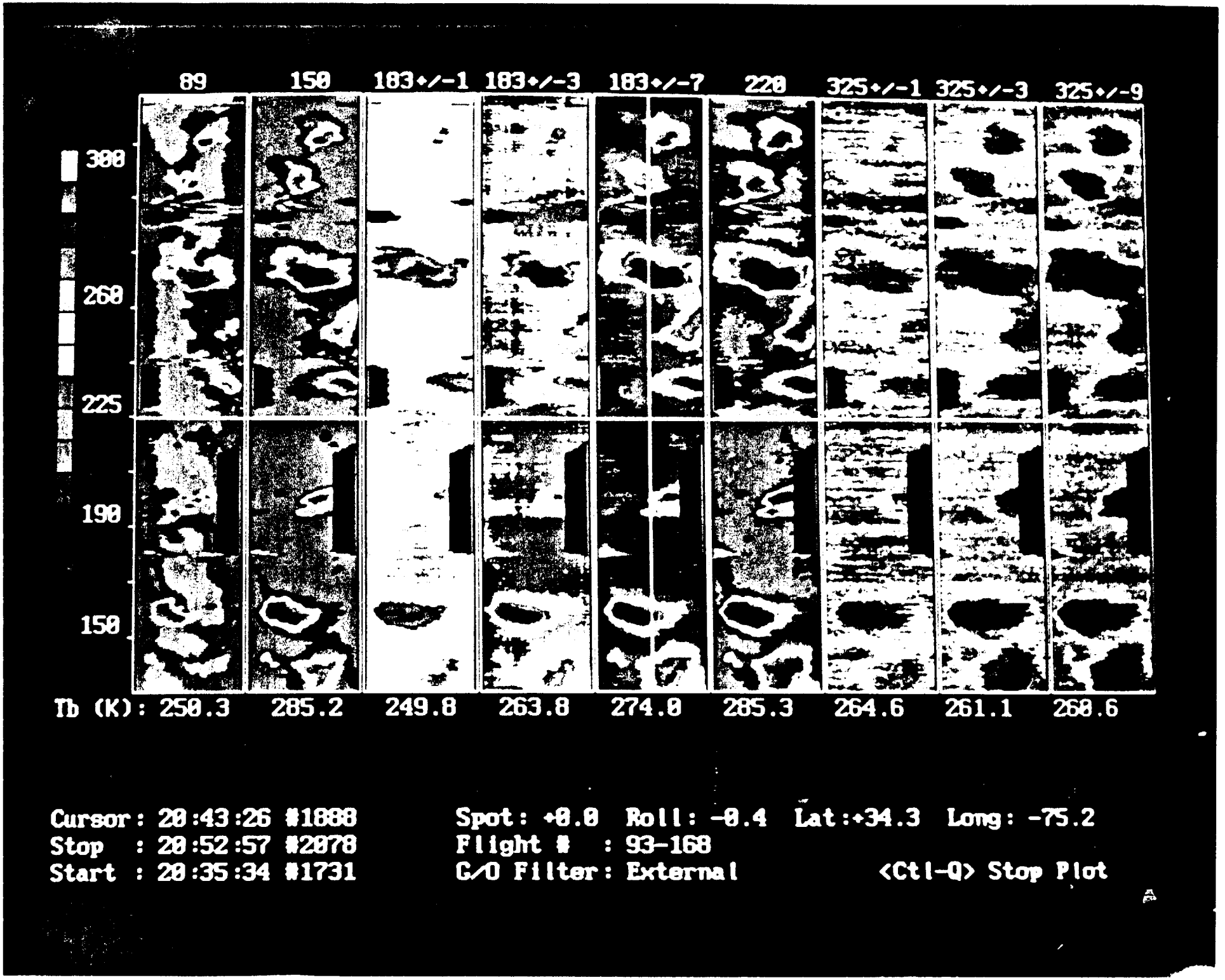
89
150
183+/-1
183+/-3
183+/-7
220
325+/-1
325+/-3
325+/-9
300
260
225
190
150
Tb (K): 250.3 285.2 249.8 263.8 274.0 285.3 264.6 261.1 260.6
Cursor: 20:43:26 #1888
Stop : 20:52:57 #2078
Start : 20:35:34 #1731
Spot: +0.0 Roll: -0.4 Lat:+34.3 Long: -75.2
Flight # : 93-168
G/O Filter: External
<Ctl-Q> Stop Plot

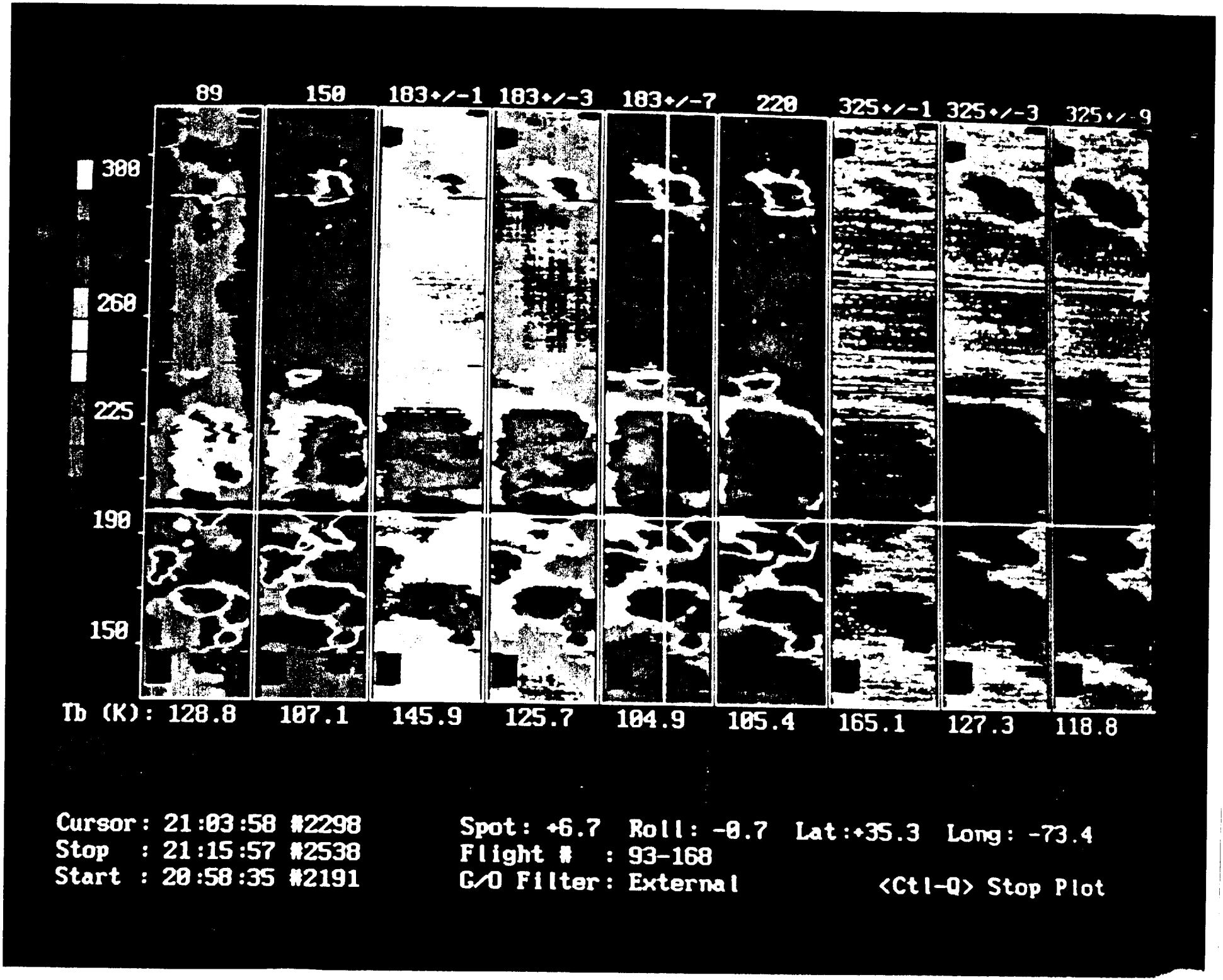
89
150
183+/-1
183+/-3
183+/-7
220
325+/-1
325+/-3
325+/-9
300
260
225
190
150
Tb (K): 128.8
107.1
145.9
125.7
104.9
105.4
165.1
127.3
118.8
Cursor: 21:03:58 #2298
Stop : 21:15:57 #2538
Start : 20:58:35 #2191
Spot: +6.7 Roll: -0.7 Lat:+35.3 Long: -73.4
Flight # : 93-168
C/O Filter: External
<Ctl-Q> Stop Plot

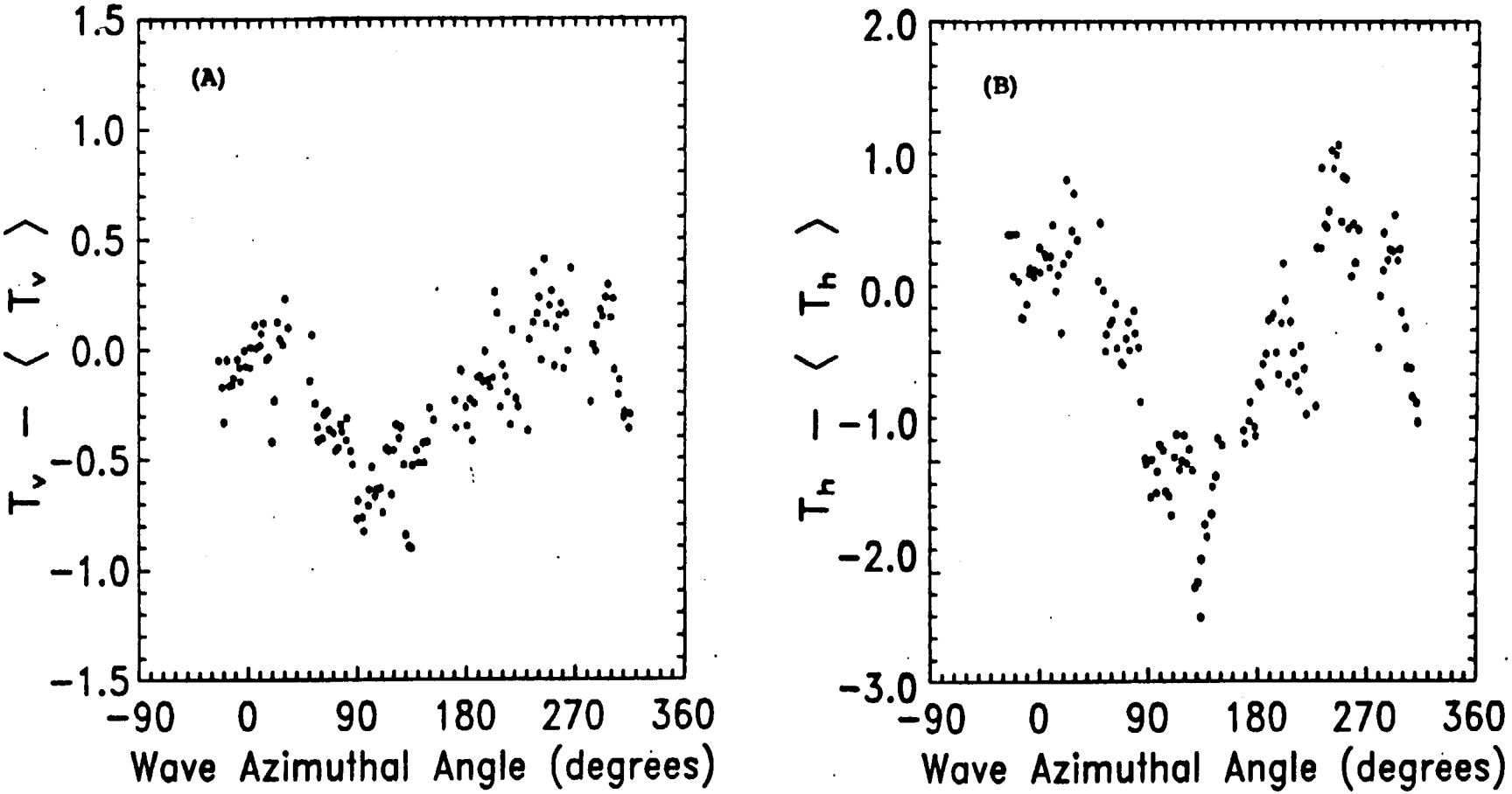

Figure 3. Vertical (A) and horizontal (B) brightness variations at 92 GHz for constant bank-angle flight over ocean during TOGA/COARE (2/8-9/93). The altitude is 1.5 km, and the radiometer beam angle is 65° from nadir. The abscissa is the angle of the beam relative to the estimated direction of the ocean waves.

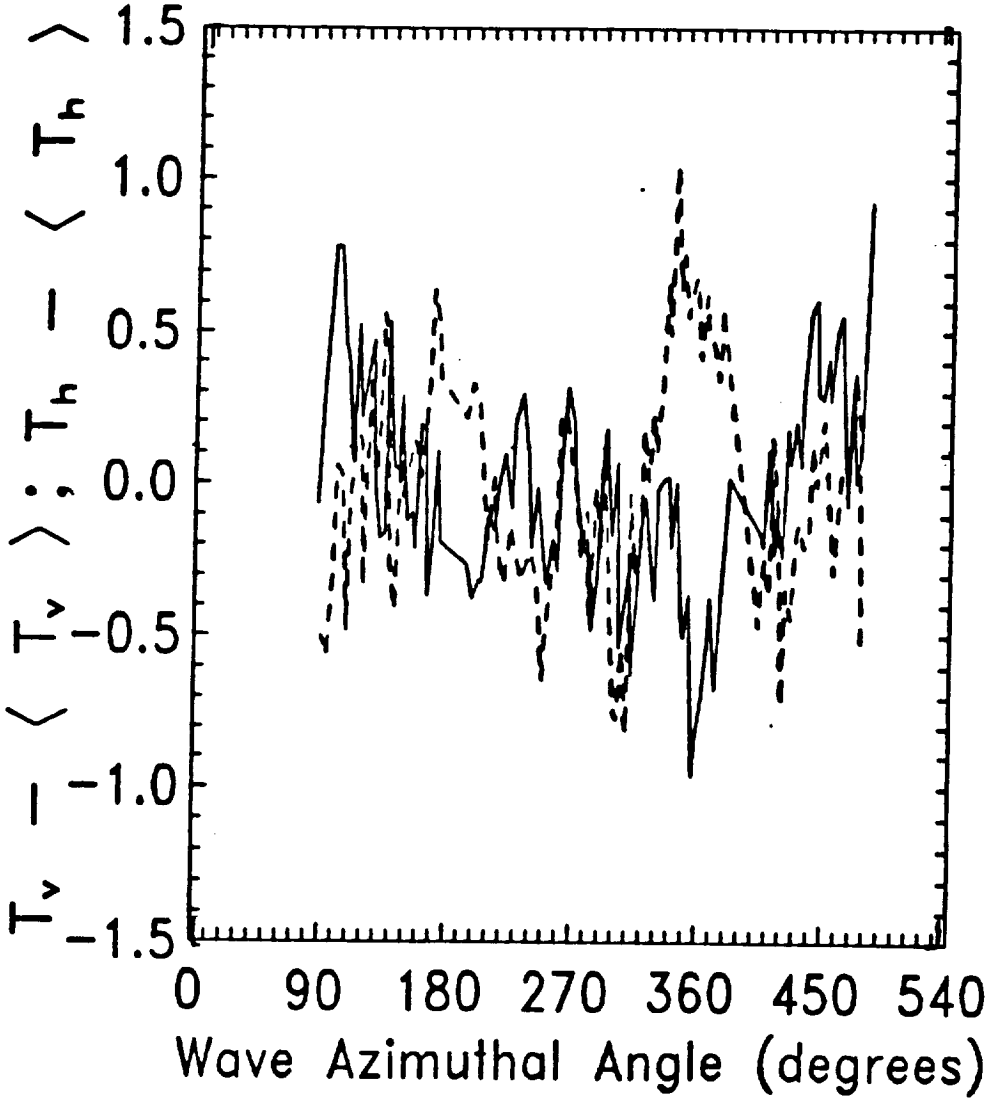

Figure 4. Vertical (solid) and horizontal (dashed) brightness variations at 92 GHz for constant bank-angle flight over ocean during an integration flight in preparation for TOGA/COARE (12/12/92). The altitude is 1.3 km, and the radiometer beam angle is approximately at nadir. The abscissa is the angle of the beam relative to the estimated direction of the ocean waves. The vertical and horizontal brightness temperatures are antiphased and of second harmonic variation.

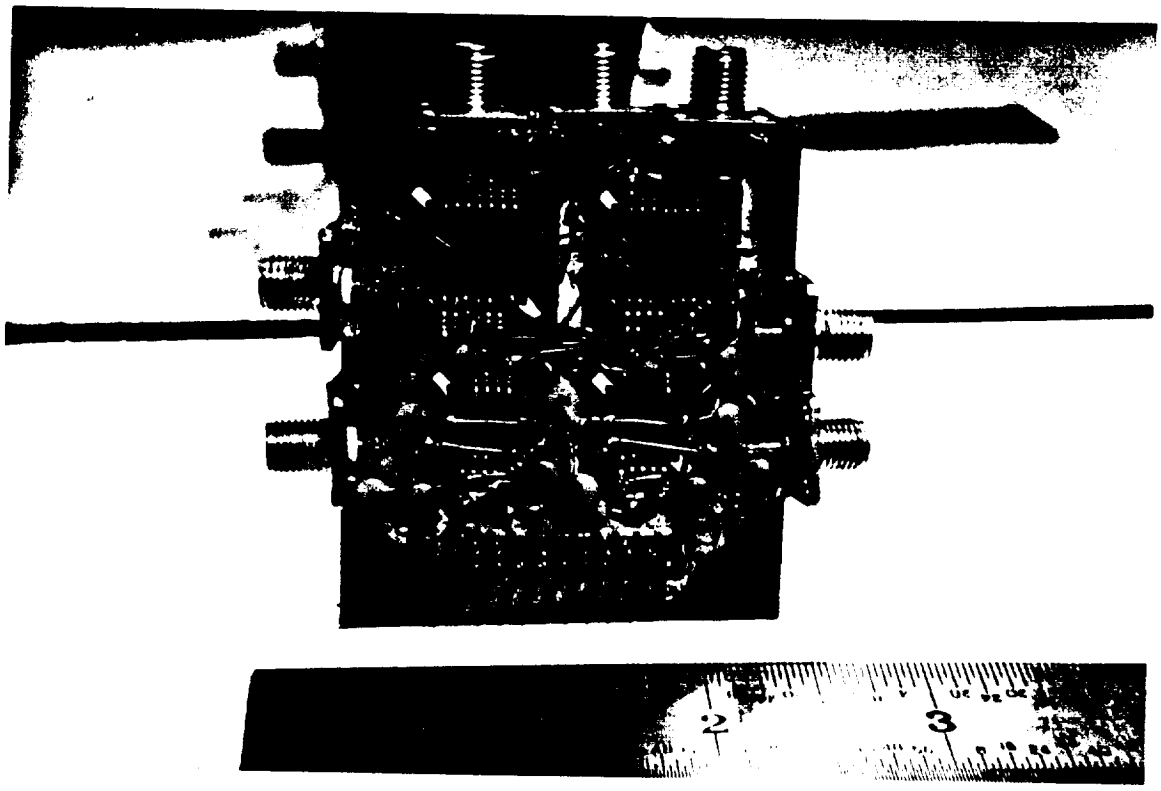

Figure 5. High-speed A/D converters for use in digital correlation polarimetric radiometry. The frequency of operation is approximately 800 Ms/sec.

Appendices A-C.

Millimeter-Wave Radiometric Observations of the Troposphere: A Comparison of Measurements and Calculations Based on Radiosonde and Raman Lidar

Submitted to:
IEEE Transactions on Geoscience and Remote Sensing
2 December 1993

by
David M. Jackson
and
A. J. Gasiewski

School of Electrical and Computer Engineering
Georgia Institute of Technology
Atlanta GA 30332-0250

Abstract

A comparison of clear-air brightness temperatures is performed between radiometric measurements and atmospheric radiative transfer calculations. The measurements were made using the NASA Goddard Space Flight Center's Millimeter-wave Imaging Radiometer (MIR) in a series of airborne and ground-based atmospheric experiments at six millimeter-wave frequencies: 89, 150, 183.3±1,±3,±7, and 220 GHz. With the inclusion of the 220 GHz channel, these measurements are the first passive observations of the atmosphere made simultaneously at the six frequencies. The MIR was operated concurrently with supporting meteorological instruments (radiosonde and Raman lidar) to construct a paired set of both spatially and temporally coincident calibrated brightness temperatures and atmospheric profile parameters. Calculated brightness temperatures based on the measured atmospheric profile parameters were obtained using a numerical radiative transfer model. Incremental water-vapor weighting functions were used to study the impact of radiosonde hygrometer errors on the radiative transfer calculations. The aircraft-based brightness temperature comparisons are generally good for the channels sensitive to the lower atmospheric levels (89, 150, 183.3±7 and 220 GHz), but show discrepancies of up to 11 K for the opaque channels (183.3±1, and ±3 GHz) caused primarily by radiosonde bias. The ground-based calculations are similarly found to be sensitive to hygrometer errors in the lower atmosphere. Ground-based comparisons between MIR observations and lidar-based calculations are typically within ±6 K.

1.0 Introduction

In constructing water-vapor profile retrieval algorithms using spaceborne passive millimeter-wave observations the relationship between the profiles and upwelling radiation must be known. Radiometric channels for water-vapor profile retrieval include those near the weak 22.235 GHz water-vapor absorption line and the stronger 183.310 GHz line. Recently, the potential uses of the 325.153 GHz water-vapor line have also been identified for the spaceborne retrieval of tropospheric water-vapor profiles and cloud parameters [1]. In developing retrieval algorithms using these lines, verification data is required consisting of radiosonde measurements of temperature, pressure, and water-vapor density profiles. However, the accuracy of a candidate water-vapor retrieval algorithm is limited by the accuracy of the radiosonde data. Comparisons between clear-air multispectral brightness temperatures from a radiometer and radiative transfer calculations can be used to investigate the impact of radiosonde errors on retrievals.

Currently, tropospheric sounding facilities in the continental United States use at least three different radiosonde packages: AIR, VIZ, and Vaisala. Both radiosonde hygrometer errors [2] and differences in relative humidity reporting practices [3] have been noted. Such errors at specific altitude levels will influence brightness calculations for channels sensitive to that level through the relative humidity weighting functions. These functions express the response of a radiometric observing system to small perturbations in the water-vapor density profile. For example, for spaceborne clear-air observations within 3 GHz of the 183.310 GHz water-vapor line, the weighting functions peak at altitudes of 7 km and above, where the corresponding relative humidity values range from 0 – 15%. Because a radiosonde hygrometer's sensitivity is monotonically related to the number density of water molecules present, their accuracy degrades in this region of the troposphere. Brightness comparisons at these channels can be expected to show this degradation as an increased discrepancy.

Clear and cloudy brightness temperature comparisons between radiometric mea-

surements and radiosonde-based radiative transfer calculations were performed by Westwater *et al.* [4] and England *et al.* [5] for ground-based vertical-angle observations and for frequencies up to 90 GHz. Mid-altitude ($\lesssim$9 km) aircraft-based comparisons were performed at 89 and 157 GHz by Foot *et al.* [6] (zenith- and nadir-directed) and English *et al.* [7] (zenith-directed) to study water-vapor continuum absorption. For these frequencies the water-vapor weighting functions show no appreciable sensitivity to water-vapor perturbations in the upper troposphere. Detailed satellite-based comparisons at 89, 150, and 183.3±1,±3,±7 GHz have also been performed by Falcone *et al.* [8] and Morrissey *et al.* [9], but were impeded by the sensor's relatively large field-of-view (~50-80 km) and the subsequent difficulties in modeling the observed background and the horizontal variability of water-vapor density in the atmosphere. In the above investigations, the effects of radiosonde "dry-end" upper atmosphere reporting errors on the theoretical calculations were not reported.

In this paper, we compare the observations made with the NASA Goddard Space Flight Center's Millimeter-wave Imaging Radiometer (MIR) and radiative transfer calculations based on simultaneous and collocated radiosonde and Raman lidar measurements. The MIR is a cross-track scanning aircraft-based radiometer currently operating with the following six millimeter-wave (MMW) channels: 89, 150, 183.3±1,±3,±7, and 220 GHz, and with provisions for three submillimeter-wave channels at 325.2±1,±3, and ±8.5 GHz. In this investigation the MIR flew aboard NASA's high altitude (~20 km) ER-2 aircraft during deployments out of the NASA Wallops Flight Facility, VA, and the NASA Ames Research Center, Moffet Field, CA. Brightness comparisons are made over both land and ocean backgrounds. Water-vapor weighting functions are developed for the MIR's frequencies and for both zenith- and nadir-directed observation geometries. Results of ground-based zenith-directed comparisons are also discussed. A preliminary study has been done by Wang *et al.* [10] for a subset of the above aircraft-based MIR comparisons.

2.0 Millimeter-wave Radiative Transfer and Radiometry

2.1 Radiative Transfer Theory

The absorption and emission of microwave radiation by the atmosphere exhibits resonances due to transitions among the quantum energy states of several molecular constituents. The water-vapor absorption resonance at 183.310 GHz, and the oxygen resonance at 118.750 GHz, are most important in the frequency range of this study, as shown in Fig. 1. The absorption near these opaque lines, as well as the continuum absorption near the window frequencies of 90, 150, and 220 GHz, is a function of the local pressure (P), temperature (T), and the density (ρ) of the absorbing constituents. Absorption models (e.g. [11], [12]) relate vertical distributions of P, T, and the constituent ρ's to profiles of the absorption coefficient, $\alpha(f,z)$, where f is the frequency and z is the altitude. The integrated radiative transfer equation (IRTE) relates the observed radiant energy to profiles of absorption coefficient and the intensity along a propagation path to the observer [13]. The radiation field is typically characterized by a brightness temperature, defined by scaling the radiation intensity (in W/m^2-St-Hz) by $\lambda^2/2k$, where λ is the wavelength and k is Boltzmann's constant. Using this definition, the brightness temperature for a blackbody radiator at physical temperature T is:

$$T_B(f) = \frac{hf}{k\,(e^{hf/kT} - 1)} \tag{1}$$

where h is Planck's constant. Note that this definition for brightness temperature differs from the Rayleigh-Jeans approximation [14], wherein Eq. (1) is expanded to first order in hf/kT and leads to $T_B(f) = T$.

For a clear and horizontally-stratified atmosphere, the brightness temperature observed at angle θ relative to the zenith for downward-looking platforms at height h is:

$$T_B(f,h,\theta) = \int_0^h T_{Bz}(f,z)\,\alpha(f,z)\sec\theta\, e^{-\tau(f,z,h)\sec\theta} dz + e^{-\tau(f,0,h)\sec\theta} T_{B0}(f,\theta) \qquad (2)$$

for $|\theta| < (\pi/2)$, where

$$T_{B0}(f,\theta) = (1-r(\theta))T_{Bs} + r(\theta)\left(\int_0^\infty T_{Bz}(f,z)\,\alpha(f,z)\sec\theta\, e^{-\tau(f,0,z)\sec\theta} dz + e^{-\tau(f,0,\infty)\sec\theta} T_{CB}\right) \qquad (3)$$

T_{Bs} and T_{CB} are the surface and cosmic background brightness temperatures, respectively. $T_{Bz}(f,z)$ is the local brightness temperature determined using Eq. (1). The integrated opacity over the path interval $[h_1,h_2]$ is:

$$\tau(f,h_1,h_2) = \int_{h_1}^{h_2} \alpha(f,z)\,dz \qquad (4)$$

In Eq. (3), the specular surface reflectivity $r(\theta)$ represents the fraction of power reflected by the surface that is copolarized with the observing instrument's antenna. Over an ocean background $r(\theta)$ is a function of frequency and surface roughness, whereas over land $r(\theta)$ is typically small ($\lesssim 10\%$), broadband, and largely independent of angle. For ground-based, upward-looking observations, the brightness temperature is:

$$T_B(f,h,\theta) = \int_0^\infty T_{Bz}(f,z)\,\alpha(f,z)\sec\theta\, e^{-\tau(f,z,0)\sec\theta} dz + e^{-\tau(f,\infty,0)\sec\theta} T_{CB} \qquad (5)$$

for $|\theta| > (\pi/2)$.

Note that the IRTE (Eqs. (2) or (5)) is exact in as far as no approximations are made in Eq. (1) for brightness temperatures. However, in obtaining $T_B(f,h,\theta)$, it is more convenient to work with expressions involving physical temperatures rather than brightness tem-

peratures. To this end, we substitute Eq. (1), expanded to second-order in hf/kT, for $T_{Bz}(f,z)$ in Eqs. (2), (3), and (5), and for T_{Bs} in Eq. (3). Equation (1) with no approximation is substituted for T_{CB}, where $T = T_c$ and T_c is the cosmic background temperature 2.73 K. As a consequence of these substitutions, T_{CB} is now defined as [15]:

$$T_{CB} = \frac{hf}{2k}\left(\frac{e^{hf/kT_c}+1}{e^{hf/kT_c}-1}\right) \tag{6}$$

and $T_B(f,h,\theta)$ now implicitly contains a second-order correction, i.e., in Eqs. (2) and (5) $T_B(f,h,\theta)$ is now interpreted as $T_B(f,h,\theta)+hf/2k$. Due to the nonlinearity in brightness temperature with physical temperature for temperatures near T_c, the second-order correction is adjusted by T_{CB} from Eq. (6). In using Eq. (1) to second order, $T_B(f)$ is accurate to ~0.15 K for frequencies up to 340 GHz and for atmospheric temperatures as low as 150 K. In contrast, the maximum error incurred using the Rayleigh-Jeans approximation over this range is 8 K.

2.2 Incremental Weighting Functions

The IRTE is nonlinear in the relevant atmospheric parameters (i.e., P, T, and particularly the constituent ρ's) due to their influence on the absorption coefficient α, which enters the equations in a nonlinear manner. However, weighting functions for particular atmospheric parameters can be determined by linearizing the IRTE, where the respective parameter is incrementally changed from a nominal value. Incremental weighting functions express the brightness temperature response of an observing system to small perturbations in the atmospheric parameters of interest. In the present study, we are interested in the effects of perturbations in the water-vapor density profile on observed brightness temperatures caused by radiosonde errors. Incremental water-vapor weighting functions for the special case of vertical viewing angles in downward-looking and upward-looking observing systems have been discussed by Schaerer and Wilheit [16], and Westwater *et. al.* [4], respectively.

To linearize the IRTE, we seek brightness changes δT_B caused by deviations in both the temperature $\delta T(z)$ and absorption coefficient $\delta\alpha(z)$ from their nominal profiles. For microwave absorption in the troposphere, the absorption coefficient $\alpha(f,z)$ is a function of $T(z)$ and $\rho_v(z)$, i.e., $\alpha = \alpha(T, \rho_v)$. Using Eq. (4), the absorption perturbation leads to an opacity perturbation, given to first order by:

$$\delta\tau(z) = \left(\frac{\partial\alpha}{\partial T}\delta T + \frac{\partial\alpha}{\partial\rho_v}\delta\rho_v\right)\delta z \tag{7}$$

where δz is the thickness of the perturbed layer. The corresponding change in brightness temperature to perturbations at height z is:

$$\delta T_B(z) = \frac{\partial T_B}{\partial T(z)}\delta T(z) + \frac{\partial T_B}{\partial\tau(z)}\delta\tau(z) \tag{8}$$

From perturbation analysis, the two terms on the right-hand side of Eq. (8) can be determined directly from Eqs. (2) or (5), where we use physical temperatures for brightness temperatures. For downward-looking observations we can write δT_B as:

$$\delta T_B = \int_0^h W_T(z,\theta)\,\delta T(z)\sec\theta\,dz + \int_0^h W_{\rho_v}(z,\theta)\,\delta\rho_v(z)\sec\theta\,dz \tag{9}$$

where the incremental temperature weighting function, $W_T(z,\theta)$, is given by:

$$W_T(z,\theta) = \alpha(f,z)\sec\theta\left(e^{-\tau(f,z,h)\sec\theta} + r(\theta)e^{-\tau(f,0,h)\sec\theta}e^{-\tau(f,0,z)\sec\theta}\right) \tag{10}$$

$$+\frac{\partial\alpha}{\partial T}\sec\theta\left\{T(z)e^{-\tau(f,z,h)\sec\theta} - \int_0^z T(z')\,\alpha(f,z')\sec\theta\,e^{-\tau(f,z',h)\sec\theta}dz'\right.$$

$$\left. - B(z,\theta)\,e^{-\tau(f,0,h)\sec\theta}\right\}$$

and the background term $B(z,\theta)$ is:

$$B(z,\theta) = (1-r(\theta))T_s + r(\theta)\left\{ 2T_{CB}\, e^{-\tau(f,0,\infty)\sec\theta} - T(z)e^{-\tau(f,0,z)\sec\theta} \right. \tag{11}$$

$$\left. + \int_0^{\infty} T(z')\,\alpha(f,z')\sec\theta\, e^{-\tau(f,0,z')\sec\theta}dz' + \int_z^{\infty} T(z')\,\alpha(f,z')\sec\theta\, e^{-\tau(f,0,z')\sec\theta}dz' \right\}$$

The downward-looking incremental water-vapor density weighting function, $W_{\rho_v}(z,\theta)$, is:

$$W_{\rho_v}(z,\theta) = \frac{\partial\alpha}{\partial\rho_v}\sec\theta\left\{ T(z)e^{-\tau(f,z,h)\sec\theta} - \int_0^{z} T(z')\,\alpha(f,z')\sec\theta\, e^{-\tau(f,z',h)\sec\theta}dz' \right. \tag{12}$$

$$\left. - B(z,\theta)\, e^{-\tau(f,0,h)\sec\theta} \right\}$$

For the ground-based upward-looking observations, the incremental temperature weighting function $W_T(z,\theta)$ is:

$$W_T(z,\theta) = \alpha(f,z)\sec\theta\, e^{-\tau(f,z,0)\sec\theta} \tag{13}$$

$$+ \frac{\partial\alpha}{\partial T}\sec\theta\, e^{-\tau(f,z,0)\sec\theta}\left\{ T(z) - T_{CB}\, e^{-\tau(f,\infty,z)\sec\theta} \right.$$

$$\left. - \int_z^{\infty} T(z')\,\alpha(f,z')\sec\theta\, e^{-\tau(f,z',z)\sec\theta}dz' \right\}$$

and the upward-looking incremental water-vapor density weighting function, $W_{\rho_v}(z,\theta)$, is:

$$W_{\rho_v}(z,\theta) = \frac{\partial\alpha}{\partial\rho_v}\sec\theta\, e^{-\tau(f,z,0)\sec\theta}\left\{ T(z) - T_{CB}\, e^{-\tau(f,\infty,z)\sec\theta} \right. \tag{14}$$

$$\left. - \int_z^{\infty} T(z')\,\alpha(f,z')\sec\theta\, e^{-\tau(f,z',z)\sec\theta}dz' \right\}$$

with T_{CB} for both observing regimes determined from Eq. (6).

The first term in the incremental weighting function $W_T(z,\theta)$ represents the linear response to temperature deviations. The terms proportional to $\partial\alpha/\partial T$ and $\partial\alpha/\partial\rho_v$ in Eqs. (10), (13), and Eqs. (12), (14), respectively, describe the IRTE's departure from strict linearity with the absorbing constituent in question. These terms also show that the difference in functional form of the response to T and ρ_v is due only to the multiplicative factors $\partial\alpha/\partial T$ or $\partial\alpha/\partial\rho_v$, respectively. Since α is relatively insensitive to T, $\partial\alpha/\partial T$ is often considered negligible (e.g., [17]) and the IRTE is considered linear in T.

In Figs. 2 and 3, incremental weighting functions $W_{\rho_v}(z,\theta)$ for aircraft- and ground-based geometries are shown for U.S. standard summer mid-latitude atmospheric conditions [18] using an exponential water-vapor density profile with a 2-km scale-height and a surface relative humidity (SRH) of 75%. The plots are of relative humidity weighting functions, which are related to water-vapor density weighting functions by:

$$W_R(z,\theta) = W_{\rho_v}(z,\theta)\frac{\rho_{sat}(z)}{100} \tag{15}$$

where $\rho_{sat}(z)$ is the saturation water-vapor density [19]. Figure 2 shows downward-viewing (at nadir) relative humidity weighting functions computed over both an ocean (Fig. 2a) and land background (Fig. 2b) at several MMW frequencies. In Fig. 3 ground-based zenith-viewing weighting functions are shown for the same frequencies. Given an assumed relative humidity perturbation δR over thickness δz, brightness temperature perturbations can be determined directly from these figures.

As expected, the peaks of the 183-GHz downward-viewing relative humidity weighting functions move lower into the atmosphere for frequencies progressively farther from 183.310 GHz resonance. For example, observations with the 183.3±1 and 183.3±7 GHz channels are most sensitive to radiation originating from altitudes of 8-12 km and 3-6 km,

respectively. The sign of window-channel weighting functions can change, as seen in their response over a land background (Fig. 2b) and in the 220 GHz channel over ocean (Fig. 2a). Therefore, positive-valued hygrometer errors in the atmospheric levels above 3 km can decrease brightness temperature calculations, and in the lower levels can increase brightness temperatures. The weighting functions are dependent on the unperturbed nominal temperature and relative humidity profiles. However, if the SRH deviates from 75% (consistent with the radiosonde profiles collected for this study) by ±20% RH the magnitude of the weighting function peaks and their positions are not significantly changed. Note that for upward-viewing observations (Fig. 3), the 150 GHz channel is the most sensitive to water-vapor perturbations in the lower atmosphere.

2.3 Millimeter-wave Radiometric Principles

For an incident unpolarized brightness field $T_B(f, h, \Omega)$, where Ω is the propagation direction, the antenna temperature T_A of a radiometer can be expressed in terms of the radiometer's antenna gain pattern $G(\Omega)$ and normalized receiver frequency response $H(f)$ as:

$$T_A(h) = \frac{1}{4\pi\beta}\int_0^\infty |H(f)|^2 \int_{4\pi} G(\Omega)\, T_B(f, h, \Omega)\, d\Omega df \qquad (16)$$

where $\beta = \int_0^\infty |H(f)|^2 df$ is a spectral normalization factor and h is the radiometer's height. Thus, the measured temperature T_A is a weighted average of the brightness temperature reaching the receiver from all directions in space and from all frequencies in the receiver passband. In practice, the bulk of the received energy for most radiometers enters through the relatively narrow main beam of the antenna.

The underlying atmospheric thermal emission observed by the radiometer is a random process. The resulting measurements are estimates of the power in this process and are themselves a random process. Consequently, the radiometer output fluctuations are proportional to the sum of T_A and the receiver noise temperature, T_{rec}. The resulting sensitivity, or

minimum detectable temperature, of a total-power radiometer is given by:

$$\Delta T_{rms} = (T_A + T_{rec})\sqrt{\frac{1}{B\tau} + \left(\frac{\sigma_g}{\langle g \rangle}\right)^2} \tag{17}$$

where B is the IF channel (3-dB) bandwidth, τ is the post-detection integration time, and $(\sigma_g/\langle g \rangle)^2$ is the relative predetection gain variance. The gain variations occur at time intervals much less than a typical calibration interval (~1-2 sec). To minimize the error in the estimate of T_A, it is desirable to increase the radiometer bandwidth (B) and integration time (τ). However, for practical measurements, the bandwidth is limited by the need for both detailed spectral information and interference rejection, and the integration time is limited by the required temporal sampling time.

2.4 Millimeter-wave Imaging Radiometer Description

The Millimeter-wave Imaging Radiometer (MIR) is a total power six-channel imaging spectrometer designed for airborne studies of passive microwave retrieval of tropospheric water vapor, clouds, and precipitation parameters [20]. The MIR is a cross-track scanning radiometer and can be configured for either airborne nadir-viewing aboard the NASA ER-2 high-altitude aircraft or ground-based zenith-viewing. Table I summarizes the MIR channel design specifications. The radiometric sensitivities were calculated using Eq. (17) for a 75-ms integration period, relative gain variance of 10^{-8}, and nominal antenna temperature of 200 K.

The MIR consists of a receiver housing and data acquisition system. For aircraft-based observations, the receiver housing mounts into the camera port of the ER-2 superpod nose cone. Within the receiver housing an ambient pressure cavity contains the scanning mirror, stepper motor, hot and cold calibration targets, and temperature sensors. A pressurized enclosure houses the lenses, feedhorns, mixers, IF and video hardware, and data acquisition analog and digital electronics. A PC-AT compatible computer system, mounted above

the receiver housing, executes configuration and control programs stored in a nonvolatile hard disk emulator. Digitized radiometric data received from A/D boards and system operational and diagnostic data are recorded on 8mm EXABYTE magnetic tape cartridges.

Each of the five MIR feedhorns is located at the focal point of a corresponding lens integrated into the pressurized receiver housing wall. All lens-feedhorn pairs have nearly identical 3.5° beamwidths. The five mixers are operated in a double-sideband configuration: the 89 and 150 GHz mixers are balanced; the 183.3, and 220 GHz mixers are sub-harmonically pumped. All LO's are InP Gunn oscillators where the second harmonic is extracted and used in the mixing process. After IF amplification, the radiometric signals are bandpass filtered. For the 183.3 GHz mixer, a triplexer is used to divide the IF signals into three channels. Detected signals are amplified, low-pass filtered, and subsequently, sampled by 12-bit A/D converters. DC feedback is added to each video signal via an 8-bit D/A converter. This permits in-flight adjustments to compensate for slowly varying drifts in receiver gain and noise temperature. The feedback can compensate for receiver gain variations of ±2 dB and receiver noise temperature variations of ±20%. The feedhorns are directed, in turn, to hot (~325 K) and cold (~240 K, ambient temperature) calibration targets that serve as known blackbody radiometric sources. Absolute calibration accuracy is estimated at better than 1 K from knowledge of both the temperature sensor accuracy (better than 0.1 K) and the electromagnetic scattering characteristics of the targets [21]. In-flight observations of both calibration targets indicate channel sensitivities consistent with those shown in Table I (Eq. (17)).

3.0 Description of Experiments

3.1 Wallops Experiments, July-August, 1992

Simultaneous and collocated measurements involving the MIR, a Raman lidar, and radiosondes were performed on five days between 29 July and 6 August 1992, at the NASA Wallops Island Flight Facility, Virginia. Motivation for these experiments included using MIR data to validate the calibration accuracy of the Special Sensor Microwave (SSM/T-2)

water vapor sounder [8], collecting data for future water-vapor retrieval comparisons, and performing clear-air brightness temperature comparisons. Statistics for MIR-observed brightness temperatures, over ocean and land backgrounds, are shown in Table II. The statistics are computed from successive nadir samples taken over 1-2 minutes during selected periods of each flight. For the comparisons, MIR observations and calculations derived from radiosonde and ground-based Raman lidar data are used. Both ground-based and aircraft-based experiments were made with the MIR.

Ground-based observations were performed over a 100° swath centered at zenith from 2200 to 0300 UTC on 29-30 and 30-31 July 1992. The observations were made during clear and stable atmospheric conditions and within 5 km of an active radiosonde network. Aircraft-based observations were made from the NASA high-altitude ER-2 aircraft during overflights of both coastal regions near the Wallops Island facility, and ocean flight-tracks, parallel to the coastline, approximately 200 km offshore. Three 6.5-hour and two 3-hour flights were made during local nighttime conditions, as summarized in Table III. A total of 27 Wallops radiosonde profiles were used in the clear-air comparisons. Temporal and spatial collocation differences were typically better than 45 minutes and 20 km, respectively, between ER-2 positions, radiosonde launches, and Raman lidar observations. Data from the Cape Cod flight segments were used for SSM/T-2 calibration studies.

A typical brightness temperature time-series is shown in Fig. 4, for the 29 July flight from 0900 to 0917 UTC (ocean to land flight track), and 0928 to 0940 UTC (land to ocean return flight track). As expected, the values of opaque-channel brightness temperatures (Fig. 4a) increase with increasing offset from 183.3 GHz and are not responsive to the land-ocean background transitions. Relatively large brightness temperature changes are evident in the 89 GHz (~60 K) and 150 GHz (~18 K) window-channel observations (Fig. 4b) for both the island-ocean boundary at 9:09-9:13 UTC and at 9:28-9:32 UTC. The cooler brightness temperatures over ocean are the result of an increased contribution from the cold ocean-reflected cosmic background radiation.

A 355 nm Raman lidar [22] was deployed at Wallops Island during the five ER-2 overflights and the ground-based experiments. The Raman component of molecular scattering is characterized by a unique shift in frequency relative to that of the incident excitation, and thus unambiguously indicates the density of the scattering species. However, molecular Raman scattering is relatively weak compared to Rayleigh scattering from molecules or Mie scattering from atmospheric aerosols. Thus, the system could only be operated at night. At a given altitude, the water-vapor mixing ratio, defined as the mass of water vapor per unit mass of dry air [19], can be determined from the Raman-shifted return signals from water vapor and nitrogen. The lidar was deployed on a mobile platform, capable of making both zenith observations and range-height indicator (RHI) maps. A detailed description of the Raman lidar system and water-vapor retrieval algorithm can be found in Whiteman *et. al* [23]. A total of 40 Wallops lidar profiles were used in the clear-air comparisons.

3.2 Ames Flights, May 1992

The MIR flew on the ER-2 out of NASA Ames, Moffet Field, CA, during two flights on 14-15 May and 15-16 May 1992 over the land and coastal waters of southwestern California (Table III). Statistics of MIR-observed brightness temperatures for these flights are shown in Table II. The two flight tracks were nearly identical and included overflights of San Nicolas and Santa Catalina Islands, and were within 60 km of Point Mugu Naval Air Station. The selection of MIR observations for cloud-free regions was facilitated by viewing data from the visible and IR channels of the Airborne Oceanographic Color Imager (AOCI Daedalus), which was operating on both late-afternoon flights. For the clear-air comparisons, data from a total of six San Nicolas and Point Mugu radiosonde launches were used. The maximum temporal and spatial collocation differences between ER-2 positions and the radiosonde launches were 1 hour and 100 km, respectively.

A nadiral brightness temperature time-series for the MIR is shown in Fig. 5 for the 14-15 May flight from 0:12:00 to 0:30:00 UTC, corresponding to overflights of Los Angeles and its coastline (land to ocean) and Santa Catalina Island. The 183.3±1 GHz channel

(Fig. 5a) detects a gradual decrease in the water vapor of the upper atmospheric levels, manifested by a ~15 K brightness temperature increase. Relatively large brightness temperature changes (40-80 K) are again evident in the window-channel observations (Fig. 5b) of both the land-ocean boundary at 0:19:30 and Santa Catalina Island at 0:22:30, particularly in the 89 and 150 GHz channels. Over land, brightness temperature fluctuations of up to 20 K in the 89 GHz channel show the effects of the variable background emissivity.

3.3 Radiosonde and Raman Lidar Atmospheric Profiles

Radiosondes offer the most accepted means of obtaining verification measurements of the principle atmospheric profile parameters: temperature, pressure, and water-vapor density. For the Wallops experiments, single-, dual-, and triple-soundings were performed using AIR, VIZ, and Vaisala radiosondes. Balloons were launched at three-hour intervals from approximately 1800 to 0600 hours, local time. Multiple sounding packages were suspended from the same balloon, less than one meter apart, thus allowing each instrument to sample the same horizontal layer in the atmosphere. The three radiosonde packages differ primarily in the type of hygrometer used: the Vaisala type employs a capacitive hygrometer (Humicap) based on a hygroscopic dielectric material, and the AIR and VIZ types both employ carbon hygristors but use different relative humidity reporting (calibration) practices. Data from a relative humidity triple-sounding is shown in Fig. 6, taken at 0700 UTC on 29 July at Wallops Island. Also in Fig. 6, a coincident Raman lidar profile is shown, observed from a site approximately 1 km from the balloon launch. Due to the weak Raman backscatter phenomena and sensitivity limitations in the lidar detectors, the maximum altitude for Raman-lidar derived water vapor profiles was limited to approximately 9.5 km. The radiosondes used in the Ames-based experiments were part of the Meteorological Rawinsonde System based at San Nicolas and Point Mugu and employ Vaisala Humicap hygrometers. Temperature sensor differences among these radiosondes (AIR and Vaisala) of 1-2 K have been noted [10], and their absolute accuracy is ±0.5 K. A standard error-propagation analysis using IRTE calculations shows that the magnitude of the brightness temperature

bias associated with a ±1-2 K sensor bias at every level is 1 K or less for all MIR channels.

The large relative humidity discrepancies evident in Fig. 6 between the radiosonde sensors is of concern in intercomparison studies [3]. In particular, above 8 km the AIR sensor's dry-end limit was found to be approximately 20% RH; this is consistent with previous hygristor studies [24]. The VIZ sensor, which uses a different calibration process than that for the AIR [25], and the Viasala sensor showed up to a 20% RH disagreement in the 8-16 km levels. Here, the VIZ and Vaisala discrepancy is consistent with a previous intercomparison of the two instruments [26]. Up to the 6 km level (500 mb) there is good agreement in AIR, Vaisala, and lidar water-vapor reporting. The relative humidity bias due to temperature sensor thermal-lag (~1-2K warmer than ambient up to the 500 mb level) [27] is reported to be –4% RH [25] for AIR and VIZ hygrometers. Apparently due to dry-end limit calibration difficulties the thermal-lag bias was not seen in the Wallops or Ames profiles and thus was not studied here. A standard error-propagation analysis using IRTE calculations shows that the brightness temperature variation associated with a hygrometer variation of +5% RH at every level is approximately +3.5 K and +2.0 K for the 89 and 150 GHz channels, respectively, and less than –1.5 K for the other channels. The implications of the upper-tropospheric relative humidity reporting errors on comparisons with MMW radiometric observations are discussed in the next section.

4.0 Clear Air Intercomparisons

Radiative transfer calculations were performed using an iterative numerical model applicable for a horizontally-stratified clear atmosphere [28]. The Liebe water-vapor absorption model [11] and the Rosenkranz oxygen absorption model [12] were used to relate the radiosonde and Raman lidar profile data to absorption coefficient profiles. Profile data were obtained by sampling the radiosonde measurements and lidar observations along a nearly uniform altitude grid from 0 to 20 km, i.e., ~150 m spacing from 0 to 10 km, and 500 m spacing from 10 to 20 km. Of the four instrument types (AIR, VIZ, Vaisala, and lidar) the AIR

data were typically the most complete and included more than 60 levels. Some VIZ data suffered from grid spacings of up to 2 km below the 10 km level due to the data files becoming corrupted. In these cases, the VIZ profiles were augmented with AIR data for those levels. Also, a few VIZ and Vaisala data sets were empty above approximately 12 km and were augmented with standard mid-latitude exponential water-vapor atmospheres, 37° N for August at Wallops, and 33° N for May at Ames. For levels in the lidar data above 9.5 km, both AIR and Vaisala data were used to augment the profiles. For this study all radiosonde and lidar profiles were considered as zenith measurements.

The effect of a non-ideal antenna gain pattern on the calculated brightness temperatures was significant for the zenith-directed ground-based observations. For example, using Eq. (16) with a representative antenna gain pattern, a brightness variation of +50 K from zenith to a scan-angle of ±45° (typical) biases the zenith observation by +0.7 K. For the aircraft-based observations, brightness variations were less than 10 K over the scan-range and therefore did not significantly perturb the nadiral measurements.

4.1 Aircraft-based comparisons

The results of the aircraft-based brightness temperature comparisons are shown in Tables IV and V for Wallops-based experiments over ocean and land backgrounds, respectively, and in Table VI for Ames-based experiments over an ocean background. The ocean was modeled as a specularly reflecting surface using the Fresnel reflectivities. No surface-foam was considered due to the relatively calm conditions throughout both experiment areas, and ocean surface roughness was neglected. Sea surface temperatures were determined from seasonal means for the coastal Pacific in May and the Atlantic in July [29]. Land background emissivities were considered frequency independent and uniform with zenith angle θ.

The three comparisons with the radiosonde instruments in Table IV, and the one in both Tables V and VI, are generally good except for the 183.3±1 channel. Here the effects of

the AIR dry-atmosphere reporting errors are the most pronounced, and differences of −10.9 K are seen. Because of the sign (negative) of $W_{\rho_v}(z, \theta)$ at altitudes from 8-12 km (Fig. 2a), the excessive moisture reported in the higher levels by the AIR radiosonde reduces the computed opaque-channel (183.3±1 and 183.3±3 GHz) brightness temperatures. For example, a +20% RH perturbation from 8 to 20 km results in a brightness temperature perturbation of −8 to −10 K at 183.3±1 GHz. Similarly, VIZ comparisons also show a significant (but smaller) discrepancy for the 183.3±1 channel, which is also due to upper level hygristor reporting errors. However, since three of the nine VIZ profiles were augmented with AIR upper-level data, some of this discrepancy also can be ascribed to the AIR. Vaisala comparisons exhibit the best agreement of the radiosondes types, with the 89 and 150 GHz channels showing the worst agreement for this instrument. For these two channels, the biases are nearly the same magnitude and are likely due to the under-reporting of water vapor in the lower atmosphere by the Vaisala's Humicap sensor.

The lidar comparisons exhibit their best agreement at 89 and 150 GHz (Tables IV and V). These channels are most sensitive to water-vapor profiles from 0 to 9.5 km, corresponding to the levels where lidar data is available. Lidar levels from 9.5-20 km were filled with the corresponding data from both AIR and Vaisala profiles. The lidar (w/AIR) upper-level comparisons, i.e., those for the remaining four channels, are similar to AIR results, particularly for the 183.3±1 channel. Whereas this similarity is probably due to gross AIR dry-atmosphere reporting errors dominating the comparisons, the widely differing upper-level lidar(w/Vaisala) and Vaisala comparisons are more difficult to explain. Because the Vaisala hygrometer more accurately reports the upper-level water-vapor profiles, the discontinuous transition between the Vaisala and lidar profiles might be dominating the comparison and causing the upper-level lidar (w/Vaisala) and Vaisala discrepancy.

For the 89 and 150 GHz comparisons in Tables IV and VI, variations in ocean-surface emission can explain the standard deviations of up to ~5 K. For example, a ±3% variation in surface emissivity can lead to a 2 K and 1 K change in calculated 89 and 150 GHz

brightness temperatures, respectively. Also, the relatively large standard deviations in the lidar comparisons in Table V are likely due to modeling errors of the land-surface emissivity.

4.2 Ground-based comparisons

Brightness temperature comparisons for the two ground-based experiments at NASA Wallops are shown in Fig. 7 for 29-30 July, and Fig. 8 for 30-31 July. Local weather conditions at the outset of both experiments were similar and unusually clear and dry (~50-75% SRH) for coastal Virginia in July. During the first night's experiment the atmosphere was characterized by an increase in relative humidity at lower levels, manifested by a brightness temperature increase (5-10 K) for the less opaque channels, 89, 150, and 220 GHz (Fig. 7a). Conversely, for the 30 July experiment there was a decrease in relative humidity at lower levels, manifested as a 5-10 K decrease in the same channels (Fig. 8a). The sensitivity of these channels to changes in relative humidity is consistent with the behavior of the incremental weighting functions $W_{\rho_v}(z)$ (Fig. 3).

The 29-30 July brightness comparisons (Fig. 7b) were made over two time frames: a 3 hour interval for AIR-based calculations, and a 1 hour interval for lidar- and Vaisala-based calculations. The AIR comparisons show a generally increasing discrepancy over the 3 hour interval, indicating that the influence of that night's increasing relative humidity is more pronounced in the calculations than in the MIR observations. The discrepancy change is largest for the 150 and 220 GHz comparisons, which is consistent with these channels' higher sensitivity to relative humidity perturbations. The lidar and Vaisala comparisons are generally good over the 1 hour interval, except for the 150 GHz Vaisala comparison. This apparent bias may be due to a hygrometer induced error, given the 150 GHz channel is most sensitive to water-vapor perturbations.

The 30-31 July comparisons (Fig. 8b) were done over a 5 hour interval for AIR-based calculations, 3 hour interval for the Vaisala-based calculations, and 1.5 hour interval for lidar-based calculations. For the AIR comparisons we see a smaller discrepancy change rela-

tive to the 29-30 July results, but still the largest discrepancy overall. Given the ~5-10 K decrease in the observed window channel brightness temperatures over the evening, the AIR fails to indicate changes (drying) in the lower atmosphere. The Vaisala results show a negative-valued discrepancy, as was seen in the 29-30 July comparisons, but generally are in better agreement. As was found in the aircraft-based comparisons, this is most likely due to the Humicap's under-reporting of water vapor in the lower atmosphere. The comparisons with the Vaisala do indicate the effects of the decreasing relative humidity over their 3.0 hour interval. A decreasing discrepancy is seen in the lidar comparisons at 150, 220, 183.3±7, and then 89 GHz. The 220 and 183.3±7 GHz lidar results are similar and the calculations appear to over-report the effect of atmospheric drying relative to the MIR observations. Since these channels have widely different sensitivities to water-vapor perturbations, their common behavior may indicate a possible MIR measurement bias for this time frame. However, the other two radiosonde comparisons, particularly the Vaisala results, do not indicate MIR measurement difficulties during this period. The 150 GHz channel appears to be most sensitive to the apparent bias in both the AIR and lidar calculations.

The accuracy of these ground-based measurements is sensitive to the temperature of the MIR cold calibration target. The cold-target temperature is typically 250 K in-flight, and is near ambient temperature (~300 K) on the ground. The same noise or measurement uncertainty in the determination of the cold-target temperature, when the target is at 300 K, produces a calibration error approximately four times greater than that when the target is at 250 K. That is, for a ±0.1% error in the cold-target temperature, the bias in a 150 K calibrated brightness temperature would be approximately ±2.3 K for the 300 K cold target, and ±0.6 K for the 250 K target. This source of error alone, however, does not explain the disparate bias seen in comparisons based on observations made at the same, or similar, times, i.e., the AIR comparisons are almost all positive-valued, while the Vaisala are almost all negative-valued.

5.0 Conclusions

The experiments described herein use the first atmospheric observations made with the wideband MIR channel set, and include unique observations at 220 GHz. The aircraft-based comparisons of computed-less-observed brightness temperatures at the two most opaque MIR channels (183±1 and ±3 GHz) show that the AIR dry-atmosphere relative humidity reporting errors produce discrepancies of –11 K and –6.5 K, respectively, over both land and ocean backgrounds. For the 89, 150, 183.3±7 and 220 GHz channels, and for the opaque channels compared against calculations based on other radiosonde types, the aircraft-based brightness temperature comparisons are in good agreement. Since different types of hygrometer-based radiosondes and reporting practices can introduce biases in upper-level water-vapor measurements, the potential effects of radiosonde inconsistency cannot be neglected in climatological and satellite calibration/validation studies. This further suggests that aircraft- or spacecraft-based passive microwave water-vapor profile retrievals can lead to more consistent measurements, albeit with reduced vertical resolution.

For the aircraft-based comparisons in this study, the most significant radiosonde-based sources of error are (in order of importance): 1) radiosonde hygrometer non-representative calibrations and non-responsive behavior in dry environments, particularly for the AIR package; 2) hygrometer measurement uncertainty; 3) incomplete or corrupted water-vapor profile data; 4) temperature-induced humidity errors due to temperature sensor thermal-lag; and 5) inconsistent temperature sensor behavior among the representative packages. Calculations based on Raman lidar humidity data are generally in excellent agreement with MIR observations of the lower troposphere. However, upper-level comparisons are impeded by lack of lidar data above 9.5 km. The effects of atmospheric absorption-model uncertainties at millimeter wavelengths are not large enough to influence brightness temperature comparisons relative to the radiosonde errors.

Ground-based window channel calculations (particularly at 89 and 150 GHz) are

more sensitive to hygrometer errors in the lower atmosphere than are airborne nadiral calculations. For example, the ground-based relative humidity incremental weighting functions for these channels are 5-20 times larger between 0-3 km than in the airborne case. Therefore, the effects of hygrometer uncertainties (±5 RH) on the calculations are considered the dominant cause of the discrepancies reported here. Furthermore, differences between the hygrometer observations are evident by the disparate values for each respective comparison, i.e., AIR-based calculations are positive-valued for each channel, and respective Vaisala-based calculations are negative-valued. Comparisons between MIR observations and lidar-based calculations show the best agreement with discrepancies typically better than ±6 K.

Acknowledgments

The authors gratefully acknowledge the contributions from P.E. Racette and J.R. Wang of NASA Goddard Space Flight Center. In addition, we thank R.F. Adler for his support during the MIR development, and S.H. Melfi, and R.A. Ferrare for providing the lidar data. This work has been supported by NASA grant NAG 5-1490.

6.0 References

[1] A.J. Gasiewski, "Numerical sensitivity analysis of passive EHF and SMMW channels to tropospheric water vapor, clouds, and precipitation," *IEEE Transactions on Geoscience and Remote Sensing*, vol. 30, no. 5, pp. 859-870, Sept. 1992.

[2] W.P. Elliott and D.J. Gaffen, "On the utility of radiosonde humidity archives for climate studies," *Bulletin of the American Meteorological Society*, vol. 72, no. 10, pp. 1507-1520, Oct. 1991.

[3] L. Garand, C. Grassotti, J. Hallé, and G.L. Klein, "On differences in radiosonde humidity-reporting practices and their implications for numerical weather prediction and remote sensing," *Bulletin of the American Meteorological Society*, vol. 73, no. 9, pp. 1417-1423, Sept. 1992.

[4] E.R. Westwater, J.B. Snider, and M.J. Falls, "Ground-based radiometric observations of atmospheric emission and attenuation at 20.6, 31.65, and 90 GHz: A comparison of measurements and theory," *IEEE Transactions on Antennas and Propagation*, vol. 38, no. 10, pp. 1569-1580, October 1990.

[5] M.N. England, F.J. Schmidlin, and J.M. Johansson, "Atmospheric moisture measurements: A microwave radiometer – radiosonde comparison," *IEEE Transactions on Geoscience and Remote Sensing*, vol. 31, no. 2, pp. 389-398, March 1993.

[6] J.S. Foot, S.J. English, D.C. Jones, C. Prigent, A. Chedin, and C. Claud, "Airborne observations at 89 and 157 GHz of atmospheric and surface properties: The MARSS project," in *Proceedings of the Specialist Meeting on Microwave Radiometry and Remote Sensing Applications*, Boulder, CO, June 1992, pp. 433-437.

[7] S.J. English, C. Guillou, C. Prigent, and D.C. Jones, "Aircraft measurements of water vapour continuum absorption at millimetre wavelengths," submitted to *Quarterly Journal of the Royal Meteorological Society*, Dec. 1992.

[8] V.J. Falcone, M.K. Griffin, R.G. Isaacs, J.D. Pickle, J.F. Morrissey, A.J. Jackson, A. Bussey, R. Kakar, J. Wang, P. Racette, D.J. Boucher, B.H. Thomas, and A.M. Kishi, "SSM/T-2 calibration and validation data analysis," Phillips Laboratory, Hanscom AFB, MA, Environmental Research Papers No. 1111, PL-TR-92-2293, Oct. 29, 1992.

[9] J.F. Morrissey, J.D. Pickle, V.J. Falcone, and M.K. Griffin, "Effects of radiosonde type on satellite-derived humidities," in *Proceedings of the Topical Symposium on Combined Optical-Microwave Earth and Atmosphere Sensing*, Albuquerque, NM, March 22-25, 1993, pp. 199-202.

[10] J.R. Wang, S.H. Melfi, P. Racette, D.N. Whiteman, R.K. Kakar, R.A. Ferrare, K.D. Evans, and F.J. Schmidlin, "Simultaneous measurements of atmospheric water vapor with MIR, Raman lidar and rawinsondes," in *Proceedings of the International Geoscience and Remote Sensing Symposium IGARSS '93*, Tokyo, Japan, Aug. 18-21, 1993, vol. 3, pp. 1061-1063.

[11] H.J. Liebe, G.A. Hufford, and M.G. Cotton, "Propagation modeling of moist air and suspended water/ice at frequencies below 1000 GHz," in *Proceedings of the AGARD 52nd Specialists' Meeting of the Electromagnetic Wave Propagation Panel*, Palma De Mallorca, Spain, May 17-21, 1993, pp. 3-1 – 3-10.

[12] P.W. Rosenkranz, "Absorption of microwaves by atmospheric gases," in *Atmospheric Remote Sensing by Microwave Radiometry*, M.A. Janssen, Ed. New York: John Wiley and Sons, 1993, ch. 2.

[13] A.J. Gasiewski, "Microwave radiative transfer in hydrometeors," in *Atmospheric Remote Sensing by Microwave Radiometry*, M.A. Janssen, Ed. New York: John Wiley and Sons, 1993, ch. 3.

[14] F.T. Ulaby, R.K. Moore, and A.K. Fung, *Microwave Remote Sensing: Active and Passive*, Volume 1. Reading, MA: Addison-Wesley, 1981, ch. 4.

[15] M.A. Janssen, "An introduction to the passive microwave remote sensing of atmospheres," in *Atmospheric Remote Sensing by Microwave Radiometry*, M.A. Janssen, Ed. New York: John Wiley and Sons, 1993, ch. 1.

[16] G. Schaerer and T.T. Wilheit, "A passive microwave technique for profiling of atmospheric water vapor," *Radio Science*, vol. 14, no. 3, pp. 371-375, May-June 1979.

[17] A.J. Gasiewski and J.T. Johnson, "Statistical temperature profile retrievals in clear-air using passive 118-GHz O_2 observations," *IEEE Transactions on Geoscience and Remote Sensing*, vol. 31, no. 1, pp. 106-115, Jan. 1993.

[18] *U.S. Standard Atmosphere Supplements*, U.S. Government Printing Office, Washington, D.C., 1966

[19] R.R. Rogers and M.K. Yau, *A Short Course in Cloud Physics*, 3rd edition. Oxford, England: Pergamon Press, 1989, ch. 2.

[20] P.E. Racette, L.R. Dod, J.C. Shiue, R.F. Adler, D.M. Jackson, A.J. Gasiewski, and D.S. Zacharias, "Millimeter-wave imaging radiometer for cloud, precipitation, and atmospheric water vapor studies," in *Proceedings of the International Geoscience and Remote Sensing Symposium IGARSS '92*, Houston, TX, May 26-29, 1992, vol. 2, pp. 1426-1428.

[21] A.J. Gasiewski and D.M. Jackson, "Electromagnetic scattering from lossy periodic surfaces: Application to microwave absorbers," submitted to *IEEE Transactions on Antennas and Propagation*, March 1993.

[22] S.H. Melfi and D. Whiteman, "Observation of lower-atmospheric moisture structure and its evolution using a Raman lidar," *Bulletin of the American Meteorological Society*, vol. 66, no. 10, pp. 1288-1292, Oct. 1985.

[23] D.N. Whiteman, S.H. Melfi, and R.A. Ferrare, "Raman lidar system for the

measurement of water vapor and aerosols in the Earth's atmosphere," *Applied Optics*, vol. 31, no. 16, pp. 3068-3082, June 1, 1992.

[24] F.J. Brousaides, "The radiosonde hygristor and low relative humidity measurements," *Bulletin of the American Meteorological Society*, vol. 56, no. 2, pp. 229-233, Feb. 1975.

[25] C.G. Wade and D.E. Wolfe, "Performance of the VIZ carbon hygristor in a dry environment," in *Proceedings of the 12th Conference on Forecasting and Analysis*, Monterey, CA, American Meteorological Society, Oct. 1989, pp. 58-62.

[26] G. Klein and A. Hilton, "An intercomparison of the Viasala Humicap and the VIZ carbon hygristor under operational conditions," Technical Report No. TR-16, Atmospheric Environment Service, Ontario, Canada, May 1987.

[27] F.J. Brousaides and J.F. Morrissey, "Residual temperature-induced humidity errors in the National Weather Service radiosonde," Final Report, AD-780-643, Air Force Cambridge Research Laboratories, Mass., 1974.

[28] A.J. Gasiewski and D.H. Staelin, "Numerical modeling of passive microwave O_2 observations over precipitation," *Radio Science*, vol. 25, no. 3, pp. 217-235, May–June, 1990.

[29] H.J. Isemer and L. Hasse, *The Bunker Climate Atlas of the North Atlantic Ocean*, vol 2. Berlin, Germany: Springer-Verlag, 1987.

Table I
MIR Receiver Characteristics

LO Frequency (GHz)	IF (MHz)	DSB Receiver Temperature (K)	Nominal ΔT_{rms} (K)
89.0	500-1500	630	0.13
150.0	500-1500	860	0.16
183.31	500-1500	2000	0.34
183.31	2000-4000	2000	0.28
183.31	6000-8000	2000	0.28
220.0	1000-4000	2000	0.26

Table II

Summary of the observed nadiral MIR brightness temperatures used in the comparisons from Wallops and Ames flights

Location (background type)	Frequency (GHz)					
	89	150	183±1	183±3	183±7	220
Wallops (ocean)	(26 samples)					
Mean (K)	220.1	266.7	255.6	270.3	281.3	282.1
Std. Dev. (K)	10.41	12.34	5.66	5.13	4.72	5.03
Wallops (land)	(8 samples)					
Mean (K)	279.9	286.4	255.1	270.0	280.7	285.7
Std. Dev. (K)	3.19	2.51	6.56	5.42	3.88	2.61
Ames (ocean)	(8 samples)					
Mean (K)	207.3	252.4	260.1	275.3	282.2	277.0
Std. Dev. (K)	2.07	3.27	3.91	2.68	1.77	2.48

Table III
Summary of ER-2 Data Flights for Clear-Air Comparison Experiments (1992)

ER-2 Flight #	Date	Time (UTC)	Description
92-089	14-15 May	2315–0440	San Nicolas, Pt. Mugu
92-090	15-16 May	2320–0445	San Nicolas, Pt. Mugu
92-131	29 July	0700–1325	Flight track 1[a]
92-132	30 July	0707–1330	Flight track 1[a]
92-134	2 August	0630–0920	Flight track 2[b]
92-135	3 August	0300–0600	Flight track 2[b]
92-140	6 August	0700–1310	Flight track 1[a]

a. 2 passes over Wallops parallel to coast, 2 passes over Wallops perpendicular to coast, 1 round-trip to Cape Cod over ocean, 200 km off coastline.
b. 2 passes over Wallops parallel to coast, 2 passes over Wallops perpendicular to coast.

Table IV

Wallops Island aircraft-based comparisons over an ocean background of computed and observed brightness temperatures. Nadir values: computed – observed

Instrument Type	Frequency (GHz)					
	89	150	183±1	183±3	183±7	220
AIR Radiosonde	(18 comparisons)					
Mean (K)	3.42	1.43	–10.90	–6.47	–2.98	–0.432
Std. Dev. (K)	2.82	3.45	3.61	3.49	2.27	1.36
VIZ Radiosonde	(9 comparisons)					
Mean (K)	3.62	0.50	–6.33	–2.19	–0.41	–0.462
Std. Dev. (K)	2.84	1.02	1.59	1.57	0.94	0.61
Viasala Radiosonde	(12 comparisons)					
Mean (K)	–2.27	–2.49	–2.09	0.23	1.04	–0.033
Std. Dev. (K)	2.07	1.80	3.06	1.88	1.34	0.76
Lidar (w/AIR)	(125 comparisons)					
Mean (K)	–0.093	–0.41	–11.10	–4.60	–1.54	–0.282
Std. Dev. (K)	2.30	3.16	3.20	2.47	1.89	1.94
Lidar (w/Vaisala)	(69 comparisons)					
Mean (K)	–0.141	–0.93	–5.87	–2.51	–0.381	–0.503
Std. Dev. (K)	1.80	1.83	2.16	1.43	1.08	0.86

Table V

Wallops Island aircraft-based comparisons over a land background of computed and observed brightness temperatures. Nadir values: computed – observed

Instrument Type	Frequency (GHz)					
	89	150	183±1	183±3	183±7	220
AIR Radiosonde	(5 comparisons)					
Mean (K)	3.35	0.23	–10.40	–5.69	–2.34	–0.68
Std. Dev. (K)	0.89	0.54	3.51	2.75	1.51	1.04
Lidar (w/AIR)	(43 comparisons)					
Mean (K)	–0.76	0.61	–10.90	–4.09	–0.67	1.73
Std. Dev. (K)	19.24	4.77	4.45	3.10	1.30	1.79

Table VI

Ames aircraft-based comparisons over an ocean background of computed and observed brightness temperatures. Nadir values: computed – observed

Instrument Type	Frequency (GHz)					
	89	150	183±1	183±3	183±7	220
Vaisala Radiosonde	(16 comparisons)					
Mean (K)	2.05	0.38	–3.35	–2.71	–1.18	–1.64
Std. Dev. (K)	4.02	5.63	3.68	2.37	1.39	3.13

7.0 Figures

Figure 1: Gaseous absorption coefficient due to molecular absorption of oxygen and water-vapor, for (a) z=0 km, P=1000 mb, and ρ_v=17.0 kg/m^3, (b) 2 km, 800 mb, 6.60 kg/m^3, (c) 6 km, 450 mb, 0.66 kg/m^3, and (d) 12 km, 200 mb, 0.039 kg/m^3. Specific frequencies of interest to this study are indicated by arrows.

Figure 2: Airborne-based nadir-directed incremental relative humidity weighting functions for a 2-km scale-height exponential water-vapor profile over: (a) an ocean background, and (b) a land background.

Figure 3: Ground-based zenith-directed incremental relative humidity weighting functions for a 2-km scale-height exponential water-vapor profile.

Figure 4: MIR brightness temperature time-series for ER-2 flight 92-131 over the NASA Wallops Island facility: (a) 183.3±1, ±3, ±7 GHz channels, (b) 89, 150, and 220 GHz channels. The flight track is a west- and east-directed overflight of the island and Virginia coast at 0900-0917 UTC and 0928-0940 UTC, respectively.

Figure 5: MIR brightness temperature time-series for ER-2 flight 92-089: (a) 183.3±1, ±3, ±7 GHz channels, (b) 89, 150, 220 GHz channels. This flight track is an overflight of Los Angeles and San Nicolas Island for 0012-0030 UTC.

Figure 6: Typical radiosonde relative humidity profiles from an AIR, VIZ, and Vaisala triple-sounding and a Raman lidar profile. (Wallops Island Va., 29 July 1992, 0700 UTC.)

Figure 7: Wallops ground-based experiment performed from 2200 to 0210 UTC on 29-30 July: (a) Time series of the six zenith-directed MIR observations, (b) Brightness temperature comparisons between MIR and AIR-, Vaisala-, and lidar-based calculations.

Figure 8: Wallops ground-based experiment performed from 2200 to 0250 UTC on 30-31 July: (a) Time series of the six zenith-directed MIR observations, (b) Brightness temperature comparisons between MIR and AIR-, Vaisala-, and lidar-based calculations.

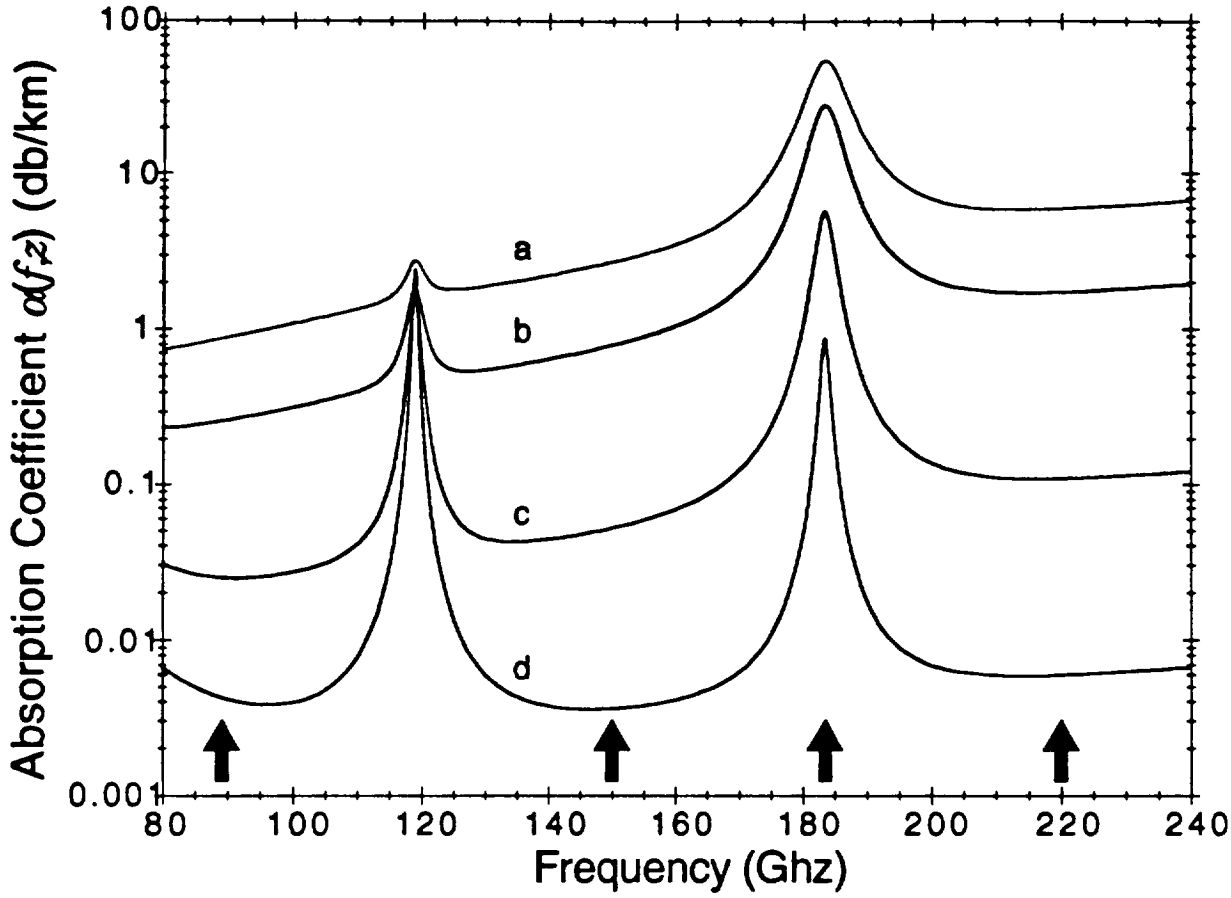
Absorption Coefficient α(fz) (db/km)
100
10
1
0.1
0.01
0.001
80
100
120
140
160
180
200
220
240
Frequency (Ghz)
a
b
c
d

Figure 1

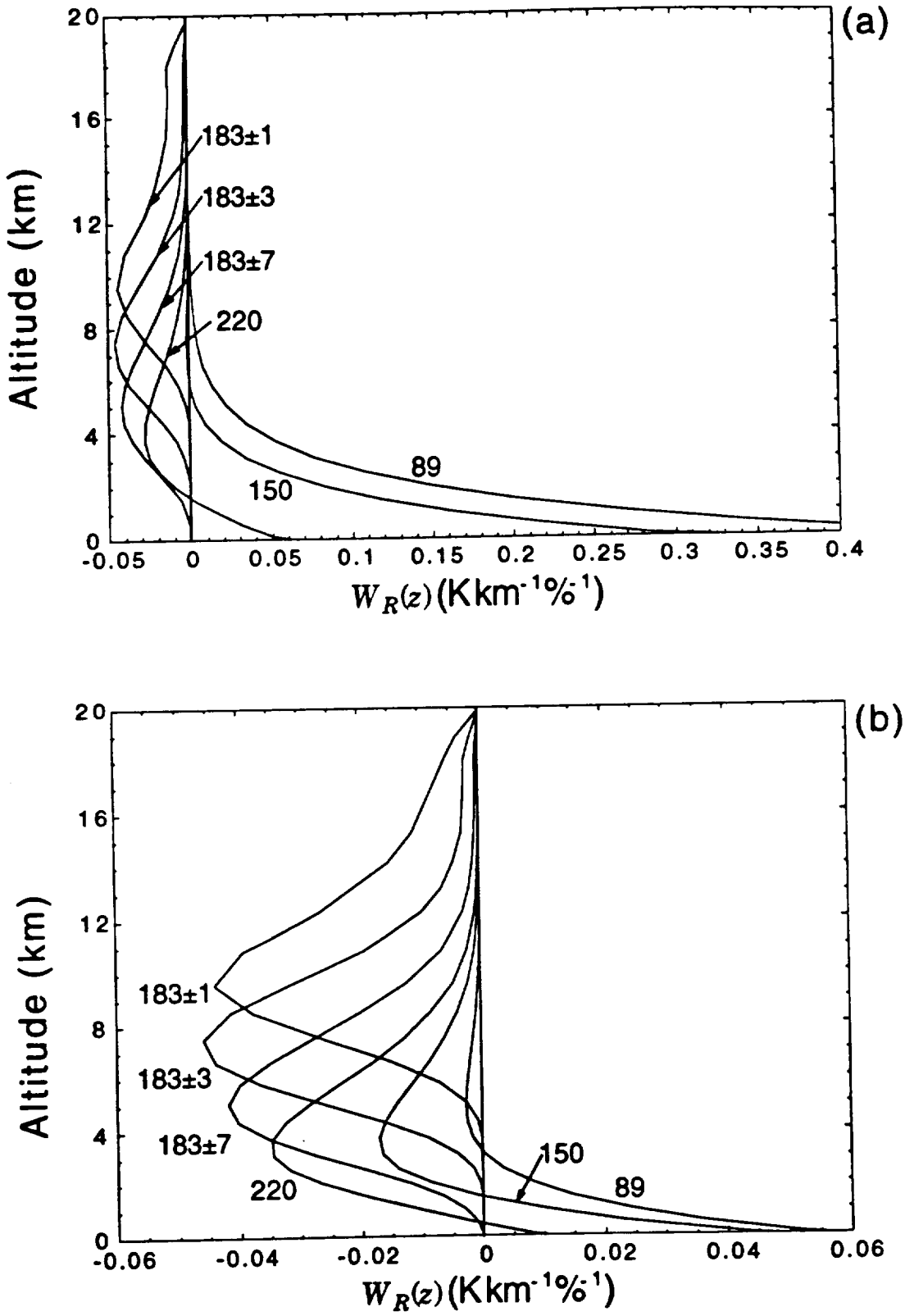
(a)
Altitude (km)
20
16
12
8
4
0
183±1
183±3
183±7
220
89
150
-0.05
0
0.05
0.1
0.15
0.2
0.25
0.3
0.35
0.4
$W_R(z)$(Kkm^{-1}%$^{-1}$)
(b)
Altitude (km)
20
16
12
8
4
0
183±1
183±3
183±7
220
150
89
-0.06
-0.04
-0.02
0
0.02
0.04
0.06
$W_R(z)$(Kkm^{-1}%$^{-1}$)

Figure 2

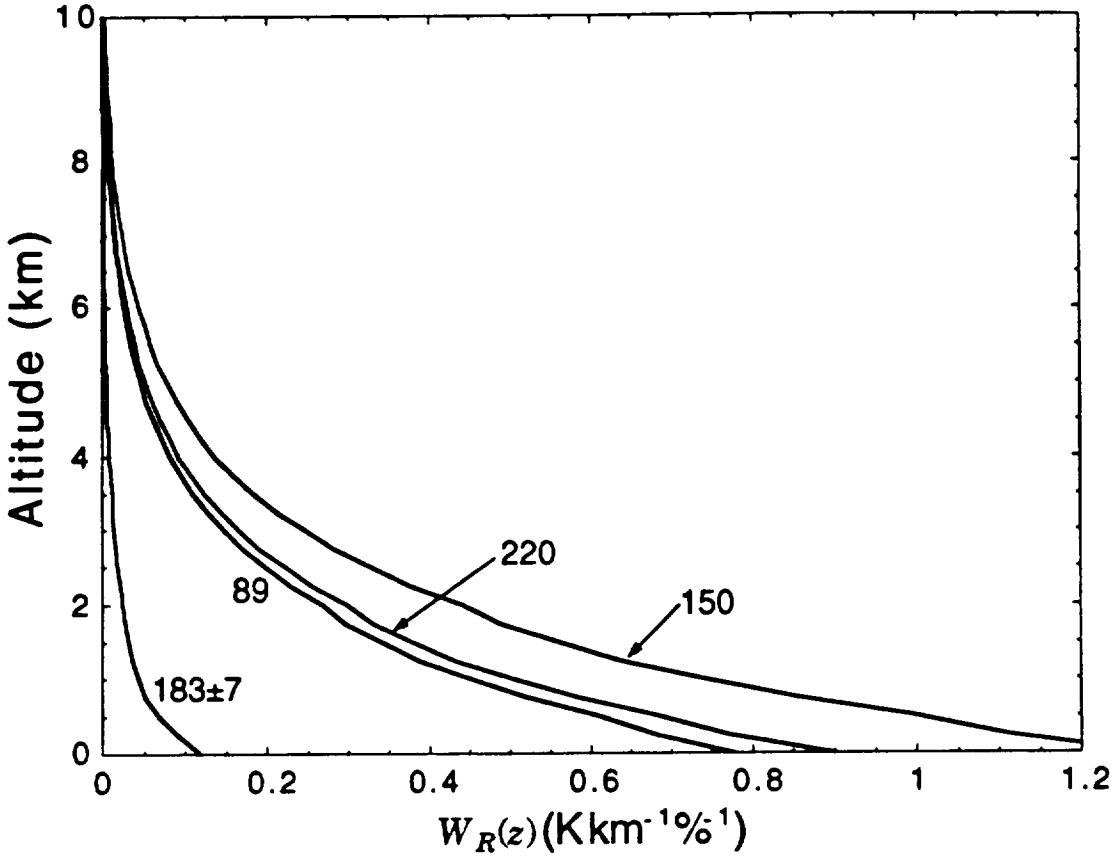

Figure 3

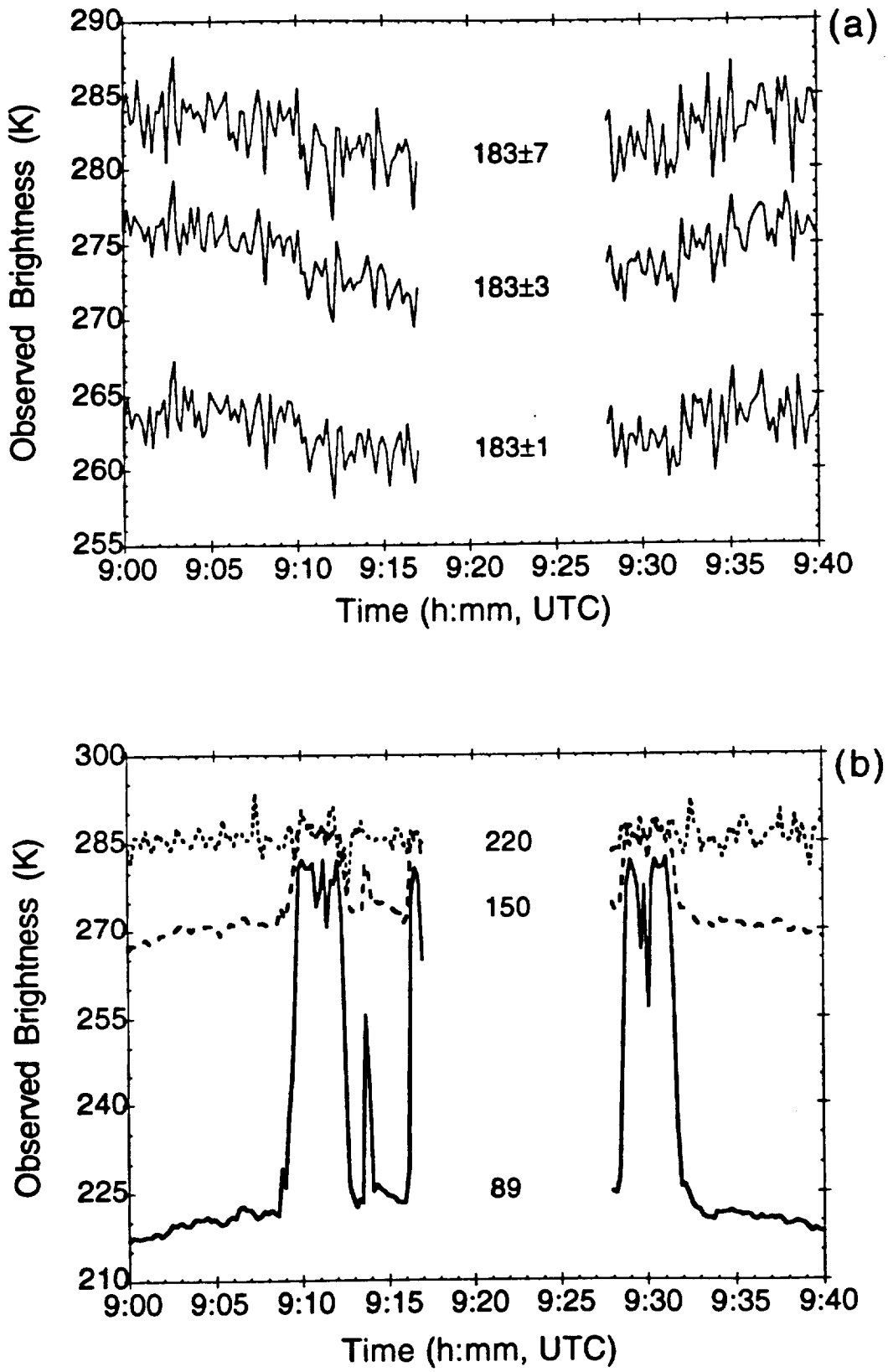
(a)
290
285
280
275
270
265
260
255
Observed Brightness (K)
183±7
183±3
183±1
9:00
9:05
9:10
9:15
9:20
9:25
9:30
9:35
9:40
Time (h:mm, UTC)
(b)
300
285
270
255
240
225
210
Observed Brightness (K)
220
150
89
9:00
9:05
9:10
9:15
9:20
9:25
9:30
9:35
9:40
Time (h:mm, UTC)

Figure 4

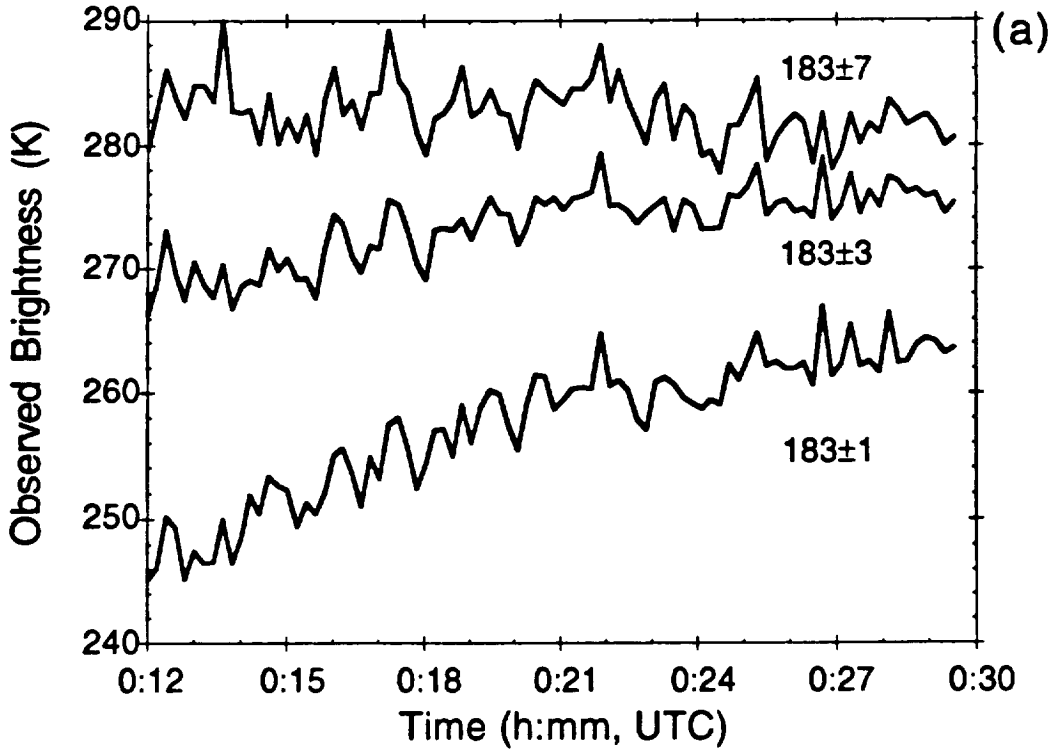
(a)
290
280
270
260
250
240
Observed Brightness (K)
183±7
183±3
183±1
0:12
0:15
0:18
0:21
0:24
0:27
0:30
Time (h:mm, UTC)

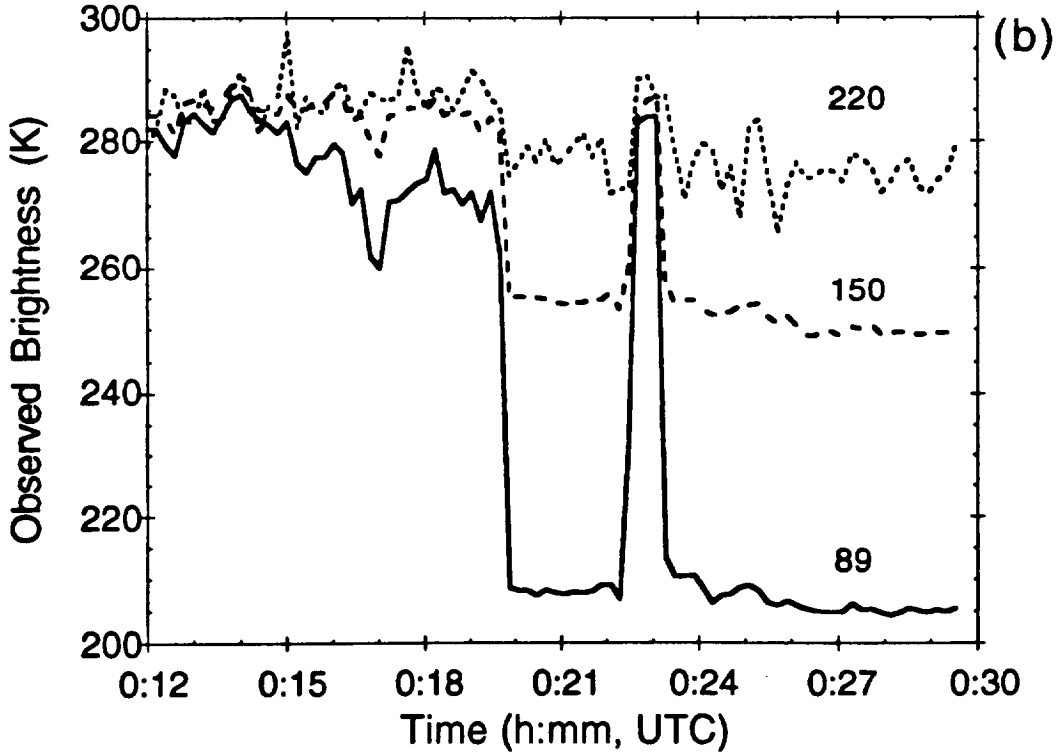
(b)
300
280
260
240
220
200
Observed Brightness (K)
220
150
89
0:12
0:15
0:18
0:21
0:24
0:27
0:30
Time (h:mm, UTC)

Figure 5

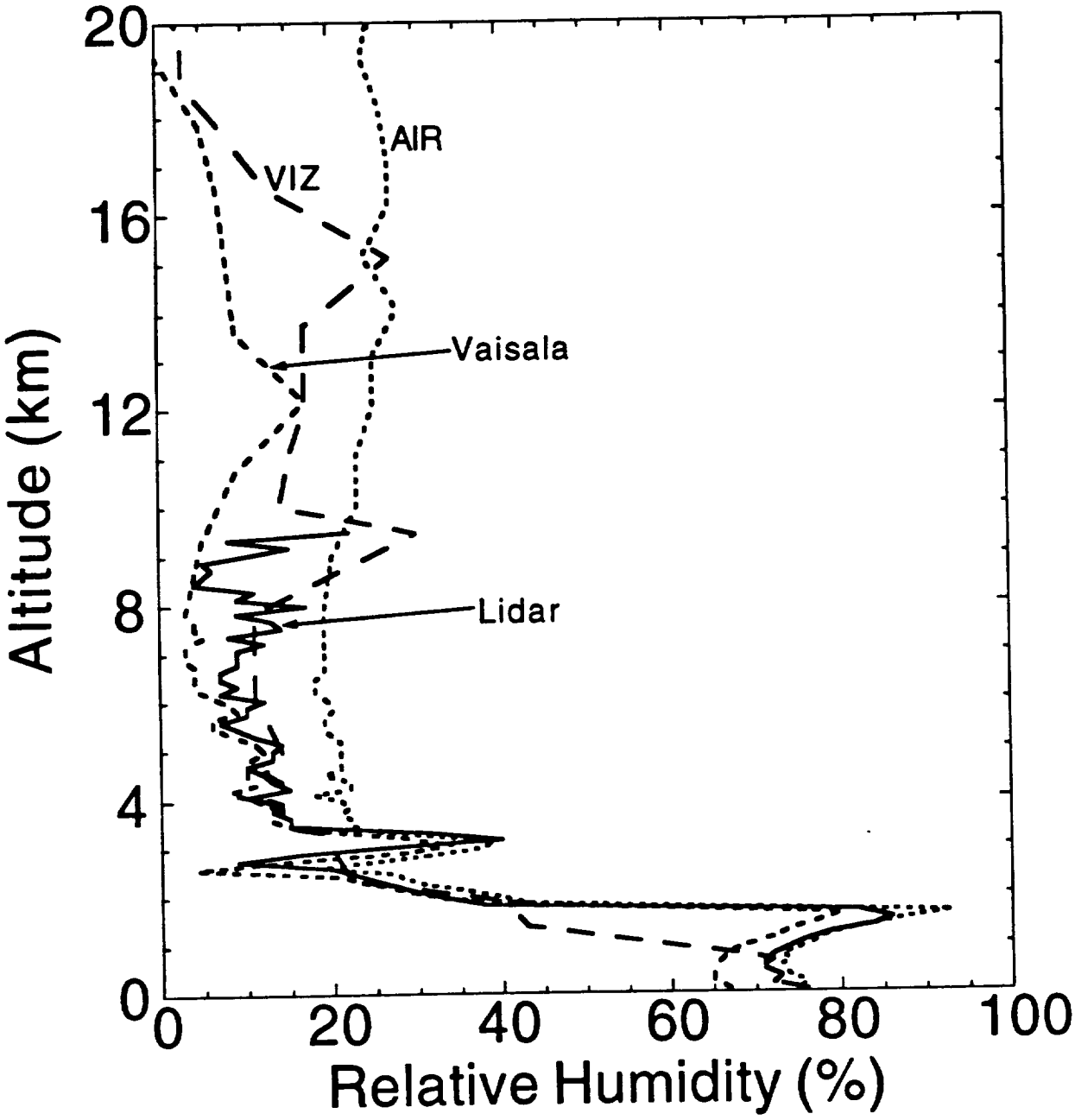
20
16
12
8
4
0
Altitude (km)
AIR
VIZ
Vaisala
Lidar
0
20
40
60
80
100
Relative Humidity (%)

Figure 6

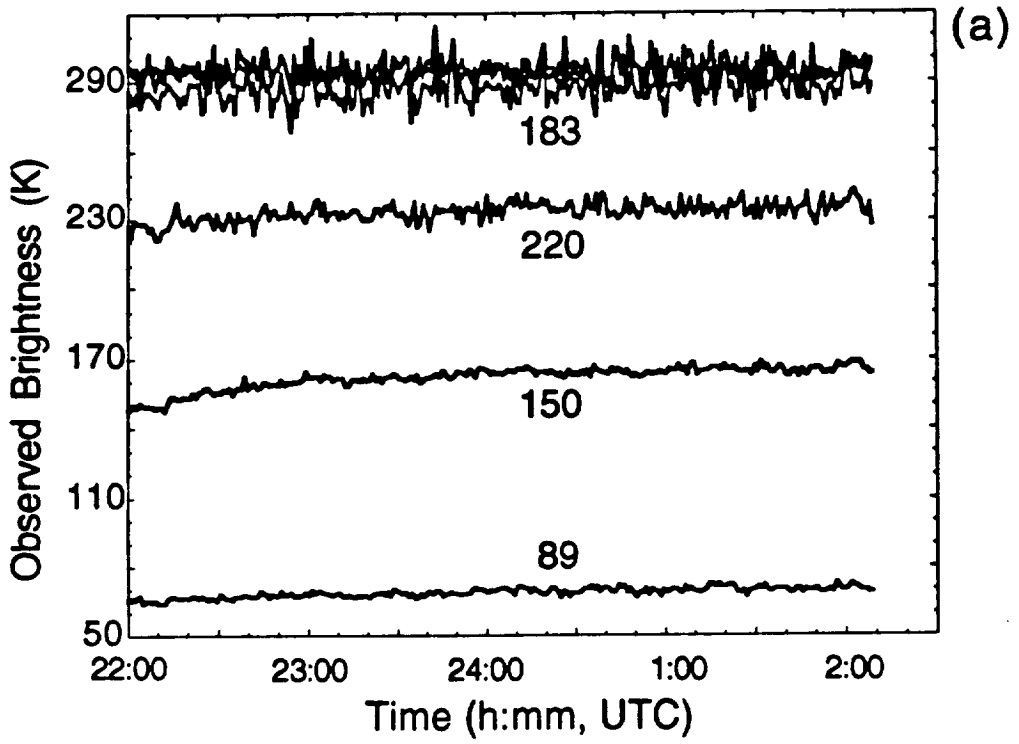
(a)
Observed Brightness (K)
290
230
170
110
50
183
220
150
89
22:00
23:00
24:00
1:00
2:00
Time (h:mm, UTC)

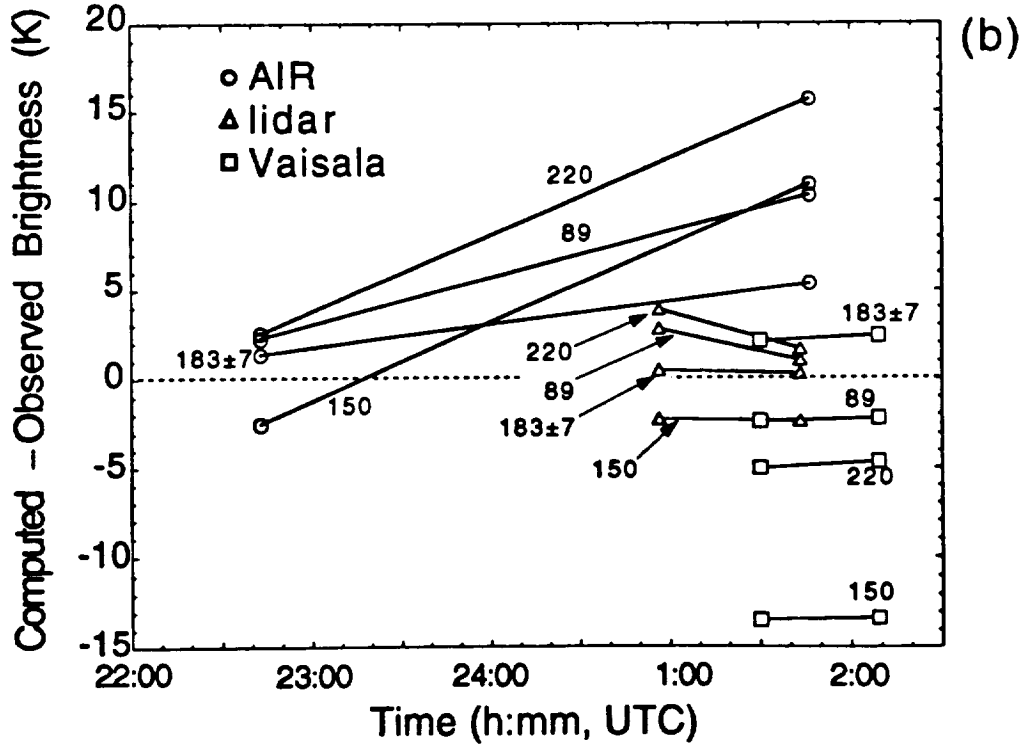
(b)
Computed - Observed Brightness (K)
20
15
10
5
0
-5
-10
-15
AIR
lidar
Vaisala
220
89
183±7
150
22:00
23:00
24:00
1:00
2:00
Time (h:mm, UTC)

Figure 7

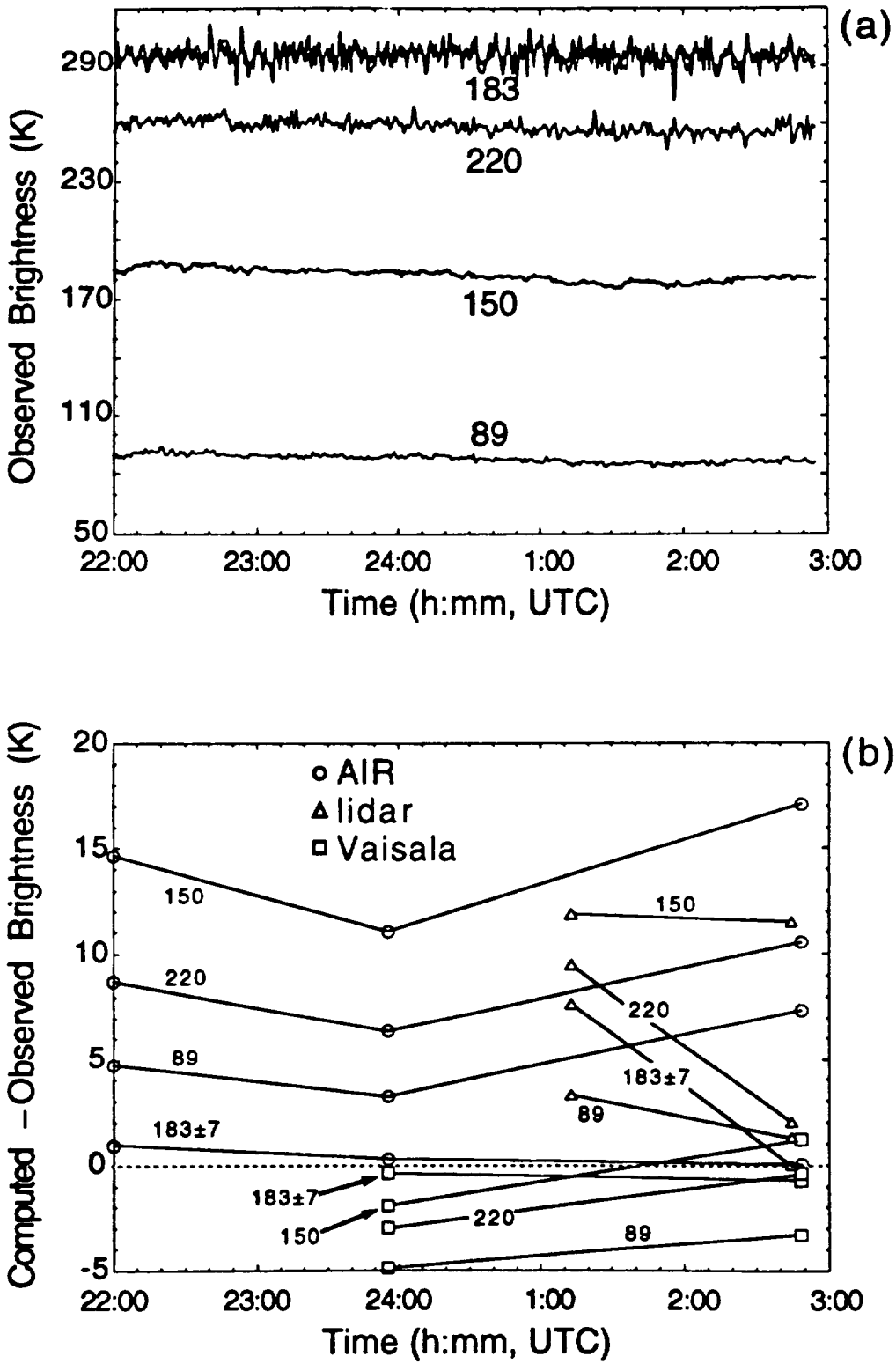
(a)
Observed Brightness (K)
290
230
170
110
50
183
220
150
89
22:00
23:00
24:00
1:00
2:00
3:00
Time (h:mm, UTC)
(b)
Computed − Observed Brightness (K)
20
15
10
5
0
-5
AIR
lidar
Vaisala
150
220
89
183±7
Time (h:mm, UTC)

Figure 8

OPTIMAL CALIBRATION OF RADIOMETERS USING WIENER FILTERING

L.K. Adelberg , A.J. Gasiewski, D.M. Jackson
School of Electrical Engineering
Georgia Institute of Technology, Atlanta, GA 30332-0250

Abstract

The application of Wiener filters to the problem of radiometer calibration is investigated. The calibration process uses voltage measurements of two targets of known temperature and emissivity, to derive a gain and offset for each scan of the instrument. The actual measurements, however, contain integration noise which limits the accuracy of the calibration. This research focuses upon the application of statistical Wiener filtering theory to develop optimal (minimum mean squared error) linear estimates for the gain and offset. The filters are tested for data from the Millimeter-Wave Imaging Radiometer. A significant reduction in calibration noise relative to that of a conventional infinite impulse response filter is demonstrated. Since the filter was derived for the conditions of statistical stationarity, a method for detecting jumps in the gains and offsets was developed.

1. Introduction

In microwave radiometry, measurements of hot and cold blackbody targets of known temperature and emissivity typically are used for calibration. The technique involves estimation of two slowly time varying processes (the gain m and the offset b) from noisy observations of these targets. Typically, these targets are observed once per scan producing voltage output $v = mT_A + b + n$ where n represents additive white Gaussian noise and T_A is the antenna temperature. Using observations of the hot and cold targets (v_{Hi} and v_{Ci}) coupled with the known antenna temperature, the single scan estimates for the calibration quantities are:

$$\widetilde{m_i} = \frac{v_{Hi} - v_{Ci}}{T_{Hi} - T_{Ci}} \qquad \widetilde{b_i} = \frac{v_{Ci}T_{Hi} - v_{Hi}T_{Ci}}{T_{Hi} - T_{Ci}}. \quad (1)$$

However, because of the presence of the noise n, these estimates are necessarily inaccurate.

Typically, this error is reduced by applying a single pole infinite impulse response (IIR) filter. This filter, however, is slow to adjust to shifts in the gain and offset statistics experienced during normal operation of the radiometer. A better filter would make use of the statistics of the gain and offset shifts to optimally reduce the noise component of the signal by incorporating many single scan observations into the development of the desired single spot quantity.

We begin by defining:

$$\widehat{m}_i = \sum_k w_k^m \, \tilde{m}_{i-k} \qquad \widehat{b}_i = \sum_k w_k^b \, \tilde{b}_{i-k} \quad (2)$$

where the w_k^m and w_k^b are the filter weights for the respective process m and b. When these weights are chosen to minimize the mean squared error of the the estimate, this is the discrete Wiener filter. This paper explores the application of Wiener filtering to the problem of radiometer calibration.

2. Discrete Wiener Filter Theory

The Wiener filter coefficients can be obtained by minimizing the mean squared error between the filtered estimates and the actual desired quantities. Letting x_i denote the desired variables (i.e. true gain or offset) and u_i denote its single scan estimate the error is defined as:

$$\begin{aligned} e_i &= x_i - \widehat{x}_i \\ &= (x_i - \sum_{k=-N}^{N} w_k u_{i-k}) \end{aligned} \quad (3)$$

where a $2N + 1$-point function is used. Since processing is performed off-line, the filter can be non-causal. A non-causal filter is used in recognition of the fact that future statistical trends are relevant to the calculation of the current quantities. If a causal filter were used, all information about the future signal would be lost and the error of the system would increase.

The mean squared error is defined as:

$$\begin{aligned} \sigma_e^2 &= E[(x_i - \widehat{x}_i)^2] \\ &= E[(x_i - \sum_{k=-N}^{N} w_k u_{i-k})^2] \end{aligned} \quad (4)$$

Using the autocorrelation function estimates m and b, the filter $\overline{w}$ was computed:

$$\overline{w} = (\overline{\overline{R}}_{xx} + \overline{\overline{R}}_{nn})^{-1}\overline{R}_{xu}. \quad (11)$$

To insure unbiased estimates of m and b, unitarity (i.e. $\sum w = 1$) was enforced by scaling the filter coefficients.

5. Application to Airborne Radiometry

The physical interpretation of the impulse at t = 0 in $\overline{\overline{R}}_{uu}$ is the variance of the high frequency fluctuation of the gain and offset processes due to integration noise. In the absense of gain and offset fluctuation noise, the minimum standard deviation of a constant temperature scene is [2, pp. 358 - 368]:

$$\Delta T_{RMS} = T_{sys}\sqrt{\frac{1}{B\tau}} \quad (12)$$

where B is the bandwidth of the the channel, τ is the integration time for the instrument, and T_{sys} is the system temperature. This equation defines the relative sensitivity of the instrument. As gain and offset noise increases, additional terms must be included to account for the fluctuations increasing the minimum sensitivity to

$$\Delta T_{RMS} = T_{sys}\sqrt{\frac{1}{B\tau} + (\frac{\sigma_m}{\langle m\rangle})^2 + (\frac{\sigma_b}{\langle m\rangle T_{sys}})^2} \quad (13)$$

degrading the performance of the radiometer.

The improvement of the ΔT_{RMS} using the Wiener filtering technique was demostrated by processing clear-air radiometric data over ocean for which the scene brightness temperatures are nearly constant. Prior to applying the filter to data, the estimated parameters from the autocorrelation functions were used for theoretical comparisons to test the accuracy of this model. From Eq. 1, the single-scan gain fluctuations are:

$$\begin{aligned}\widetilde{m_i} &= \frac{v_{Hi} - v_{Ci}}{T_{Hi} - T_{Ci}} \\ &= \frac{(v_{HA} + n_H) - (v_{CA} - n_C)}{T_{Hi} - T_{Ci}} \\ &= \frac{v_{HA} - v_{CA}}{T_{Hi} - T_{Ci}} + \frac{n_H - n_C}{T_{Hi} - T_{Ci}} \\ &= m_{Ai} + \frac{n_H - n_C}{T_{Hi} - T_{Ci}} \quad (14)\end{aligned}$$

where m_{Ai} is the true quantity (i.e. no noise). Substituting into Eq. 4, σ_m^2 can be predicted by:

$$\begin{aligned}\sigma_{nn}^2 &= E[(m_A - (m_A + \frac{n_H - n_C}{T_{Hi} - T_{Ci}}))^2] \\ &= \frac{2(\langle m\rangle \Delta T_{RMS})^2}{(T_{Hi} - T_{Ci})^2} \quad (15)\end{aligned}$$

This allows comparison of the measured height of the impulse function to a theoretical calculation.

For these comparisons, we use a modified version of Eq. 12 which accounts for the RC integration and oversampling technique [7] used in the MIR:

$$\Delta T_{RMS} = T_{sys}\sqrt{\frac{1}{B\tau}}P(N_L, \rho) \quad (16)$$

$$P(N_L, \rho) = \sqrt{\frac{N_L(1-\rho^2) - 2\rho(1-\rho^{N_L})}{N_L(1-\rho)^2}} \quad (17)$$

where $\tau = N_L\Delta t$, $P(N_L, \rho)$ is a derating factor with N_L total samples during calibration stares, and $\rho = exp(-\frac{\Delta t}{RC})$ is the correlation between subsequent calibration measurements. The actual sampling interval is Δt. As Δt decreases relative to the RC time constant, consecutive voltage measurements contain information from prior samples still held by the integration filter. Since the previous signals have not yet decayed, new measurements contain less additional information than the completely uncorrelated case (e.g. $\Delta t \gg RC$). The P-factor, therefore, corrects the ΔT_{RMS} in Eq. 12 due to this correlation. For the MIR, P = 1.48 with $N_L = 27$, RC = 6.8 ms and a sampling interval of approximately 6.1 ms.

For the following noise calculations (Table 1), $T_{Hi} - T_{Ci} = 100$ K. By definition, $\tau = N_s T_s$ [2] where N_s is the number of samples taken at a specific location (spot) in the rotation of the mirror ($N_s = 13$) and T_s is the sampling interval (6.1ms) yielding a value $\tau \approx 80$ms. It is noted that the three window channels (89, 150, 220 GHz) all have good agreement with the theoretical calculation and the estimate obtained from the autocorrelation function. The three 183 GHz channels, however, have greater values for the estimated noise than the theoretical prediction (5 times greater). This does not imply failure of this method, but rather implies the presence of a noise source greater than the theoretical limit (i.e. Eq. 13 rather than Eq. 12). Calculations from other flights demonstrate similar numerical results (i.e. good agreement for window channels and similar difference factors for the 183 GHz channels).

The Wiener calibration filter is applied to the gain and offset sequences and the brightness temperatures are subsequently computed. The Wiener-filtered data is then compared with the IIR-filtered data for evaluation purposes using data collected over clear air regions of flight. Clear air regions were located using coincident measurements with the lidar. Since the lidar measurements verify clear air at nadir positions, the MIR comparisons have been limited to these spots to eliminate the possibility of atmospheric structure creating increases in the variance of the scene temperature. However, full scan calculations have been performed with results that are consistent with the nadir spots in areas believed to contain clear air.

The standard deviation of the clear air measurements is calculated using the along track nadir spots for both the IIR and Wiener filtered case. In order to obtain statistically significant comparisons, only regions with a

Table 1: Comparison of Estimated and Calculated Noise Variance

Channel	ΔT_{RMS}	σ^2_{nn}	$\hat{\sigma}^2_{nn}$
89	0.199	2.24e-7	2.5e-7
150	0.245	3.35e-7	4e-7
183 ± 1	0.420	1.58e-6	8.15e-6
183 ± 3	0.297	8.15e-7	4.25e-6
183 ± 7	0.297	8.31e-7	4.5e-6
220	0.323	2.4e-6	3.4e-6

Table 2: IIR versus Wiener Filter ΔT_{RMS} Comparisons Scene 1

Channel	ΔT_{RMS} IIR	ΔT_{RMS} Wiener
89	1.1195	1.0738
150	0.4221	0.3544
183 ± 1	1.7091	1.3039
183 ± 3	1.1591	0.9134
183 ± 7	1.6537	0.9108
220	0.8920	0.5239

Table 3: IIR versus Wiener Filter ΔT_{RMS} Comparisons Scene 2

Channel	ΔT_{RMS} IIR	ΔT_{RMS} Wiener
89	0.9973	0.9837
150	0.4307	0.3187
183 ± 1	2.2003	1.2264
183 ± 3	1.5338	0.7959
183 ± 7	1.1878	0.8391
220	0.9499	0.5446

Table 4: Jump Detector Performance

Jumps Locations	Jump Height	Jump Detection
700	0.7078	
1200	-0.7078	
1500	-1.4138	x
2000	1.4138	x
2100	1.4734	x
2600	-1.4734	x
2700	0.4262	
3200	-0.4262	
3300	1.2315	x
3800	-1.2315	x

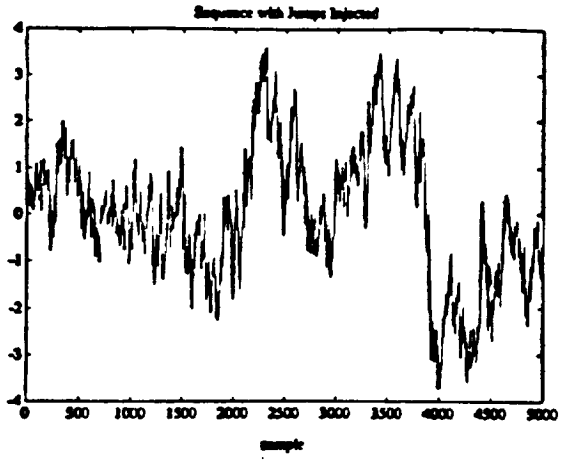

Figure 5: Simulated sequence for testing jump detector.

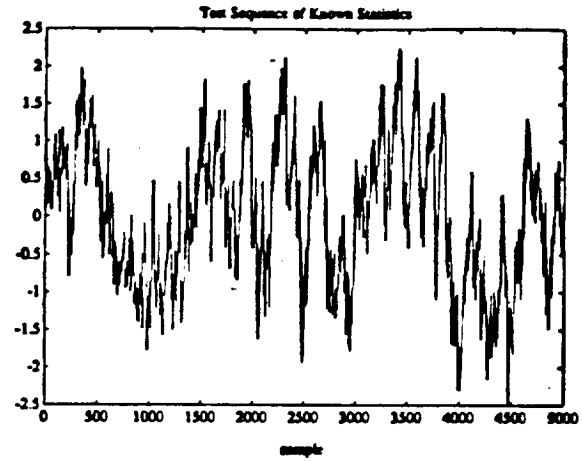

Figure 6: Simulated sequence with jumps located as depicted in Table 1.

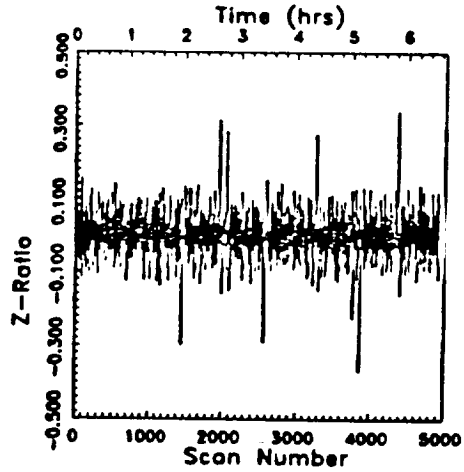

Figure 7: Z-ratio test results. Notice the impulse functions at the jump locations.

References

[1] S. Haykin, *Adaptive Filter Theory*. Englewood Cliffs, NJ: Prentice Hall, 1991.

[2] Ulaby, Fung, and Moore, *Microwave Remote Sensing, Active and Passive*. 1986.

[3] S. A. Book, *Statistics: Basic Techniques for Solving Problems*. New York: McGraw-Hill, Inc., 1977.

[4] H. D. Tagare and R. J. deFiueiredo, "On the localization performance measure and optimal edge detection," *SPIE*, vol. 1244, pp. 408 – 412, 1990.

[5] A. J. Gasiewski, "Airborne passive microwave remote sensing during TOGA/COARE," *URSI Radio Science Meeting*, URSI '93, Ann Arbor, MI, p. 45, June 28 - July 3 1993.

[6] P. Racette et al, "Millimeter-Wave imaging radiometer for cloud, precipitation and atmospheric water vapor studies," *International Geoscience and Remote Sensing Symposium*, IGARSS '92, Houston, TX, Vol. 2, pp. 1426 – 1428, May 26 – 29, 1992.

[7] A. J. Gasiewski and D. H. Staelin, Coursenotes, Remote Sensing Signals and Systems, Georgia Institute of Technology, Feb. 1993.

[8] J. Durbin, "The fitting of time series models," *Review of the International Statistical Institute*, Vol. 23, pp 233 – 244, 1960.

Polarized Microwave Emission from Water Waves

A.J. Gasiewski and D.B. Kunkee

School of Electrical and Computer Engineering
Georgia Institute of Technology
Atlanta, Georgia 30332-0250

Submitted for publication in:
Radio Science

December 1, 1993

Abstract

Partially polarimetric measurements of thermal emission from a striated water surface at 91.65 GHz illustrate the potential for remote sensing of water wave direction by passive microwave radiometry. The three Stokes parameter measurements were made using a precision polarimetric radiometer trained on a rotatable water wave tank at several elevation angles from near nadir to near grazing. The polarimetric measurements are well corroborated by calculations using a tilted-facet geometrical optics model for the water surface emission and scattering. Multiple scattering of the incident background radiation is incorporated for observation angles approaching grazing. The downwelling background brightness is computed using an atmospheric radiative transfer model. We show that azimuthal brightness variations in the third Stokes parameter are in phase quadrature with the first and second modified Stokes parameters. For observation angles near $\sim 60 - 70^{\circ}$ from nadir the first three parameters have particularly large azimuthal brightness variations, and thus have significant potential for measuring ocean wave direction. Moreover, the azimuthal brightness variations caused by water waves are not negligible for many passive microwave atmospheric sounding and surface remote sensing purposes, even at nadir. A range of elevation angles resulting in minimal azimuthal variations is identified.

1. Introduction

The utility of vertically and horizontally polarized brightness temperatures in passive microwave remote sensing of terrestrial atmospheric and surface properties is recognized by many investigators. Studies of dual-polarized thermal radiation have benefited from satellite data using instruments such as the Scanning Multichannel Microwave Radiometer (SMMR) [*Njoku et al.*, 1980] and the Special Sensor Microwave/Imager (SSM/I) on the DMSP Block-5 platforms [*Hollinger et al.*, 1990]. Here, the large contrast between T_v and T_h (the first two modified Stokes' parameters, as defined in the Earth's "natural" polarization basis) has been used to improve measurements of ocean surface wind speed, atmospheric clouds, rain and water vapor, and facilitate sea ice detection. Recent theoretical and experimental investigations have also shown measurable differences between T_v and T_h caused by oriented atmospheric ice particles [*Evans and Vivekanandan*, 1990; *Adler et al.*, 1990].

Many techniques for the measurement and interpretation of the first two parameters have been published [e.g., *Stogryn*, 1967; *Spencer*, 1986]. However, comparatively few experimental studies of the utility of the third and fourth Stokes parameters (T_U and T_V) for Earth remote sensing have been made. Primary among these are airborne linearly-polarized brightness measurements over open wave-covered water by *Dzura et al.* [1992]. These measurements showed signatures in T_v, T_h, and (indirectly) T_U that were related to the wind vector. In other experiments, values of T_U as high as $\sim$ 50 K have been measured over rough periodic moist soil at a frequency of 10 GHz [*Veysoglu*, 1991; *Veysoglu et al.*, 1991; *Nghiem et al.*, 1991]. The measurements were corroborated by an electromagnetic diffraction model based on the method of moments. Currently, there is increasing interest in passive microwave remote sensing of land and ocean parameters using fully-polarimetric measurements.

In this paper, we present the results of experiments investigating the relationship between the first three Stokes' parameters of the upwelling radiation field over a striated water surface and the associated water wave parameters. Direct measurements of T_v, T_h and T_U were made over a rotatable outdoor water wave tank using a well-calibrated 91.65-GHz polarization correlating radiometer developed by the authors [*Gasiewski*, 1990; *Gasiewski and Kunkee*, 1992, 1993]. A polarized calibration load was used to achieve an absolute calibration accuracy of approximately

2 K for each Stokes parameter. Standing gravity waves were generated in the tank; by rotating the tank the water wave vectors could be oriented at arbitrary azimuthal angles with respect to the radiometer's plane of observation.

The polarimetric measurements were corroborated by a geometrical optics (GO) model of the water surface scattering and emission. The GO model considers the water surface to be composed of specularly-reflecting facets, with the upwelling radiation field computed as a sum of contributions from each facet [e.g., *Ilyin and Raizer*, 1992]. The model accounts for multiple scattering along ray paths, and yields values of the full Stokes vector at observation angles from normal to near grazing. Estimates of the downwelling background radiation field are obtained from radiosonde data and using the numerical radiative transfer model of *Gasiewski and Staelin* [1990].

Computed GO and measured results are presented to illustrate the relationship between the first three upwelling Stokes' parameters and the water wave direction. The peak-to-peak amplitude and phase variations of T_v, T_h and T_U with azimuthal angle are shown to depend upon the water wave slope distribution, scan elevation angle and the atmospheric state. A numerical analysis illustrating the sensitivity of the upwelling radiation to various atmospheric and surface parameters is presented. Finally, implications of the investigation with regard to passive microwave remote sensing of ocean wave direction and passive atmospheric sounding are discussed.

2. Experiment Description

The polarization-correlating radiometer was implemented by modifying a 91.65-GHz dual-linearly polarized radiometer (Fig. 1). The v_A and v_B channels are the analog outputs of a conventional dual-polarized Dicke radiometer. The v_C channel is a simple adding correlator with a post-detection summing circuit to cancel the relatively large orthogonal-mode signals [*Gasiewski and Kunkee*, 1993]. The analog signals correspond to each of three radiometric parameters: the two orthogonal feedhorn mode powers $v_A \propto T_v$ and $v_B \propto T_h$, and a third parameter $v_C \propto \cos^2(\Delta\varphi)T_U + \sin^2(\Delta\varphi)T_V$. Here, $\Delta\varphi$ is a variable phase shift added to one of the two local oscillator signals. The v_C channel is a linear combination of the in-phase and quadrature correlations between the orthogonal-mode field amplitudes. By adjusting $\Delta\varphi$, the third channel

can be made sensitive to either T_U or T_V. The total electrical path lengths of the two orthogonal mode channels were equalized to well within one correlation length $l_c = v_p/W \sim 5$ cm by adjustment of Δl, where $v_p \sim 10^8$ m/sec is the IF phase velocity and $W = 2$ GHz is the IF bandwidth.

The water wave observations were made over a square rotatable wave tank measuring 1.2 m on a side and filled to a mean depth of $\sim$ 7 cm (Fig. 2). The tank size was large enough to subtend the radiometer beam to approximately the third pattern null, thus minimizing beam spillover. A 1.2-m long vertically-oscillating plunger coupled by eccentrics to a variable speed motor excited standing water waves with peak amplitudes from 0.3 to 0.5 cm. The dispersion relation for small-amplitude water waves is [*Phillips*, 1980]

$$\omega^2 = gk\left[1 + \frac{\tau k^2}{\rho g}\right]\tanh(kd) \tag{1}$$

where ρ is the water density, τ is the surface tension, d is the water depth, ω is the angular frequency and k is the surface wavenumber. Accordingly, the plunger was driven between 1.4 - 1.9 Hz to provide wavelengths adjustable from $\sim$ 7 to 12 cm. The wave profiles were approximately sinusoidal, and the 3-dB footprint of the radiometer subtended several water wavelengths.

All experiments were performed outdoors under clear-sky background conditions. The radiometer's antenna beam was trained on the wave-covered surface using flat subreflectors. Care was taken to insure that a cold sky background illuminated the water surface from all specular facet angles. Due to some minor feedhorn alignment problems the polarization basis of the instrument was skewed 15° relative to the $\hat{v} - \hat{h}$ basis of the water surface. This alignment error was removed during data processing using a Stokes' parameter rotation as described in *Gasiewski and Kunkee* [1993].

To minimize measurement errors caused by slightly imperfect sinusoidal water waves (e.g., waves exhibiting small travelling-wave components, reflected secondary wave components and small amplitude inhomogeneities) at least one full rotation of the tank was performed. Coincident radiosonde measurements of atmospheric temperature and water vapor profiles were obtained for computing sky background brightness temperatures. All radiosondes were launched from Athens, GA, located

100 km E-NE of the experiment location.

3. Geometrical Optics Model

Within the GO model, a non-flat surface is modelled by a distribution of specularly-reflecting facets, each of which contributes to the overall upwelling radiation in accordance with the Fresnel reflectivity relations [*Tsang, et al.*, 1985]. The surface material is assumed to be homogeneous and isotropic with dielectric parameters ϵ_2, μ_2, and illuminated by a clear-air background radiation field from a medium with parameters $\epsilon_1 = \epsilon_o, \mu_1 = \mu_o$.

Consider plane wave reflections into the observation direction $\hat{k}_s$ from the k^{th} facet (Fig. 3). The incident wave direction is:

$$\hat{k}_{i_k} = (\overline{\overline{I}} - 2\hat{n}_k\hat{n}_k)\,\overline{k}_s \tag{2}$$

where the $\hat{n}_k$ is the facet normal vector and $\overline{\overline{I}}$ is the identity matrix. Let the illuminating wave from this direction be

$$\overline{E}_{i_k} = (E_{v_{i_k}}\hat{v}_{i_k} + E_{h_{i_k}}\hat{h}_{i_k})\,e^{-j\overline{k}_{i_k}\cdot\overline{r}} \tag{3}$$

where the incident vertical and horizontal basis vectors $\hat{v}_{i_k}$ and $\hat{h}_{i_k}$ are defined according to:

$$\hat{v}_{i_k} = \hat{h}_{i_k} \times \hat{k}_{i_k} \qquad \hat{h}_{i_k} = \frac{\hat{k}_{i_k} \times \hat{z}}{|\hat{k}_{i_k} \times \hat{z}|} \tag{4}$$

The contribution to the scattered field from this facet is:

$$\overline{E}_{s_k} = (E_{v_{sk}}\hat{v}_s + E_{h_{sk}}\hat{h}_s)\,e^{-j\overline{k}_s\cdot\overline{r}} \tag{5}$$

where the scattered field components are related to the illuminating wave components by the scattering function matrix:

$$\begin{bmatrix} E_{v_{sk}} \\ E_{h_{sk}} \end{bmatrix} = e^{-j\overline{k}_s\cdot\overline{r}}\,\overline{\overline{f}}_k \begin{bmatrix} E_{v_{ik}} \\ E_{h_{ik}} \end{bmatrix} \tag{6}$$

and

$$\hat{v}_s = \hat{h}_s \times \hat{k}_s \qquad \hat{h}_s = \frac{\hat{k}_s \times \hat{z}}{|\hat{k}_s \times \hat{z}|} \tag{7}$$

The scattering function matrix elements are computed using the Fresnel reflectivity relations for the TE and TM wave components in the frame of the facet:

$$\overline{\overline{f}}_k = \begin{bmatrix} f_{vv_k} & f_{vh_k} \\ f_{hv_k} & f_{hh_k} \end{bmatrix} \tag{8}$$

where

$$f_{vv_k} = (\hat{v}_{i_k} \cdot \hat{p}_{i_k}) R_v(\theta_{l_k}) (\hat{v}_s \cdot \hat{p}_{s_k}) + (\hat{v}_{i_k} \cdot \hat{q}_k) R_h(\theta_{l_k}) (\hat{v}_s \cdot \hat{q}_k) \quad (9)$$

$$f_{vh_k} = (\hat{h}_{i_k} \cdot \hat{p}_{i_k}) R_v(\theta_{l_k}) (\hat{v}_s \cdot \hat{p}_{s_k}) + (\hat{h}_{i_k} \cdot \hat{q}_k) R_h(\theta_{l_k}) (\hat{v}_s \cdot \hat{q}_k) \quad (10)$$

$$f_{hv_k} = (\hat{v}_{i_k} \cdot \hat{p}_{i_k}) R_v(\theta_{l_k}) (\hat{h}_s \cdot \hat{p}_{s_k}) + (\hat{v}_{i_k} \cdot \hat{q}_k) R_h(\theta_{l_k}) (\hat{h}_s \cdot \hat{q}_k) \quad (11)$$

$$f_{hh_k} = (\hat{h}_{i_k} \cdot \hat{p}_{i_k}) R_v(\theta_{l_k}) (\hat{h}_s \cdot \hat{p}_{s_k}) + (\hat{h}_{i_k} \cdot \hat{q}_k) R_h(\theta_{l_k}) (\hat{h}_s \cdot \hat{q}_k) \quad (12)$$

and the Fresnel reflectivities are:

$$R_v(\theta_{l_k}) = \frac{\eta_1 \cos\theta_{l_k} - \eta_2 \sqrt{1 - \left(\frac{k_1}{k_2}\right)^2 \sin^2\theta_{l_k}}}{\eta_1 \cos\theta_{l_k} + \eta_2 \sqrt{1 - \left(\frac{k_1}{k_2}\right)^2 \sin^2\theta_{l_k}}} \quad (13)$$

$$R_h(\theta_{l_k}) = \frac{\eta_2 \cos\theta_{l_k} - \eta_1 \sqrt{1 - \left(\frac{k_1}{k_2}\right)^2 \sin^2\theta_{l_k}}}{\eta_2 \cos\theta_{l_k} + \eta_1 \sqrt{1 - \left(\frac{k_1}{k_2}\right)^2 \sin^2\theta_{l_k}}} \quad (14)$$

where η_1 and η_2 are the intrinsic impedances and k_1 and k_2 are the wave numbers of free space and the surface material, respectively. Here, $\theta_{l_k} = \cos^{-1}(\hat{n}_k \cdot \hat{k}_s)$ is the angle between the facet and the observation direction. The facet unit vectors are:

$$\begin{aligned} \hat{q}_k &= \frac{\hat{k}_s \times \hat{n}_k}{|\hat{k}_s \times \hat{n}_k|} = \frac{\hat{k}_i \times \hat{n}_k}{|\hat{k}_i \times \hat{n}_k|} \\ \hat{p}_{i_k} &= \hat{q}_k \times \hat{k}_{i_k} \\ \hat{p}_{s_k} &= \hat{q}_k \times \hat{k}_s \end{aligned} \quad (15)$$

The scattered radiation $\overline{T}_{s_k}(\hat{k}_s)$ from a facet can be related to the incident radiation from direction $\hat{k}_{i_k}$ using the Stokes' matrix:

$$\overline{T}_{s_k}(\hat{k}_s) = \begin{bmatrix} T_{s_{vk}} \\ T_{s_{hk}} \\ T_{s_{Uk}} \\ T_{s_{Vk}} \end{bmatrix} =$$

$$\begin{bmatrix} |f_{vv_k}|^2 & |f_{vh_k}|^2 & Re\{f_{vv_k} f_{vh_k}^*\} & -Im\{f_{vv_k} f_{vh_k}^*\} \\ |f_{hv_k}|^2 & |f_{hh_k}|^2 & Re\{f_{hv_k} f_{hh_k}^*\} & -Im\{f_{hv_k} f_{hh_k}^*\} \\ 2Re\{f_{vv_k} f_{hv_k}^*\} & 2Re\{f_{vh_k} f_{hh_k}^*\} & Re\{f_{vv_k} f_{hh_k}^* + f_{vh_k} f_{hv_k}^*\} & -Im\{f_{vv_k} f_{hh_k}^* - f_{vh_k} f_{hv_k}^*\} \\ 2Im\{f_{vv_k} f_{hv_k}^*\} & 2Im\{f_{vh_k} f_{hh_k}^*\} & Im\{f_{vv_k} f_{hh_k}^* + f_{vh_k} f_{hv_k}^*\} & Re\{f_{vv_k} f_{hh_k}^* - f_{vh_k} f_{hv_k}^*\} \end{bmatrix} \cdot \begin{bmatrix} T_{i_{vk}} \\ T_{i_{hk}} \\ T_{i_{Uk}} \\ T_{i_{Vk}} \end{bmatrix} \quad (16)$$

where $\overline{T}_{i_k}$ is the incident Stokes' vector for direction $\hat{k}_{i_k}$. For a single-scattering facet $\overline{T}_{i_k}$ is the unpolarized downwelling brightness field (i.e., $T_{i_{vk}} = T_{i_{hk}}$ and $T_{i_{Uk}} = T_{i_{Vk}} =$

0). All facets are assumed to scatter incoherently. Thus, their contributions to the total scattered radiation field $\overline{T}(\hat{k}_s)$ add:

$$\overline{T}_s(\hat{k}_s) = \int_{-\infty}^{\infty}\int_{-\infty}^{\infty} \overline{T}_{s_k}(\hat{k}_s)\, p(\alpha,\beta)\, d\alpha d\beta \tag{17}$$

In the expression above, $p(\alpha,\beta)$ is the probability of a facet having slopes $\alpha = \partial f/\partial x$ and $\beta = \partial f/\partial y$ where the surface is described by $z = f(x,y)$. Accordingly,

$$\hat{n}_k = \frac{-\alpha\hat{x} - \beta\hat{y} + \hat{z}}{\sqrt{\alpha^2+\beta^2+1}} \tag{18}$$

For a single-scattering facet, the thermal emission $\overline{T}_{e_k}(\hat{k}_s)$ can be polarized, but T_V is zero. To see this, consider a facet of kinetic temperature T. Using detailed balancing, the principles of reciprocity and conservation of energy can be used to find the thermal emission. In the $\hat{p}_{s_k} - \hat{q}_{s_k}$ basis this is:

$$\overline{T}'_{e_k}(\hat{k}_s) = \begin{bmatrix} (1-|R_v(\theta_{l_k})|^2)\,T \\ (1-|R_h(\theta_{l_k})|^2)\,T \\ 0 \\ 0 \end{bmatrix} \tag{19}$$

Using the rotational transformation, this is written in the $\hat{v} - \hat{h}$ basis as:

$$\overline{T}_{e_k}(\hat{k}_s) = \begin{bmatrix} (1-\cos^2\phi_r|R_v(\theta_{l_k})|^2 - \sin^2\phi_r|R_h(\theta_{l_k})|^2)\,T \\ (1-\sin^2\phi_r|R_v(\theta_{l_k})|^2 - \cos^2\phi_r|R_h(\theta_{l_k})|^2)\,T \\ \sin 2\phi_r(|R_v(\theta_{l_k})|^2 - |R_h(\theta_{l_k})|^2)T \\ 0 \end{bmatrix} \tag{20}$$

where ϕ_r is the angle of rotation between the two bases:

$$\phi_r = \frac{\hat{n}_k \cdot \hat{h}_s}{|\hat{n}_k \cdot \hat{h}_s|}\cos^{-1}(\hat{h}_s \cdot \hat{q}_k) \tag{21}$$

Thus, facet emission with nonzero T_U is possible, but T_V emission is always zero provided that the medium is isotropic. As in the case of the scattered radiation the orientationally-averaged emission becomes:

$$\overline{T}_e(\hat{k}_s) = \int_{-\infty}^{\infty}\int_{-\infty}^{\infty} \overline{T}_{ek}(\hat{k}_s)\, p(\alpha,\beta)\, d\alpha d\beta \tag{22}$$

The total upwelling radiation field is:

$$\overline{T}(\hat{k}_s) = \overline{T}_s(\hat{k}_s) + \overline{T}_e(\hat{k}_s) \tag{23}$$

For deterministic surfaces, $p(\alpha,\beta)$ is replaced by the fractional projected area of a given surface element:

$$p(\alpha,\beta)\,d\alpha d\beta \rightarrow \frac{(\hat{n}_k \cdot \hat{k}_s)\,dS}{\iint_S (\hat{n}_k \cdot \hat{k}_s)\,dS} \tag{24}$$

Here, $(\hat{n}_k \cdot \hat{k}_s)$ accounts for the projected area of the facet in the scattering direction, and the denominator normalizes the function. The surface integral is over only the portion of the surface that can be seen from direction $\hat{k}_s$, thereby accounting for shadowing. Written as an integral over the $x-y$ plane, the upwelling radiation becomes:

$$\overline{T}(\hat{k}_s) = \frac{\int_{-\infty}^{\infty}\int_{-\infty}^{\infty} [\overline{T}_{ek}(\hat{k}_s) + \overline{T}_{sk}(\hat{k}_s)]\,(\hat{n}_k \cdot \hat{k}_s)\sqrt{1+\alpha^2+\beta^2}\,dxdy}{\int_{-\infty}^{\infty}\int_{-\infty}^{\infty} (\hat{n}_k \cdot \hat{k}_s)\sqrt{1+\alpha^2+\beta^2}\,dxdy} \tag{25}$$

where the Jacobian of the transformation from surface coordinates to the $x-y$ plane is used. Again, shadowed regions are excluded.

Consider the GO model applied to the sinusoidal surface $f(x,y) = h\sin(2\pi x/\Lambda)$, where h is the peak wave amplitude and Λ is the surface wavelength. Here, $\alpha = (2\pi h/\Lambda)\cos(2\pi x/\Lambda)$ and $\beta = 0$. At large enough observation angles, multiple scattering either with or without shadowing can occur. Thresholds for the onsets of both multiple scattering and shadowing, in terms of θ_s, are shown for sinusoidal surfaces as a function of wave height for $\phi_s = 0$ in Fig. 4. For θ_s beyond the multiple scattering threshold, the $\hat{k}_{i_k}$ associated with some surface facets intersect the surface at other facets (Fig. 5). Accordingly, the unpolarized downwelling background brightness $\overline{T}_{i_k}$, must be replaced by the brightness of the facet at the point of intersection:

$$\overline{T}_{i_k} = \overline{T}^{(2)}_{e_k}(\hat{k}_{i_k}) + \overline{T}^{(2)}_{s_k}(\hat{k}_{i_k}) \tag{26}$$

where the superscript $^{(2)}$ indicates radiation from the second facet. The process is repeated if the $\hat{k}_{i_k}$ for the second facet intersects the surface again. Note that the incident brightness illuminating the primary facet is not necessarily unpolarized. Consequently, T_V is not necessarily zero in the case of multiple scattering, even if the surface medium is homogeneous and isotropic. Shadowing occurs when the $\hat{k}_s$ from any facet intersects the surface; shadowing is always accompanied by multiple scattering. For example, for $h/\Lambda = 0.05$ multiple scattering can occur for $\theta_s \gtrsim 51^\circ$ and shadowing can occur for for $\theta_s > \tan^{-1}[\Lambda/(2\pi h)] \approx 72^\circ$.

Use of the GO model is justified by considering the domain of applicability of the Kirchoff approximation (KA). As discussed by Wirgin [1983], the KA for a sinusoidal surface is applicable for $h\lambda/\Lambda^2 \ll 0.011$ for $\theta_s = 0$, where λ is the electrical wavelength. Applying this criterion to a periodic water surface with $\Lambda \sim 10$ cm and $h \sim 0.5$ cm, it is seen that the KA is indeed applicable at 91.65 GHz ($\lambda = 3.3$ mm) for normal observation. As shown in the next section by the good agreement between theory and experiment, this KA criterion appears conservative for polarimetric emission studies. For surfaces that are uniformly illuminated over at least several water periods Λ, (20) need be performed over only a single period. That is, any local brightness variations over the surface are adequately filtered by the antenna beam. This is the case for the experiments described herein.

4. Computed and Measured Results

Calculations of T_v, T_h and T_U based on the GO model for a sinusoidally-striated fresh water surface are shown in Fig. 6a-c. The calculations use $h/\Lambda = 0.05$ and are for observation angles $0 \leq \theta_s \leq 68°$ and $0 \leq \phi_s \leq 90°$. The brightnesses for all other quadrants in ϕ_s can be obtained by symmetry: T_v and T_h have even symmetry about $\phi_s = 0°$ and $\phi_s = 90°$ [i.e., $T_v(\phi_s) = T_v(-\phi_s)$ and $T_v(90 + \phi_s) = T_v(90 - \phi_s)$], while T_U has odd symmetry about $\phi_s = 0°$ and $\phi_s = 90°$ [i.e., $T_U(\phi_s) = -T_U(-\phi_s)$ and $T_U(90 + \phi_s) = -T_U(90 - \phi_s)$]. The dielectric parameterization of *Klein and Swift* [1977] at 91.65 GHz and at a temperature of $T_w = 290$ K is used for the water permittivity, resulting in $\epsilon_2 = 7.39 - j\,12.38$. The unpolarized downwelling radiation field is computed using the radiative transfer model described by *Gasiewski and Staelin* [1990] with a US standard atmosphere temperature profile interpolated to July at 34° N latitude. The water vapor profile was exponentially decaying with a 2 km scale height and 50% surface relative humidity (SRH). The figures for T_v and T_h show only the differences with respect to the vertical and horizontal brightnesses of a calm water surface, indicated by $T_v^{(c)}$ and $T_h^{(c)}$ (respectively).

Three characteristic ranges in the relationships between T_v, T_h and T_U and water wave angle can be identified, each corresponding to particular ranges of θ_s. When $0° \leq \theta_s \lesssim 35°$, T_v decreases, T_h increases and T_U remains negative as ϕ_s is moved from 0° (parallel to the water wave vector) to 90° (perpendicular to this vector). At nadir, ($\theta_s = 0°$) purely sinusoidal variations of $\sim 2 - 4$ K are found in all

three parameters; this follows from elementary properties of the Stokes' parameter rotation matrix. At $\theta_s \sim 40°$, T_v, T_h and T_U are essentially constant in ϕ_s; such angles would not be useful for observing wave direction. When $\theta_s \gtrsim 45°$, T_v increases and T_U remains positive as ϕ_s is moved from 0 to 90°. However, for $\theta_s \gtrsim 50°$, multiple scattering causes non-monotonic behavior in T_h as ϕ_s varies.

The above behavior can be conveniently described using the azimuthal Fourier amplitudes $B_{\alpha n}$ and phases $\Phi_{\alpha n}$, defined by:

$$T_\alpha(\theta_s, \phi_s) = \sum_{n=0}^{\infty} B_{\alpha n}(\theta_s) \cos[n\phi_s + \Phi_{\alpha n}(\theta_s)] - T_\alpha^{(c)} \tag{27}$$

where $T_\alpha^{(c)}$ is the calm water brightness. In general these coefficients are functions of θ_s, as illustrated in Figs. 7a-c for $n = 0, 2$, The $B_{\alpha 0}$ (Fig. 7a) are the azimuthally-averaged brightness changes caused by the water waves. Even for this "DC" case values of B_{v0} and B_{h0} exceeding 5 K at nadir and 20 K for T_h at $\theta_s \sim 55°$ are seen. Thus, the presence of small water waves can significantly change the azimuthally-averaged brightness. For $\theta_s \lesssim 50°$ the change is positive; this is a result of an increased fraction of the total scattered radiation originating from lower (and hence warmer) sky elevation angles. However, for $\theta_s \gtrsim 50°$ this change is negative for T_v and trending toward negative for T_h. For T_v this is a result of a reduction in surface emission caused by the spread in facet angle distribution: the well-known null in reflectivity near the Brewster angle is not as distinct nor deep when waves are present. For T_h the decreasing trend is a result of multiple scattering: more of the radiation is multiply-scattered and originates from higher (and hence colder) sky elevation angles when waves are present. As expected from symmetry, $B_{U0} = 0$.

The $B_{\alpha 2}$ (Figs. 7b and c) and associated phases $\Phi_{\alpha 2}$ clearly show the three characteristic ranges of θ_s. Over $0° \leq \theta_s \lesssim 35°$, B_{v2} and B_{h2} are of comparable magnitude but opposite sign. At nadir ($\theta_s = 0°$), these two coefficients are precisely equal and opposite ($B_{v2} = B_{h2}$, $\Phi_{v2} = 0°$, $\Phi_{h2} = -180°$) and $|B_{Un}| = 2 * |B_{v2}| = 2 * |B_{h2}|$; at nadir all $B_{\alpha n}$ are identically zero except for $n = 0, 2$. Near $\theta_s \sim 40°$ all $B_{\alpha 2}$ exhibit nulls and sign reversals. A second sign reversal is observed in B_{h2} at $\sim 58°$ as multiple scattering becomes significant. Note that the Φ_{U2} is always $\pm 90^0$, while Φ_{v2} and Φ_{h2} are always either 0° or 180°. That is, T_U is in phase quadrature with T_v and T_h. One important consequence of this is that observations of T_U along with coincident observations of T_v and T_h will facilitate the retrieval of wave direction

by removing ambiguities in the quadrant of the wave azimuthal angle [*Kunkee and Gasiewski*, 1993]. All B_{an} are zero for odd n, as expected for a symmetric surface. Higher order coefficients (B_{an} for $n > 2$) are generally nonzero, but usually too small to be of practical importance. An exception is B_{h4}, which has a maximum amplitude of ~ 4 K at $\theta_s \approx 58°$.

Measurements of T_v, T_h, and T_U at $\theta_s = 20°$, $39°$ and $65°$ using the 91.65 GHz polarimetric radiometer are compared with computed GO brightnesses in Figs. 8-10. These three observation angles lie within each of the characteristic ranges described above. All measurements were over a sinusoidally striated water surface with $h \approx 0.5$ cm and $\Lambda \approx 10$ cm under clear skies. The radiometric noise on each measurement is ~ 0.2 K and the bias is $\lesssim 3-5$ K. To minimize the effects of instrument drift, the data have been corrected by first subtracting the measured calm water brightness $T_a^{(c)}$ at each azimuthal angle, then adding the average measured calm water brightness $\langle T_a^{(c)} \rangle$. The calm water measurement was made after turning off the wave tank plunger and allowing the waves to dissipate.

Overall, the amplitudes and phases of the azimuthal variations in the measured brightnesses corroborate the GO model well. As predicted, the amplitude variations at $\theta_s = 39°$ are relatively small, while near nadiral ($\theta_s = 20°$) and near-grazing ($\theta_s = 65°$) measurements both show significant variations. In general, these variations are large enough to warrant consideration in many remote sensing problems. The sharp features in T_h and T_U for $\theta_s = 65°$ are the result of multiple scattering of order two (double scattering). Indeed, due to the larger local reflectivity for $h-$ compared to $v-$polarization multiple scattering is more strongly manifested in T_h than in T_v. The dashed lines in Figs. 10a and b show GO simulations obtained when multiple scattering is neglected. In this case the model seriously conflicts with the measurements, thus clearly demonstrating the need to account for multiple scattering at large observation angles. The absence of sharp features in the measured T_h and T_U data at $\theta_s = 65°$ is primarily the result of imperfect sinusoidal water waves: small capillary waves from air gusts and vibrations were often superimposed on the dominant gravity waves.

Other discrepancies between the measured and computed brightnesses include small biases of ~ 3 K in the measured values of T_v for $\theta_s = 20°$ and ~ -4 K in

T_h for $\theta_s = 39°$. In addition, the amplitude of T_U for $\theta_s = 20°$ is only $\sim 60\%$ of the computed value. These errors can be attributed to beam spillover, absolute calibration errors, water surface inhomogeneities, and errors in the computed downwelling brightness field.

5. Physical Basis for Polarimetric Signatures

Insight into the relationship between various geophysical parameters and variations in the upwelling polarimetric brightness can be obtained by writing the upwelling surface brightness in terms of the bistatic scattering function $\gamma_{\beta\alpha}$ [*Tsang et al.*, 1985]:

$$T_\alpha(\theta_s,\phi_s) = \frac{1}{4\pi}\sum_\beta \int_0^{2\pi}\int_0^{\pi/2} \gamma_{\beta\alpha}(\theta_s,\phi_s,\theta_i,\phi_i)\, T_\beta(\theta_i,\phi_i)\, \sin\theta_i d\theta_i d\phi_i + T_w\,[1-r_\alpha(\theta_s,\phi_s)] \tag{28}$$

where the surface reflectivity $r_\alpha(\theta_s,\phi_s)$ is:

$$r_\alpha(\theta_s,\phi_s) = \frac{1}{4\pi}\sum_\beta \int_0^{2\pi}\int_0^{\pi/2} \gamma_{\beta\alpha}(\theta_s,\phi_s,\theta_i,\phi_i)\, \sin\theta_i d\theta_i d\phi_i \tag{29}$$

The downwelling background brightness can be considered to be the sum of an average component weighted over all incident angles and an angularly varying component:

$$T_\beta(\theta_i,\phi_i) = \langle T(\theta_i,\phi_i)\rangle + \delta T_\beta(\theta_i,\phi_i) \tag{30}$$

where

$$\langle T(\theta_i,\phi_i)\rangle \triangleq \frac{1}{4\pi}\sum_\beta \int_0^{2\pi}\int_0^{\pi/2} T'_\beta(\theta_i,\phi_i)\, \sin\theta_i d\theta_i d\phi_i \tag{31}$$

With reference to (27), the second-harmonic azimuthal Fourier coefficient can now be written as:

$$\begin{aligned} B_{\alpha 2}(\theta_s) = 2\Big|&[\langle T(\theta_i,\phi_i)\rangle - T_w] r_{\alpha 2}(\theta_s) \\ &+ \frac{1}{4\pi}\sum_\beta \int_0^{2\pi}\int_0^{\pi/2} \delta T_\beta(\theta_i,\phi_i)\, \gamma_{\beta\alpha 2}(\theta_s,\theta_i,\phi_i)\, \sin\theta_i d\theta_i d\phi_i\Big| \end{aligned} \tag{32}$$

where

$$r_{\alpha n}(\theta_s) = \frac{1}{2\pi}\int_0^{2\pi} r_\alpha(\theta_s,\phi_s)\, e^{-j2\pi n\phi_s}\, d\phi_s \tag{33}$$

is the n^{th} azimuthal Fourier coefficient of the surface reflectivity, and

$$\gamma_{\beta\alpha n}(\theta_s,\theta_i,\phi_i) = \frac{1}{2\pi}\int_0^{2\pi} \gamma_{\beta\alpha}(\theta_s,\phi_s,\theta_i,\phi_i)\, e^{-j2\pi n\phi_s}\, d\phi_s \tag{34}$$

is the n^{th} azimuthal Fourier coefficient of $\gamma_{\beta\alpha}$ with respect to ϕ_s.

The second harmonic amplitude $B_{\alpha 2}$ is influenced by two independent geophysical effects, described by the two terms in (32). The first effect results from variations in the total surface reflectivity r_α (or equivalently, the surface emissivity) with ϕ_s, and is described by $[\langle T(\theta_i, \phi_i)\rangle - T_w] r_{\alpha 2}(\theta_s)$. This effect causes surface emission and reflection harmonics in T_α which are by nature of opposite phase. The second effect results from both elevational variations in the angular distribution of the downwelling $T_\beta(\theta_i, \phi_i)$ and azimuthal variations in the bistatic scattering function $\gamma_{\beta\alpha}$, and is described by the integral in (32). This effect causes background-induced harmonics in T_α.

Inspection of (32) shows that the amplitude of the second harmonic contains a component which is proportional to the difference between the weighted-average downwelling brightness and the water temperture. (This can easily be shown to be true for all harmonic orders.) Thus, a brightness contrast between the background and the surface temperature must be present to produce either surface or background harmonics. For example, if the background brightness was uniform over angle, unpolarized and identical to T_w then the upwelling surface brightness T_α would be unpolarized and equal to T_w at all angles ϕ_s.

The computed sensitivities of $B_{\alpha 2}$ to various parameters provide additional insight into the link between geophysical parameters and radiometric observables. Accordingly, the numerical derivatives $\partial B_{\alpha 2}/\partial(\%SRH)$, $\partial B_{\alpha 2}/\partial(h/\Lambda)$ and $\partial B_{\alpha 2}/\partial T_w$ are shown in Table 1 for three values of θ_s: $15°, 40°$ and $65°$, representative of the three characteristic ranges discussed in Section 4. The calculations use quiescent surface and atmospheric states identical to those of Figs. 7a and b.

Both positive and negative values of $\partial B_{\alpha 2}/\partial(\%SRH)$ are possible in clear air. This is explained by analyzing the components of $B_{\alpha 2}$ under small increments in the background humidity profile. For $\theta_s = 15°, 40°$ and $65°$, the surface harmonic component in (32) is reduced due to an overall warming of the background brightness profile. In general the background warming also reduces $\delta T(\theta_i, \phi_i)$, however, this reduction is not uniform over the entire sky: elevation angles near the horizon are increased by a larger amount than those near zenith. This phenomona is characteristic

of the stratified nature of the atmosphere and varies somewhat with the particular atmospheric quiescient state. Since $\gamma_{\beta\alpha 2}(\theta_s, \theta_i, \phi_i)$ exhibits both positive and negative values over θ_i, it is possible for the background-induced harmonic component in (32) to increase with a general warming of the background brightness profile. This is the case for all polarizations and for all three observation angles studied.

For $\theta_s \lesssim 30°$, the $n = 2$ surface emission harmonic dominates both the surface scattering and background-induced harmonics. Due to destructive interference of these harmonics, an increase in SRH decreases $B_{\alpha 2}$, as shown by the negative sensitivities in Table 1. When θ_s is increased to $\sim 40°$ surface emission continues to dominate B_{v2}, however, the surface scattering and background-induced harmonics dominate B_{h2} since the reflection coefficient is larger for $\alpha = h$. Thus, the sensitivity values in Table 1 for $\alpha = h$ are positive. For $\theta_s = 65°$, the $n = 2$ background-induced harmonics become large and dominate $B_{\alpha 2}$ for all polarizations, hence again the positive sensitivity values in Table 1. The background-induced harmonics are large when $\theta_s = 65°$ due to the rapidly changing background profile near the horizon along with the diffuse reflecting features of the sinusoidal surface (as described by $\gamma_{\beta\alpha 2}$) when the observation angle is near the Brewster angle of the calm water surface ($\sim 71°$).

6. Implications for Remote Sensing

The radiometric behavior under the GO model is a consequence of the slope distribution of a sinusoidal surface, the variance of which is $\sigma_s^2 = (\sqrt{2}\pi h/\Lambda)^2 \approx 0.049$. Consider spaceborne passive remote sensing of ocean wave direction. For the open ocean, the slope distribution can be approximated using the model of *Cox and Munk* [1954; *Wilheit*, 1979], which has the following variance:

$$\sigma_o^2 = 0.003 + 0.0048\, w \tag{35}$$

where w is the wind speed at a height of 20-m above the surface. Using $w = 7$ m/sec (the most probable value) we obtain $\sigma_o^2 \approx 0.037$, a value comparable to σ_s^2. Thus, azimuthal brightness signatures of comparable amplitude can be expected over striated portions of ocean. For θ_s outside of the range $35 - 45°$ the signatures are expected to be large enough for remote sensing of ocean wave direction, particularly for $\theta_s \gtrsim 50°$. However, signature amplitudes can be expected to be reduced somewhat by ocean foam, non-directional wave spectra and horizontal spectral inhomogeneity.

Since the azimuthal signature for T_U is in phase quadrature with both T_v or T_h, measurements of T_U are expected to facilitate retrieval of ocean wave direction modulo 180° by reducing the ambiguity in the quadrant of the wave direction from fourfold to twofold ([e.g., *Etkin et al.*, 1993]. Since a real ocean surface is not symmetric the Fourier amplitudes $B_{\alpha n}$ for odd n are nonzero. This was shown by *Wentz* [1992] for $\alpha = v, h$ using SSM/I data, and explained by an excess of leeward-side foam. Thus, elimination of the remaining 180° ambiguity is expected to be facilitated by the natural ocean wave asymmetry. In principle, ocean wave direction should be unambiguously measurable from single polarimetric observations, preferably at a large incident angle. In practice, the presence of foam, non-directional spectra and spectral inhomogeneity will likely necessitate additional observations at several azimuthal angles.

Although the downwelling brightness field and the water vapor opacity between the surface and a space-based observer ($\lesssim$ 3 dB) affect the characteristics of the azimuthal radiometric features, signatures useful for ocean wave direction sensing at millimeter-wave frequencies (at least a few Kelvin in amplitude) should be observable from space in clear air under nearly all humidity conditions and under light ($\lesssim$ 0.1 kg/m^2) cloud cover. Indeed, the downwelling brightness depends on both the columnar water vapor content of the atmosphere and the amount of cloud water. At 90 GHz and under US standard atmosphere conditions the clear-air zenith brightness ranges from $\sim$ 15 K for 0% SRH to $\sim$ 75 K for 100% SRH, and can increase to $\sim$ 145 K under saturated tropical summer conditions. In any of these cases the brightness contrast between the background and surface is large enough ($\sim 150 - 260$ K) to produce observable signatures. For somewhat heavier clouds (0.1 g/m^3 from 1 km to 5 km altitude) the zenith brightness increases to $\sim 190 - 220$ K. Under such conditions the brightness contrast is reduced to $\sim 50 - 80$ K, and the amplitude of the azimuthal Fourier harmonics are reduced to $\sim$ 30% of their clear-air values. In this case azimuthal brightness signatures might be observable from low-flying aircraft, but cloud opacity ($\sim 6 - 8$ dB) would render them practically unobservable from space. The impact of clouds on spaceborne surface measurements is considerably reduced at lower frequencies (e.g., $\sim$ 18 and $\sim$ 37 GHz), albeit with reduced spatial resolution when using diffraction limited apertures of fixed size.

As shown in Table 1 by the sensitivity to the parameter (h/Λ) the Fourier

amplitudes generally increase with slope variance, and are particularly large for θ_s exceeding $\sim 50 - 60°$. The anisotropic effects of striated water surfaces should be most readily observed at such angles. Otherwise, the sensitivity to T_w is relatively small near 90 GHz. In addition, no significant changes occur upon incorporating salt at normal oceanic levels (3.5%).

The results of this study are also applicable to nadiral- or near-nadiral sounding of atmospheric parameters. For angles $\theta_s \lesssim 35°$, the GO model suggests that water waves with slope variances comparable to open ocean can cause peak-to-peak variations in the surface brightness of ~ 3 K, resulting in random variations of $\sim 1 - 2.5$ K in a 90-GHz window channel. Comparable variations have been shcwn to occur at 20- and 37-GHz over ocean [*Dzura et al.*, 1992]. The magnitude of these variations are large enough to warrant consideration in algorithms for water vapor and temperature sounding, atmospheric wet-path delay measurements, and in satellite climatological studies of parameters that might be statistically correlated with ocean wave or surface wind direction.

7. Summary

Presented in this study are the results of controlled partially polarimetric measurements of thermal emission at 91.65 GHz from a striated water surface as corroborated by a geometrical optics radiative model. The measurements were obtained outdoors using a precision polarimetric radiometer which directly measured the first three modified Stokes' parameters. Significant variations in these parameters as a function of azimuthal water wave angle were found, with peak-to-peak variations in T_U of up to $\sim$ 10 K. The measurements are well corroborated by the GO model over a range of observations angles from near nadir up to $\sim 65°$ from nadir. The model incorporates both multiple scattering and a realistic downwelling background brightness field.

Both the data and the GO model suggests three characteristic ranges of observation angle. The largest azimuthal signatures in T_v, T_h and T_U are found at observation angles beyond $\sim 50°$ from nadir. For $35° \lesssim \theta_s \lesssim 45°$ the azimuthal signatures practically vanish. For $\theta_s \leq 35°$ the azimuthal signatures are of smaller amplitude, with phase reversals occurring in T_v and T_U. The presence of water waves

was also noted to influence the azimuthally-averaged values of T_v and T_h by several Kelvins. Applications of the study include passive polarimetric remote sensing of ocean wave direction from space, oceanic wave studies from both space and aircraft, and prediction of polarimetric surface effects for atmospheric sounding.

Acknowledgements-This work has been supported by NASA grant NAG 5-1490 and the Georgia Institute of Technology. The authors are grateful to the NASA Goddard Space Flight Center for providing the 91.65 GHz radiometer.

References

Adler, R.F., R.A. Mack, N. Prasad, H.-Y.M. Yeh, and I.M. Hakkarinen, Aircraft Microwave Observations and Simulations of Deep Convection from 18-183 GHz. Part I: Observations, *J. Ocean. Atm. Tech.*, 7, 377-391, 1990.

Cox, C., and W. Munk, Measurement of the Sea Surface from Photographs of the Sun's Glitter, *J. Opt. Soc. America*, 44(11), 838-850, 1954.

Dzura, M.S., V.S. Etkin, A.S. Khrupin, M.N. Pospelov, M.D. Raev, Radiometers-Polarimeters: Principles of Design and Applications for Sea Surface Microwave Emission Polarimetry, *Proceedings of the 1992 IEEE International Geoscience and Remote Sensing Symposium (IGARSS)*, pp. 1432-1434, Houston, TX, 1992.

Etkin, V.S., A.V. Kuzmin, M.N. Pospelov, A.I. Smirnov, and V.V. Yalovlev, The Determination of Sea Surface Wind and Temperature with Airborne Radiometric Data, *Proceedings of the 1993 IEEE International Geoscience and Remote Sensing Symposium (IGARSS)*, pp. 1622-1624, Tokyo, 1993.

Evans, K.F., and J. Vivekanandan, Multiparameter Radar and Microwave Radiative Transfer Modeling of Nonspherical Atmospheric Ice Particles, *IEEE Trans. Geosci. Remote Sensing*, 28(4), 423-437, 1990.

Gasiewski, A.J., and D.H. Staelin, Numerical Modelling of Passive Microwave O_2 Observations Over Precipitation, *Radio Sci.*, 25(3), 217-235, 1990.

Gasiewski, A.J. A Technique for Measuring Vertically and Horizontally Polarized Brightness Temperatures Using Electronic Polarization Basis Rotation, *Proceedings of the 1990 IEEE International Geoscience and Remote Sensing Symposium (IGARSS)*, pp. 1569-1572, College Park, MD, 1990.

Gasiewski, A.J., and D.B. Kunkee, Laboratory Demonstration of Electronic Polarization Basis Rotation, *Proceedings of the 1992 IEEE MTT-S International Microwave Symposium (IMS)*, pp. 329-332, Albuquerque, NM, 1992.

Gasiewski, A.J., and D.B. Kunkee, Calibration and Applications of Polarization-

Correlating Radiometers, *IEEE Trans. Microwave Theory Tech.*, 41(5), 767-773, 1993.

Hollinger, J.P., J.L. Pierce, and G.A. Poe, SSM/I Instrument Evaluation, *IEEE Trans. Geosci. Remote Sensing*, 28(5), 781-790, 1990.

Ilyin, V.A., and V.Y. Raizer, Microwave Observations of Finite-Amplitude Water Waves, *IEEE Trans. Geosci. Remote Sensing*, 30(1), 1992.

Klein, L.A., and C.T. Swift, An Improved Model for the Dielectric Constant of Sea Water at Microwave Frequencies, *IEEE Trans. Ant. Prop.*, 25(1), 104-111, 1977.

Kunkee, D.B., and A.J. Gasiewski, Laboratory Measurements of Water Gravity Wave Characteristics Using Full Polarization Radiometry, *Proceedings of the 1993 National Radio Science Meeting*, p. 155, Boulder, CO, 1993.

Nghiem, S.V., M. Veysoglu, J.A. Kong, R.T. Shin, K. O'Neill and A. Lohanick, Polarimetric Passive Remote Sensing of a Periodic Soil Surface: Microwave Measurements and Analysis, *J. Electromagnetic and Waves Appl.*, 5(9), 997-1005, 1991.

Njoku, E.G., J.M. Stacey, and F.T. Barath, The Seasat Multichannel Microwave Radiometer (SMMR): Instrument Description and Performance, *IEEE J. Oceanic Eng.*, 5(2), 100-115, 1980.

Phillips, O.M., *The Dynamics of the Upper Ocean*, pp. 37-43, Cambridge University Press, London, 1980.

Spencer, R.W., A Satellite Passive 37-GHz Scattering-based Method for Measuring Oceanic Rain Rates, *J. Cli. Appl. Meteor.*, 25(6), 754-766, 1986.

Stogryn, A., The Apparent Temperature of the Sea at Microwave Frequencies, *IEEE Trans. Ant. Prop.*, 15(2), 278-286, 1967.

Tsang, L., J.A. Kong, and R.T. Shin, *Theory of Microwave Remote Sensing*, 613 pp., New York: John Wiley and Sons, 1985.

Veysoglu, M.E., Polarimetric Passive Remote Sensing of Periodic Surfaces and Anisotropic Media, S.M. Thesis, Department of Electrical Engineering and Computer Science, Massachusetts Institute of Technology, Cambridge, MA, 1991.

Veysoglu, M.E., H.A. Yueh, R.T. Shin and J.A. Kong, Polarimatric Passive Remote Sensing of Periodic Surfaces, *J. Electromagnetic and Waves Appl.*, 5(3), 267-280, 1991.

Wentz, F., Measurement of Oceanic Wind Vector Using Satellite Microwave Radiometers, *IEEE Trans. Geosci. Remote Sensing*, 30(5), 960-972, 1992.

Wilheit, T.T., A Model for the Microwave Emissivity of the Ocean's Surface as a Function of Wind Speed, *IEEE Trans. Geosc. Electron.*, 17(4), 244-249, 1979.

Wirgin, A. Scattering from Sinusoidal Gratings: An Evaluation of the Kirchoff Approximation, *J. Opt. Soc. Am.*, 73(8), 1028-1041, 1983.

Table 1: Computed sensitivities $\partial B_{\alpha 2}/\partial x$ for $x = \%SRH, (h/\Lambda)$ and T_w, and $\alpha = v, h, U$.

x	θ_s	$\partial B_{\alpha 2}/\partial x$ $\alpha = v$	$\alpha = h$	$\alpha = U$	Dimensions
$\%SRH$	15°	-0.014	-0.016	-0.030	(K/%)
	40°	-0.030	0.016	-0.052	
	65°	0.021	0.168	-0.056	
h/Λ	15°	63.2	53.3	116.9	(K)
	40°	22.1	82.4	-29.1	
	65°	213.2	304.2	319.7	
T_w	15°	0.009	0.006	0.014	(unitless)
	40°	0.018	0.002	0.016	
	65°	0.054	0.045	-0.003	

C-2

Figure 1: Block diagram of the 3-channel (v_A, v_B and v_C) polarization-correlating radiometer.

Figure 2: Experimental configuration for polarimetric radiometric measurements of emission from a striated water surface.

Figure 3: Geometry associated with the GO brightness model.

Figure 4: Multiple scattering and shadowing thresholds for a sinusoidal surface $z = h \sin(2\pi x/\Lambda)$.

Figure 5: Geometry associated with multiple scattering from a sinusoidal surface.

Figure 6: Computed upwelling brightness perturbations for $0^\circ \leq \theta_s = 68^\circ$, $0^\circ \leq \phi_s \leq 90^\circ$, $h/\Lambda = 0.05$ and a surface relative humidity of 50%: (a) $T_v - T_v^{(c)}$, (b) $T_h - T_h^{(c)}$, (c) T_U.

Figure 7: Azimuthal Fourier coefficients for the brightness perturbations in Figs. 6a-c: (a) DC Fourier amplitude, (b) 2^{nd} harmonic magnitude $B_{\alpha 2}$, and (c) 2^{nd} harmonic phase $\Phi_{\alpha 2}$.

Figure 8: Measured and calculated polarimetric brightnesses for $\theta_s = 20^\circ$, $T_w = 291\ K$, $h/\Lambda = 0.05$ and SRH = 85%: (a) T_v and T_h, (b) T_U.

Figure 9: Measured and calculated polarimetric brightnesses for $\theta_s = 39^\circ$, $T_w = 291\ K$, $h/\Lambda = 0.05$ and SRH = 80%: (a) T_v and T_h, (b) T_U.

Figure 10: Measured and calculated polarimetric brightnesses for $\theta_s = 65^\circ$, $T_w = 288\ K$, $h/\Lambda = 0.05$ and SRH = 50%: (a) T_v and T_h, (b) T_U. The dashed line in (a) and (b) shows the computed values of T_h and T_U (respectively) when multiple scattering is neglected.

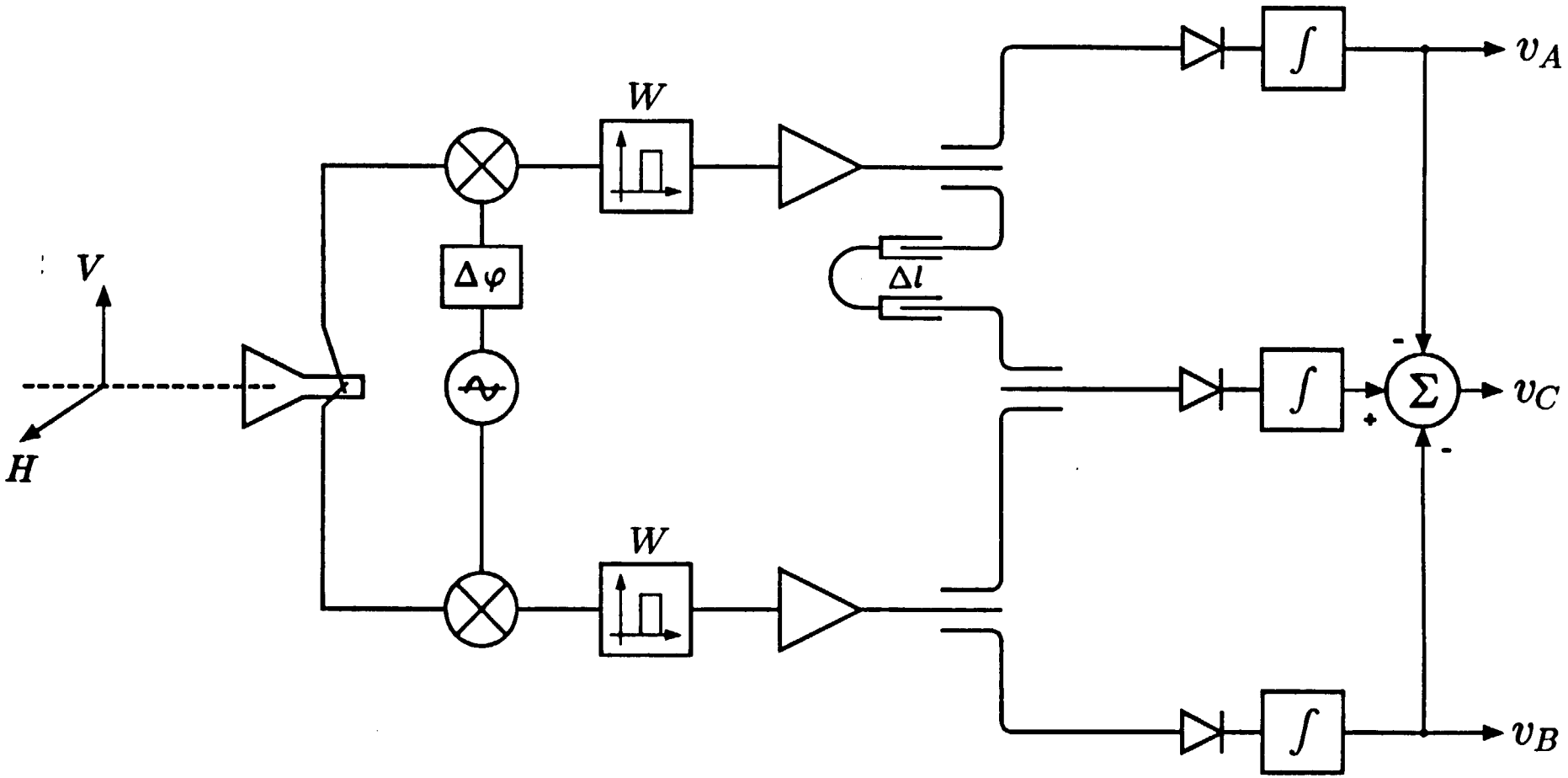

Figure 1

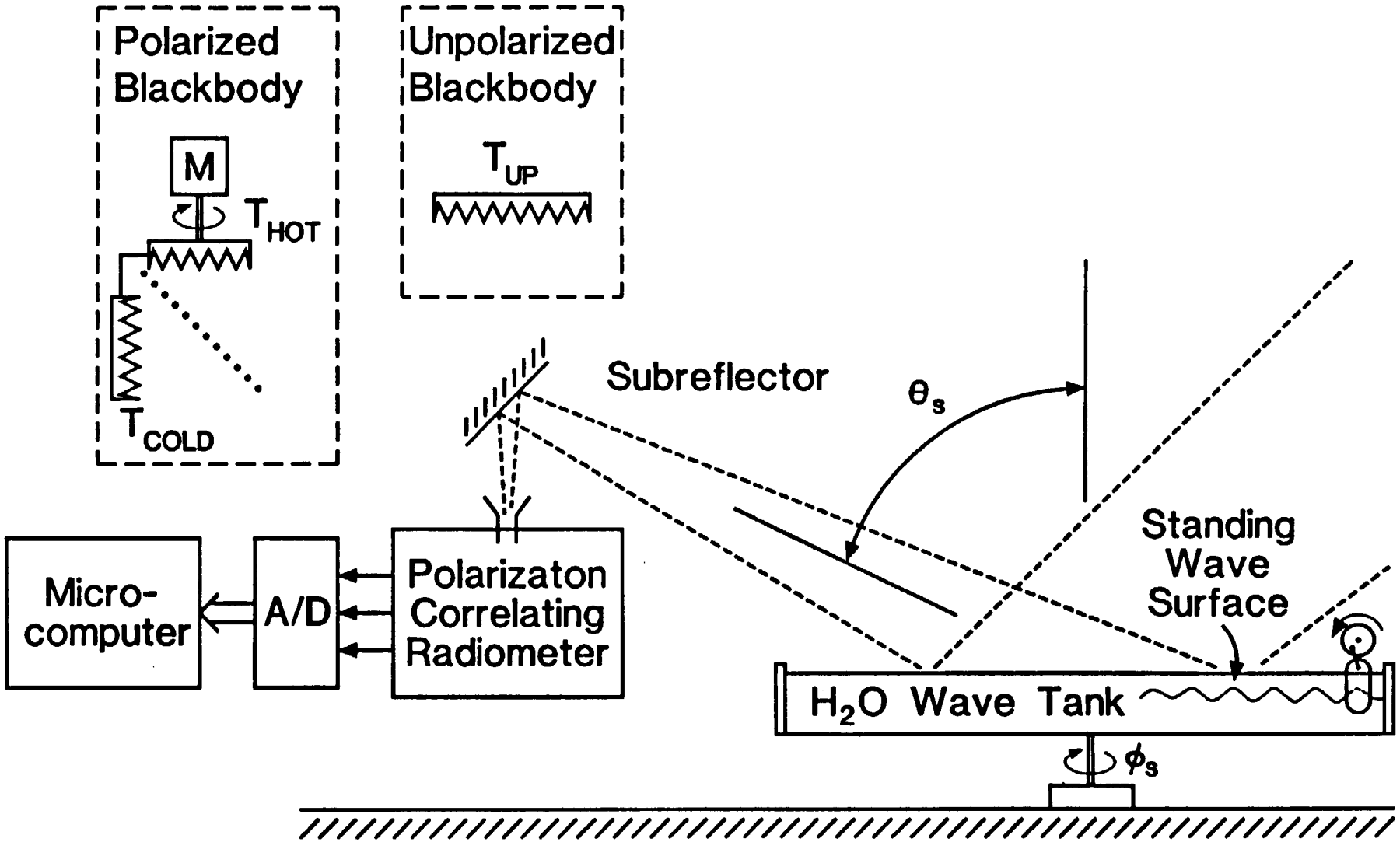
Polarized
Blackbody
M
T_{HOT}
T_{COLD}
Unpolarized
Blackbody
T_{UP}
Subreflector
θ_s
Standing
Wave
Surface
Micro-
computer
A/D
Polarizaton
Correlating
Radiometer
H_2O Wave Tank
ϕ_s

Figure 2

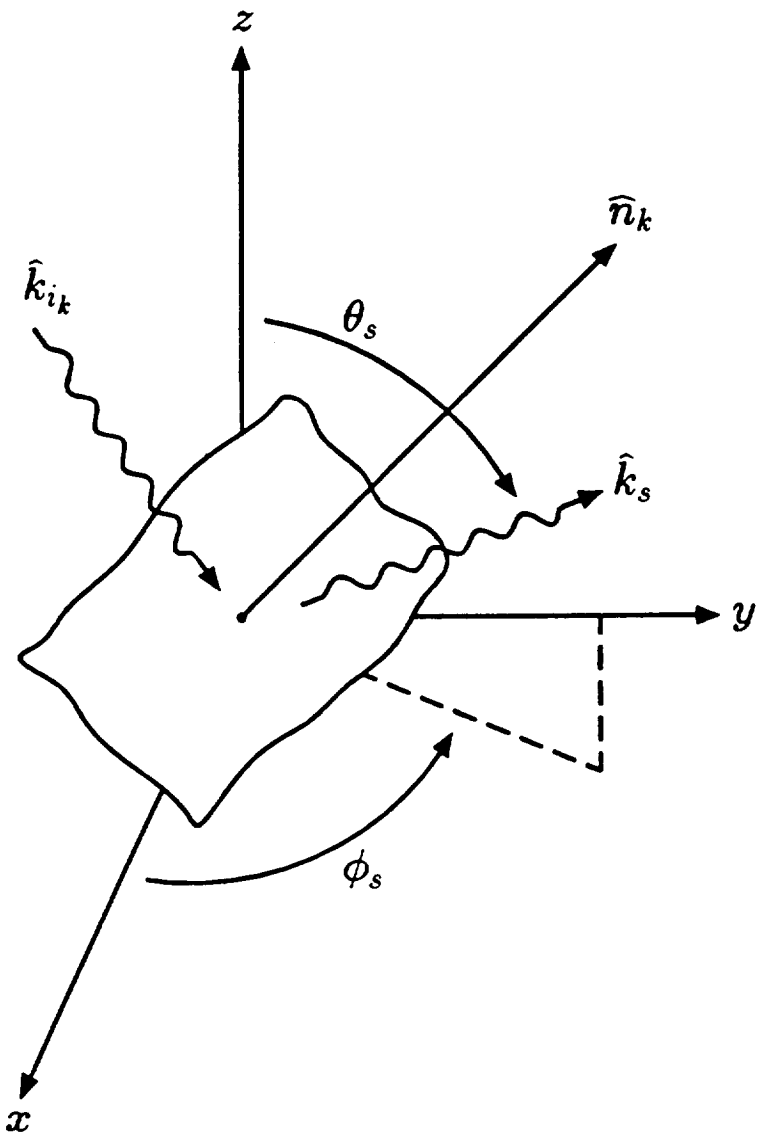

Figure 3

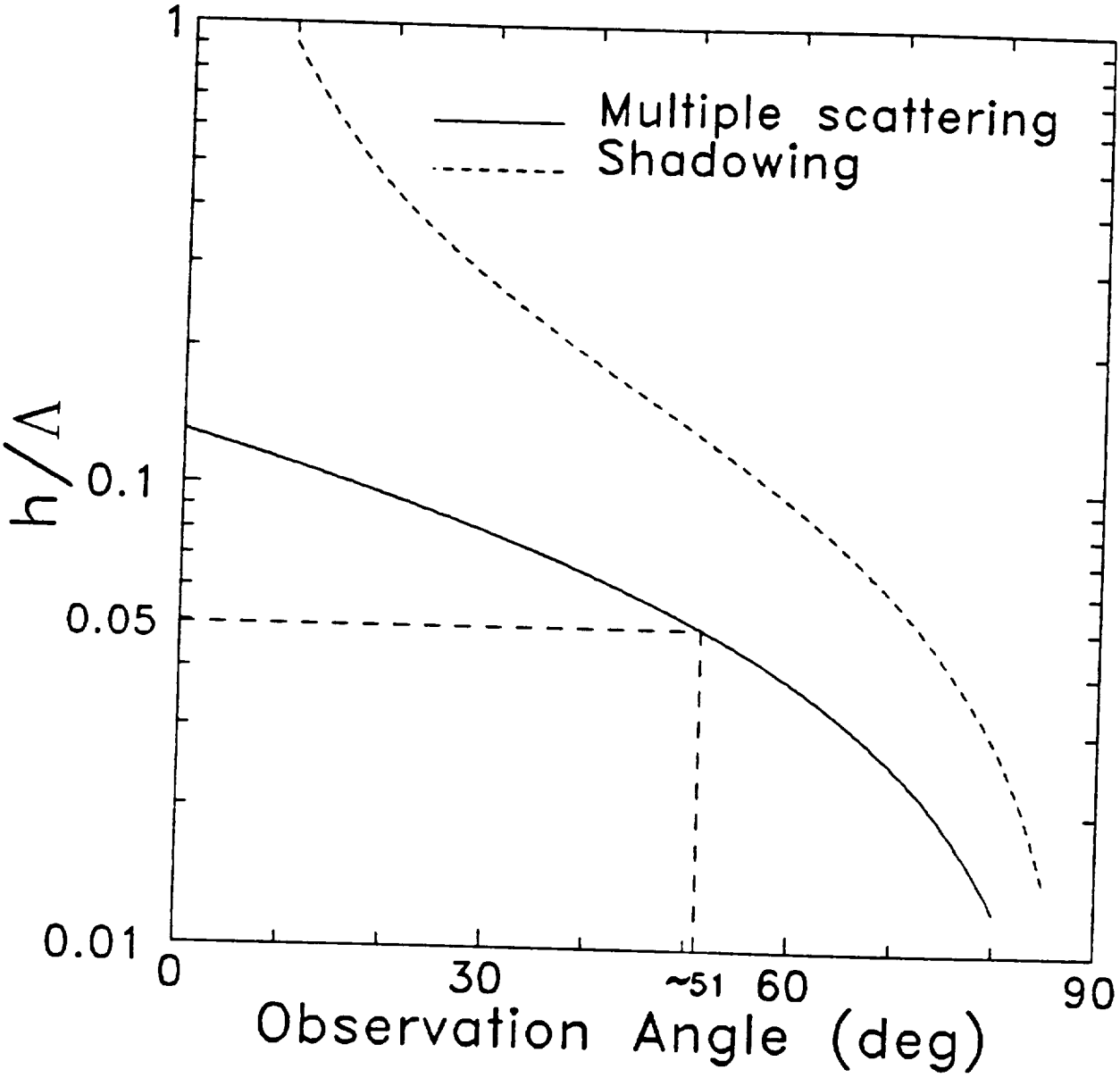
1
0.1
0.05
0.01
h/Λ
Multiple scattering
Shadowing
0
30
~51
60
90
Observation Angle (deg)

Figure 4

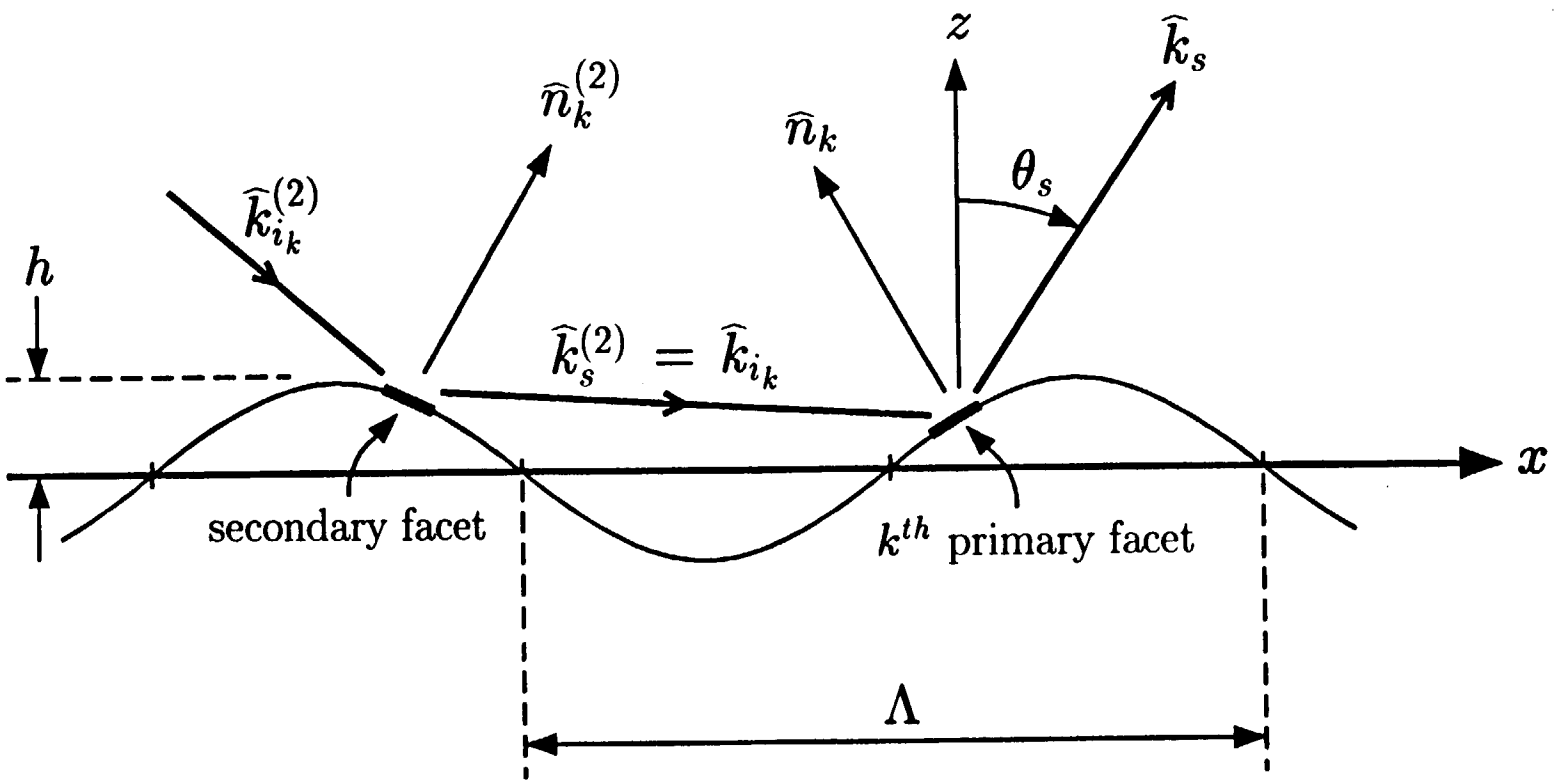
z
$\widehat{k}_s$
$\widehat{n}_k^{(2)}$
$\widehat{n}_k$
θ_s
$\widehat{k}_{i_k}^{(2)}$
h
$\widehat{k}_s^{(2)} = \widehat{k}_{i_k}$
x
secondary facet
k^{th} primary facet
Λ

Figure 5

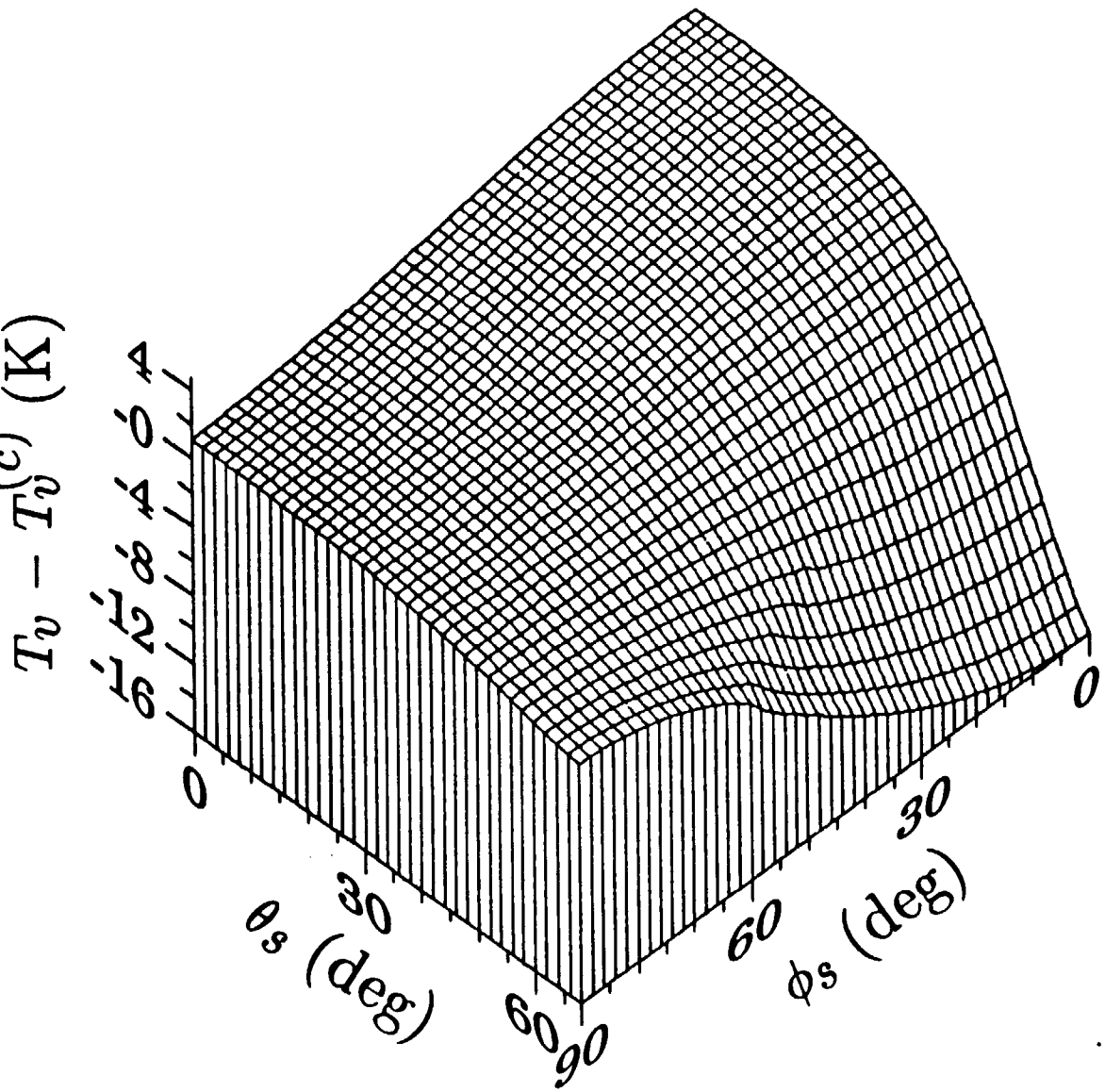

Figure 6a

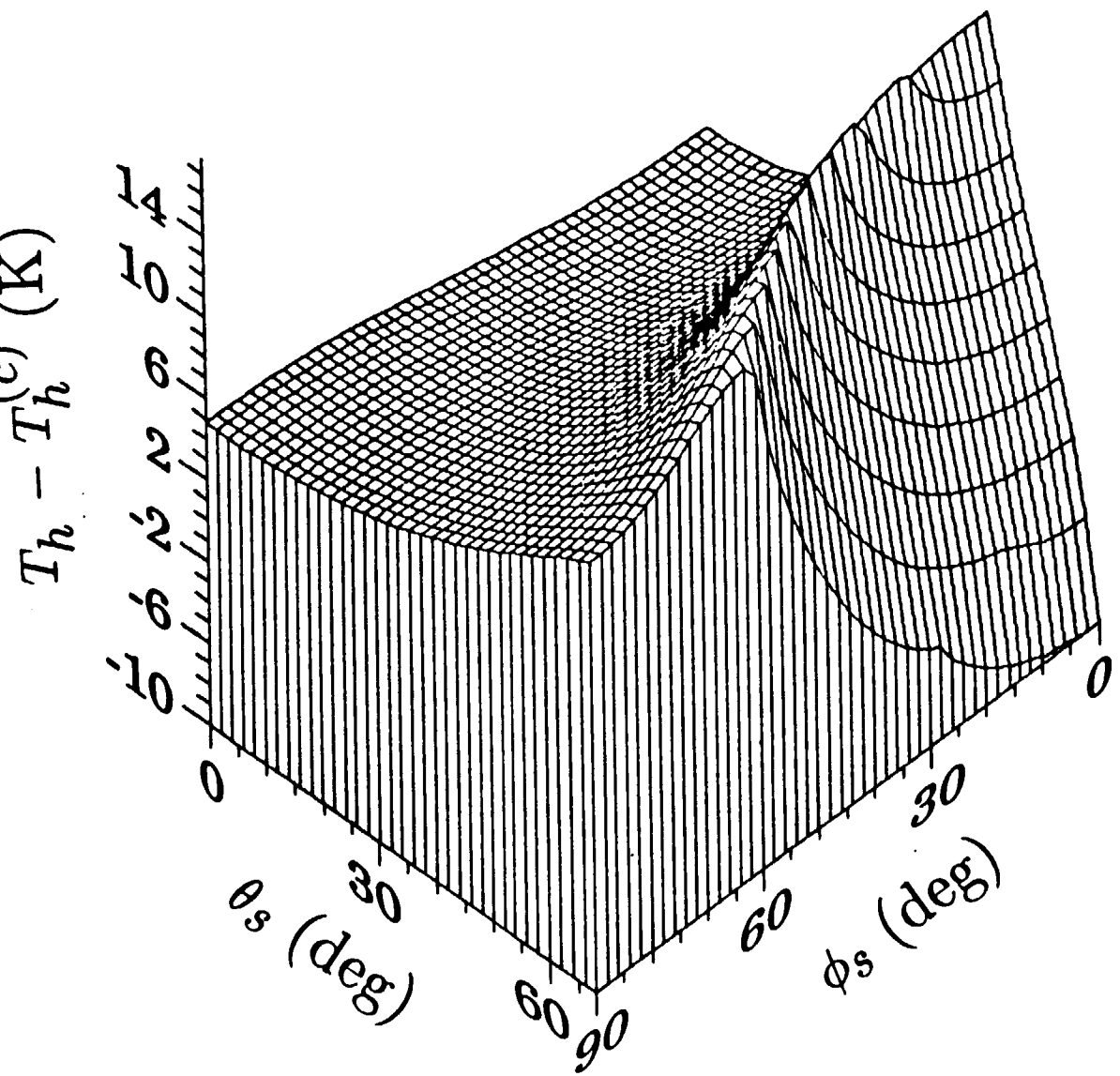

Figure 6b

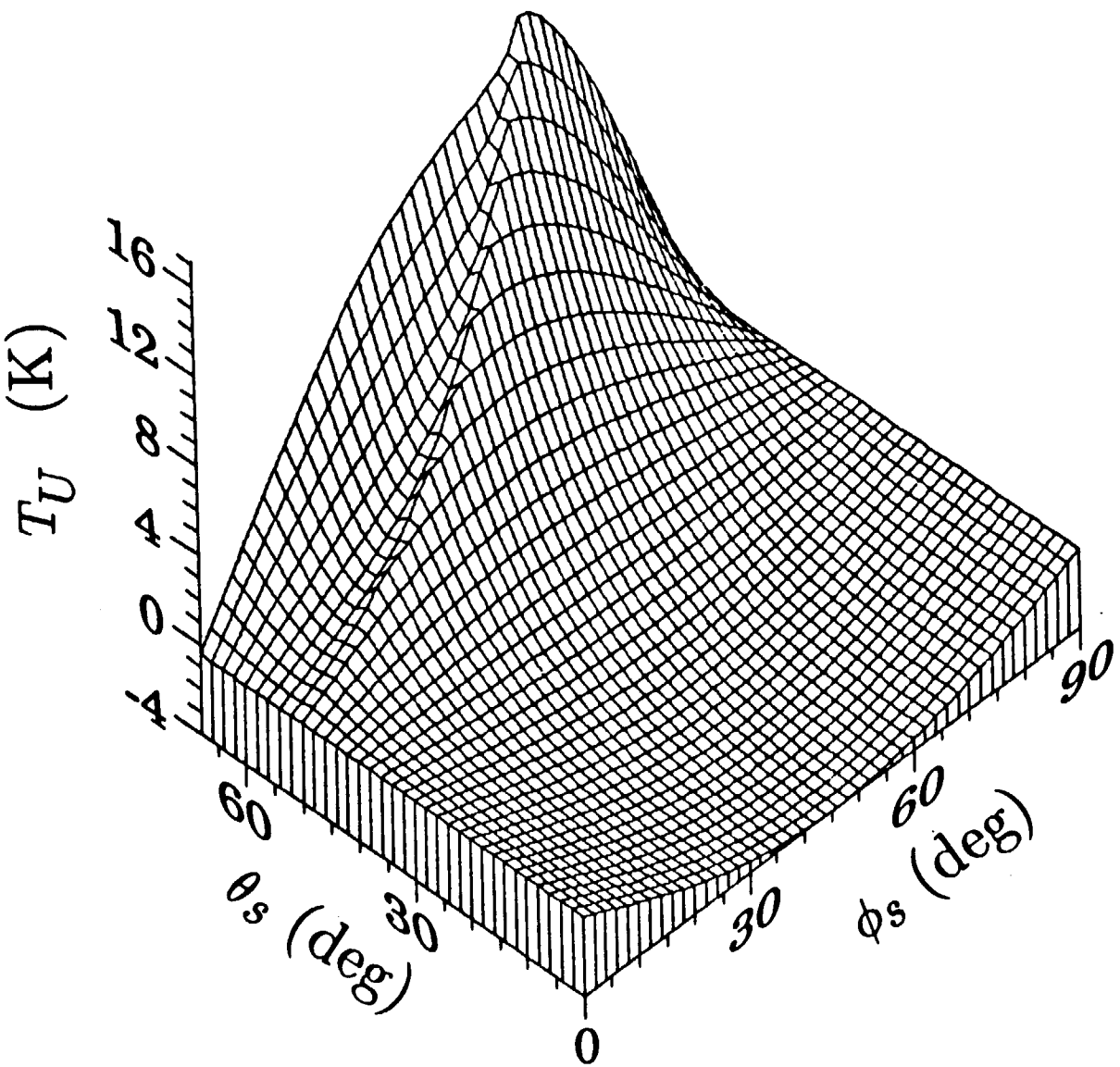

Figure 6c

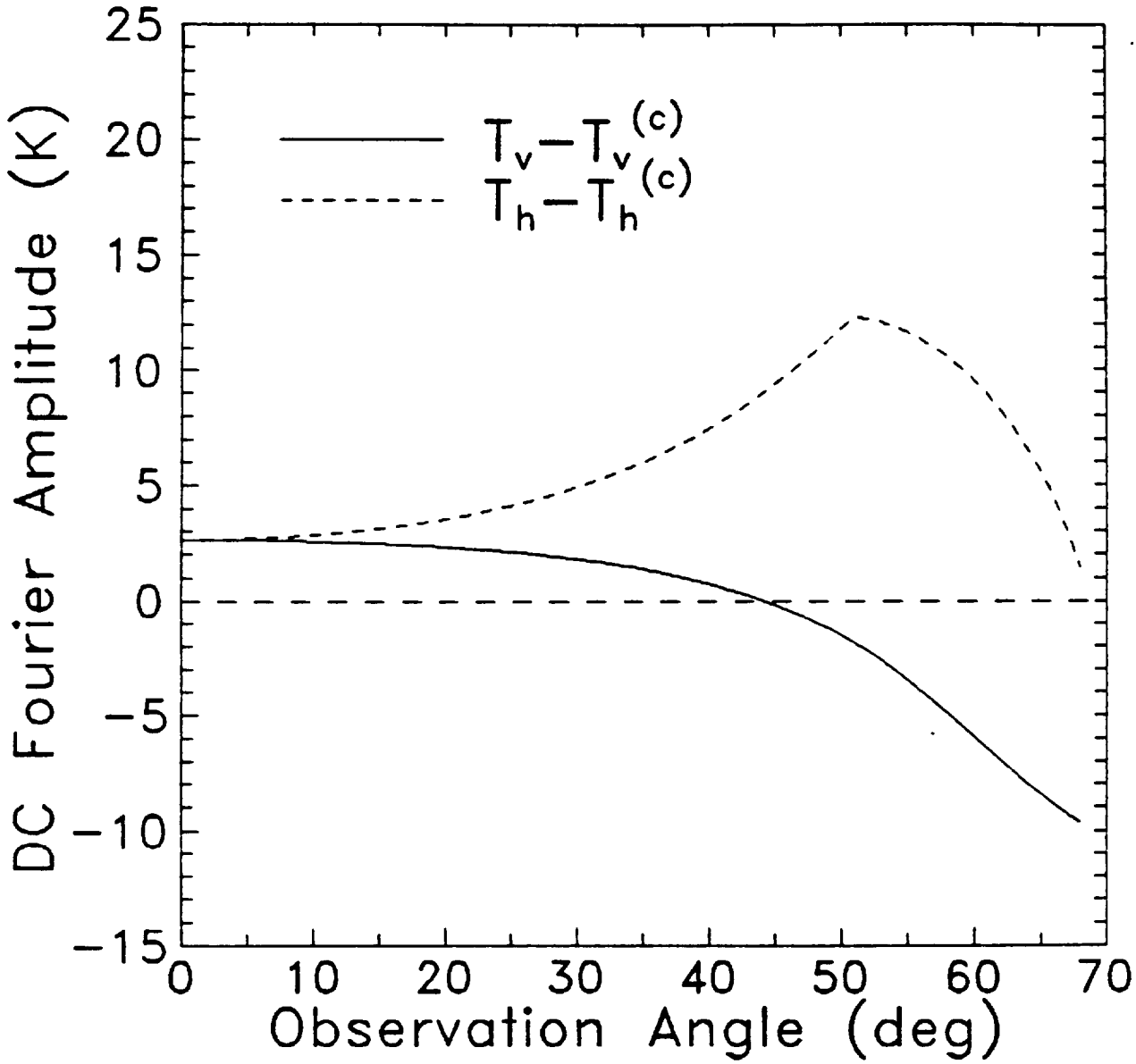
25
20
15
10
5
0
−5
−10
−15
DC Fourier Amplitude (K)
$T_v - T_v^{(c)}$
$T_h - T_h^{(c)}$
0
10
20
30
40
50
60
70
Observation Angle (deg)

Figure 7a

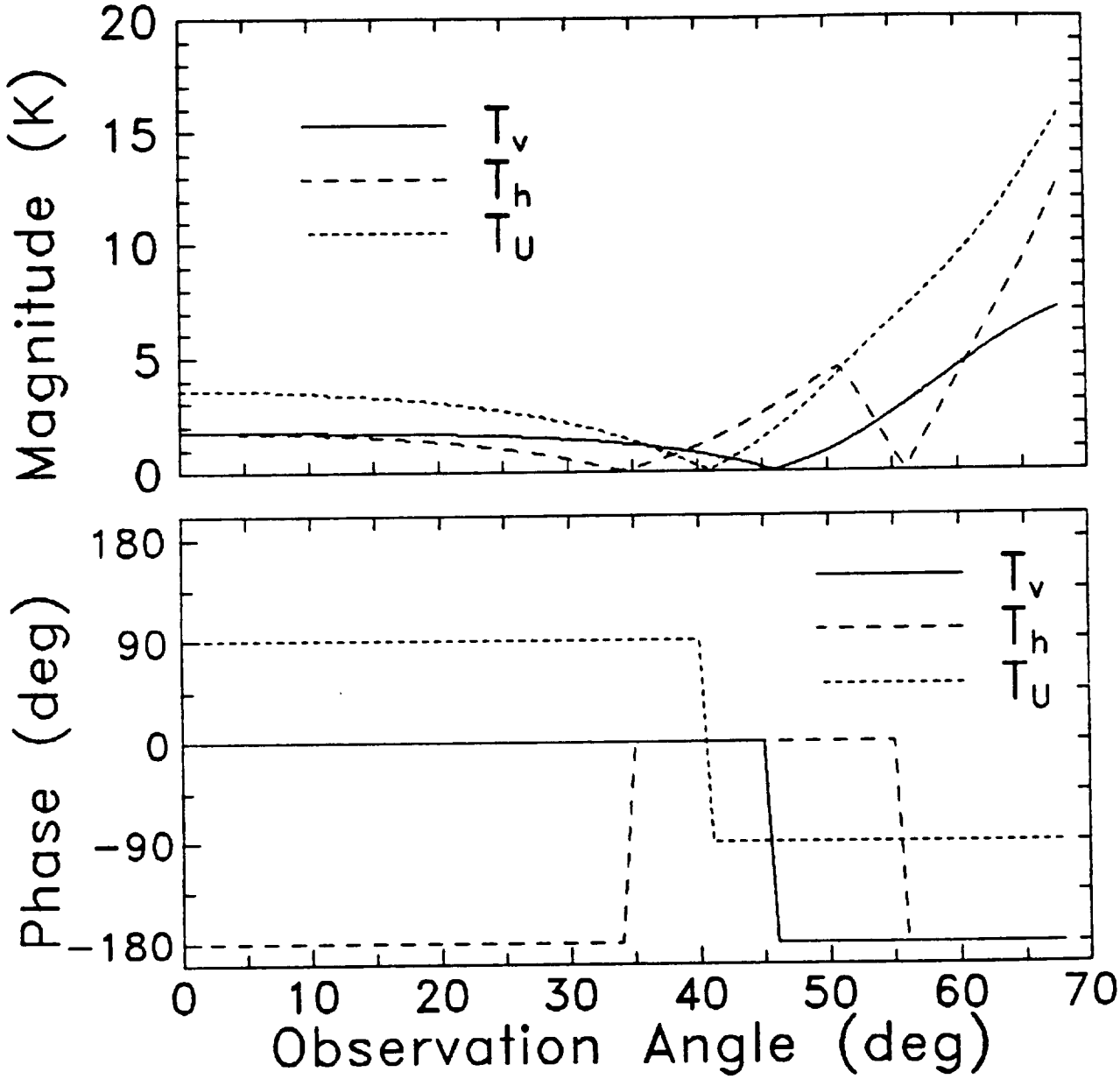
Magnitude (K)
20
15
10
5
0
T_v
T_h
T_U
Phase (deg)
180
90
0
−90
−180
T_v
T_h
T_U
0
10
20
30
40
50
60
70
Observation Angle (deg)

Figure 7b,c

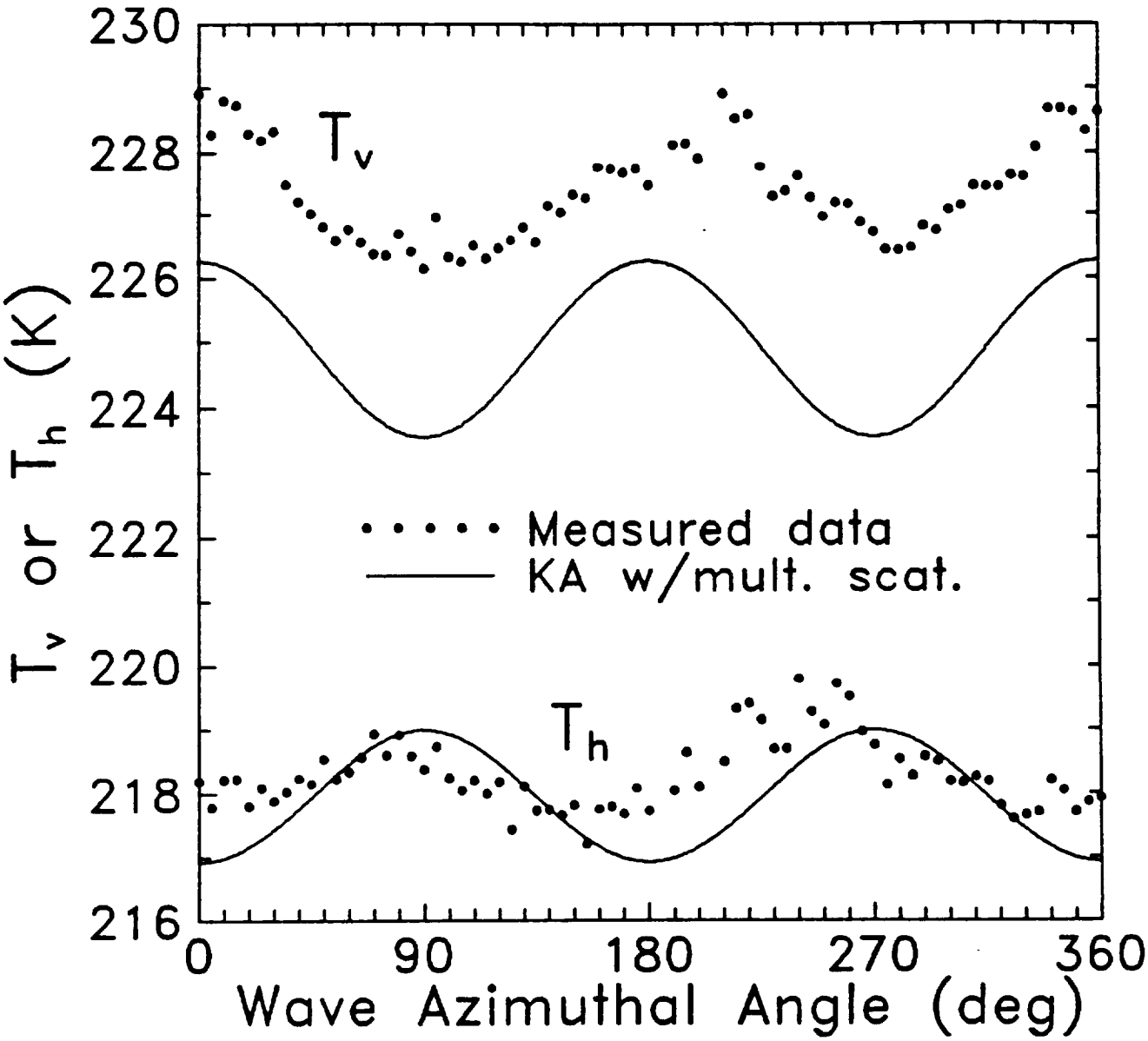
230
228
226
224
222
220
218
216
T_v
T_h
T_v or T_h (K)
Measured data
KA w/mult. scat.
0
90
180
270
360
Wave Azimuthal Angle (deg)

Figure 8a

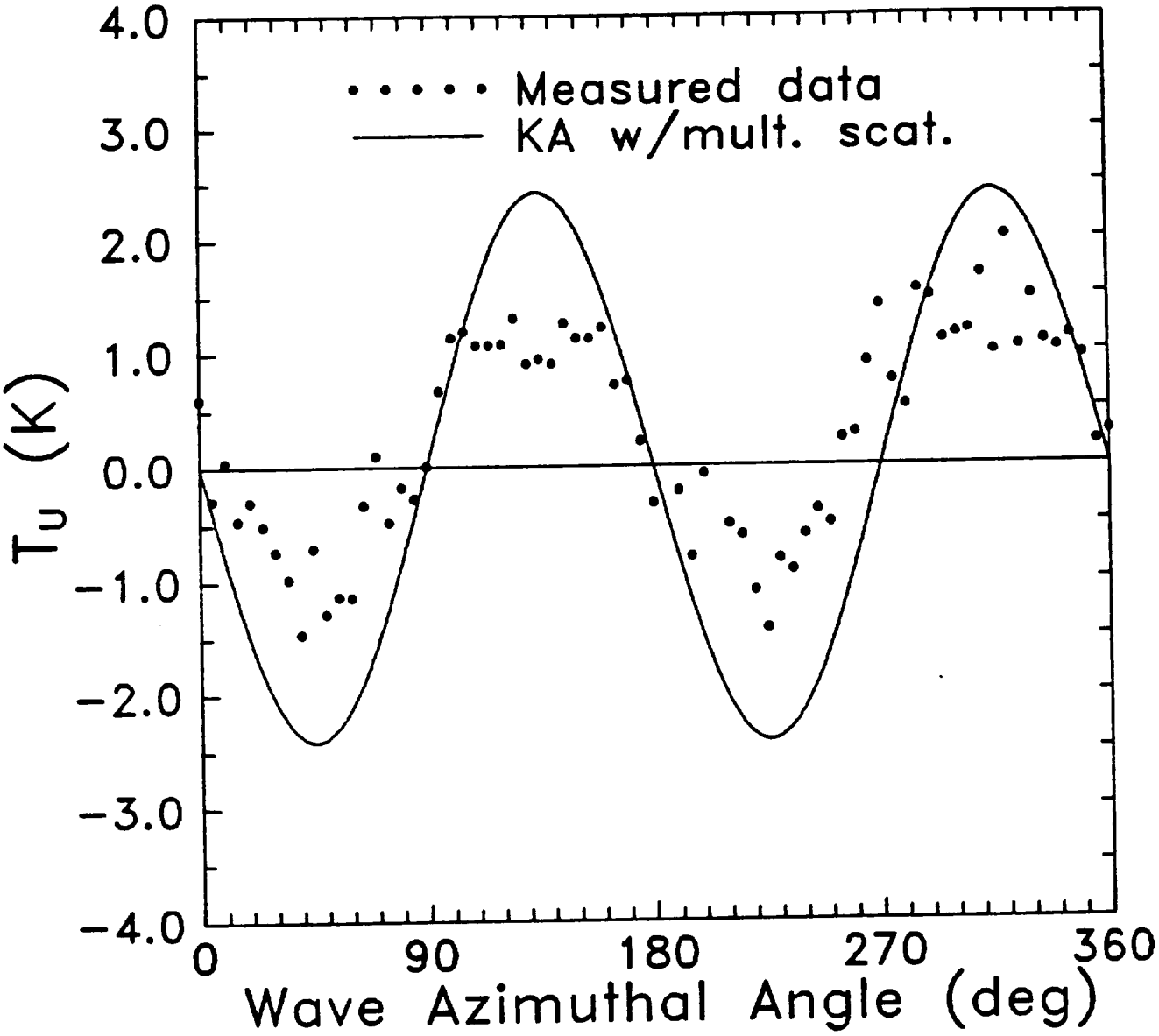
4.0
3.0
2.0
1.0
0.0
−1.0
−2.0
−3.0
−4.0
T_U (K)
Measured data
KA w/mult. scat.
0
90
180
270
360
Wave Azimuthal Angle (deg)

Figure 8b

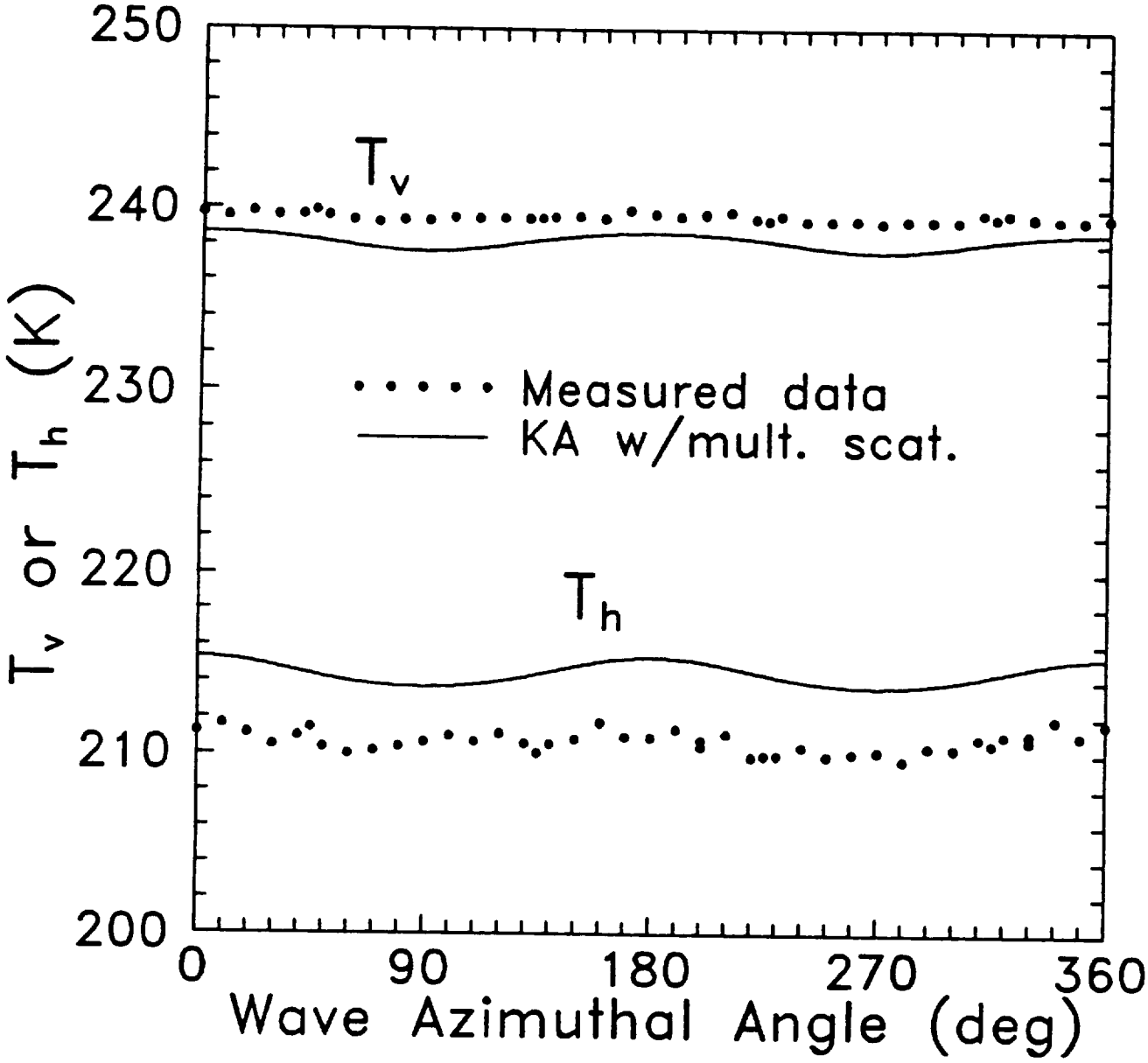
250
240
230
220
210
200
T_v
T_h
Measured data
KA w/mult. scat.
T_v or T_h (K)
0
90
180
270
360
Wave Azimuthal Angle (deg)

Figure 9a

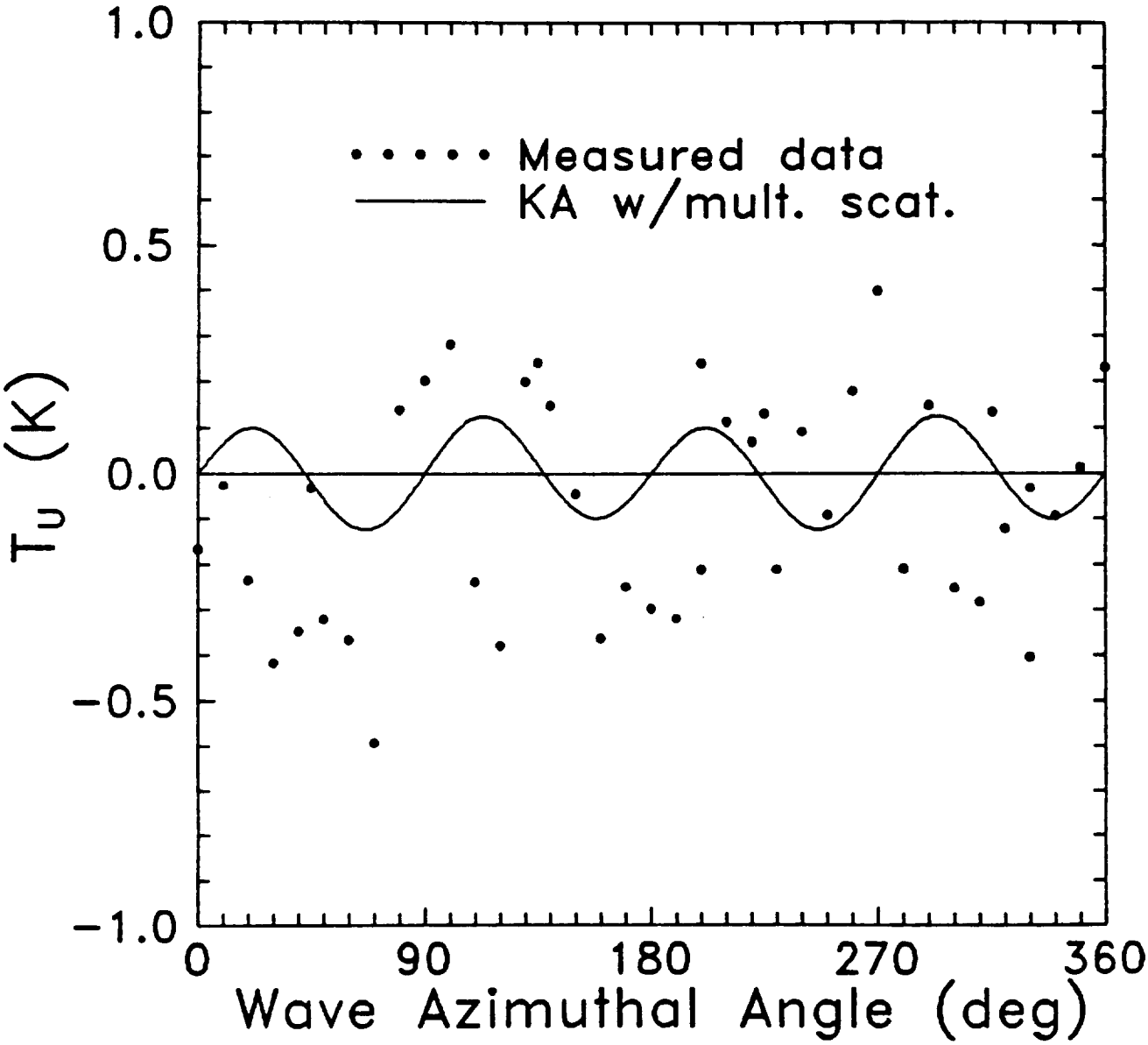
1.0
0.5
0.0
−0.5
−1.0
T_U (K)
Measured data
KA w/mult. scat.
0
90
180
270
360
Wave Azimuthal Angle (deg)

Figure 9b

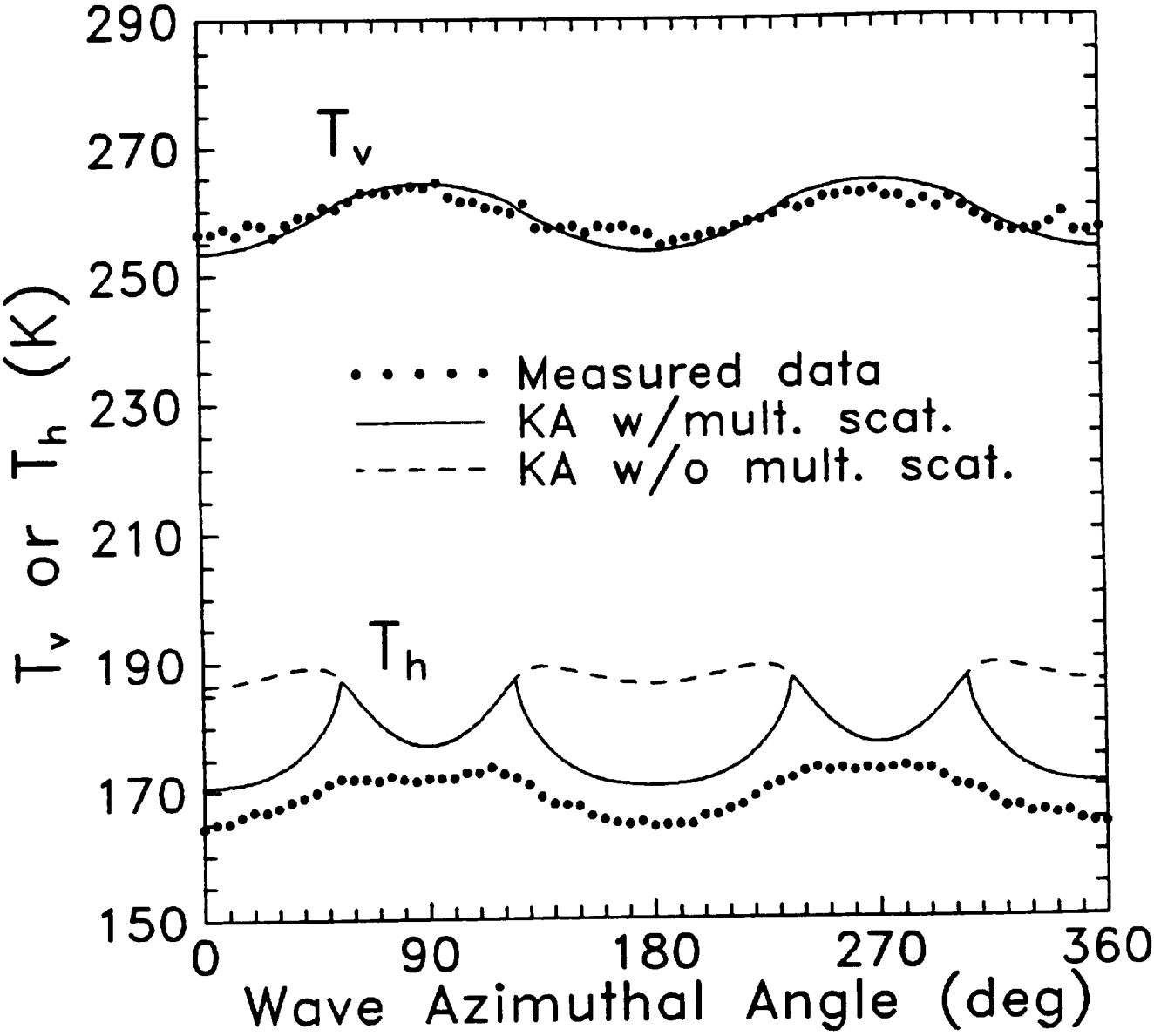
290
270
250
230
210
190
170
150
T_v
T_h
T_v or T_h (K)
Measured data
KA w/mult. scat.
KA w/o mult. scat.
0
90
180
270
360
Wave Azimuthal Angle (deg)

Figure 10a

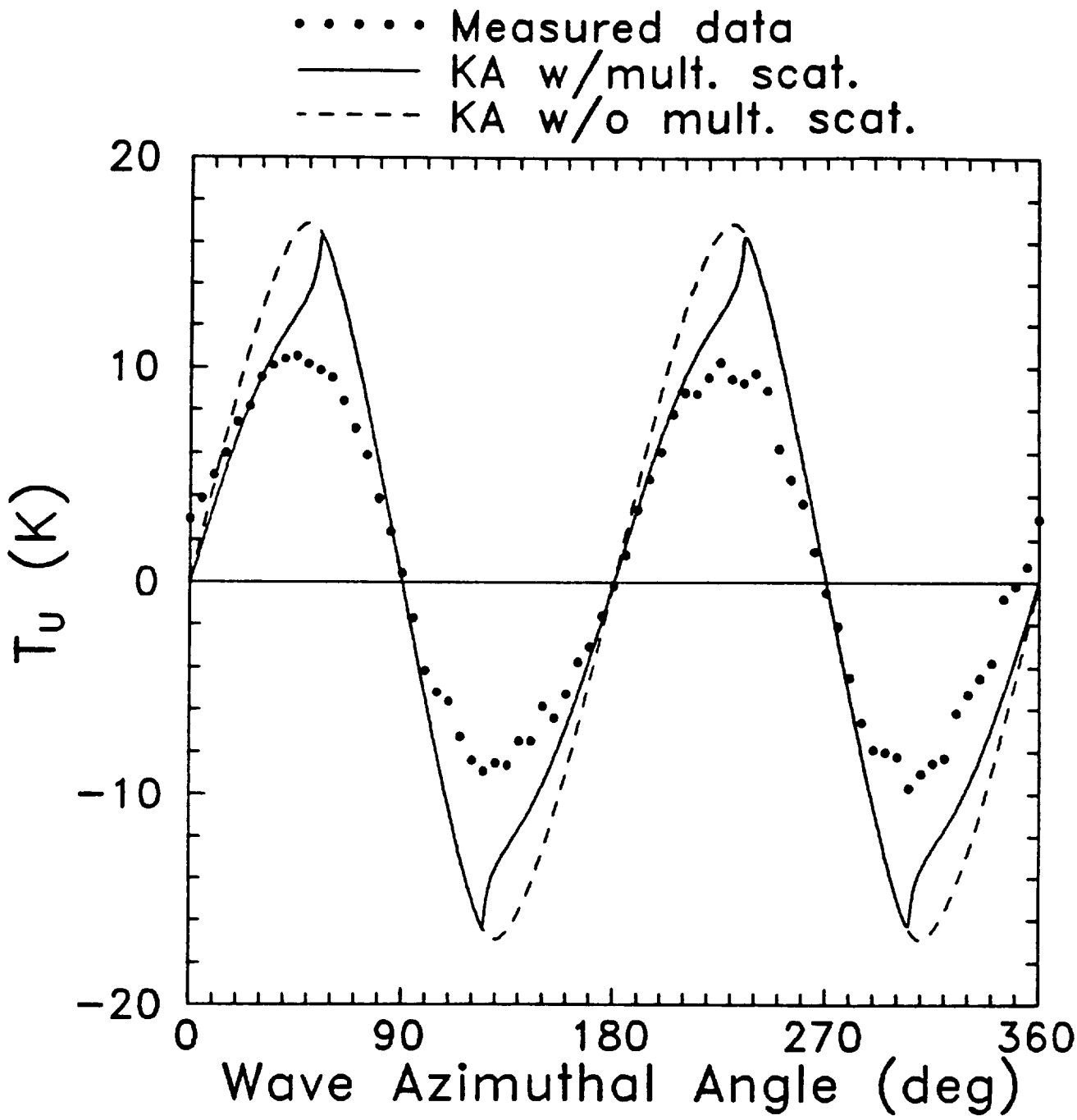
Measured data
KA w/mult. scat.
KA w/o mult. scat.
20
10
0
−10
−20
T_U (K)
0
90
180
270
360
Wave Azimuthal Angle (deg)

Figure 10b